AN INVESTIGATION
INTO
THE HEAT CAPACITIES
OF
THE SUPERCONDUCTING SPINELS

by

PONGSRI SIRIPAIROJE, B.Sc., M.Sc.

A thesis submitted for the degree

of

DOCTOR OF PHILOSOPHY

of

The University of Aston in Birmingham

April, 1978.

AN INVESTIGATION INTO THE HEAT CAPACITIES OF THE SUPERCONDUCTING SPINELS

by

PONGSRI SIRIPAIROJE, B.Sc., M.Sc.

A thesis submitted for the degree of DOCTOR OF PHILOSOPHY of
the University of Aston in Birmingham.

April, 1978.

SUMMARY

A calorimeter, using a silicon wafer as sample holder, temperature sensor and sample heater, and an adiabatic calorimeter with a radiation shield have been designed and constructed for measuring the heat capacities of two superconducting spinel compounds, $LiTi_2O_4$ and $CuRh_2Se_4$, over the temperature ranges 1 - 30°K and 30 - 300°K, respectively.

These data have been analysed at low temperatures to determine coefficients which describe the electronic and lattice contributions for both compounds and at high temperatures to provide an estimate of their anharmonicity. In both cases, the thermal behaviour is very satisfactorily described by the theories which have been developed for strong-coupled superconductors.

Some reasons for the superior superconducting qualities of $LiTi_2O_4$ compared with $CuRh_2Se_4$ are given. In particular, it is found that the major contribution to the improvement in the electron-phonon coupling comes from changes in the McMillan-Hopfield η parameter in agreement with the recent suggestions of Allen and Dynes.

Finally, evidence is presented which indicates that anharmonicity may be an important factor for superconductivity among the materials which crystallize with spinel structure. The heat capacity results thus confirm the conclusions which had been drawn previously from X-ray and Mössbauer investigations on the spinel series $CuRh_{2-x}Sn_xSe_4$.

Index terms:

Anharmonicity

Cryostats

Heat capacity

Spinels

Superconductivity

To

My Father and Mother

I declare that no part of the work described in this thesis was done in collaboration and that the work has not been submitted for any other award.

P. Siripairoje

(Miss) P. Siripairoje

CONTENTS

Page No.

SUMMARY (i)

LIST OF IMPORTANT SYMBOLS (vi)

LIST OF TABLES (ix)

CHAPTER 1 INTRODUCTION 1

1.1 The Phenomenon of Superconductivity 1

1.2 Microscopic Theory 5

1.3 High Transition Temperature Superconductivity 17

1.3.1 Background History 17

1.3.2 Empirical Developments 19

1.3.3 Theoretical Advances 21

1.4 Lattice Instabilities in High T_c Superconductors 24

1.5 Superconductivity amongst Compounds with the Spinel Structure 27

1.5.1 Spinel Compounds 27

1.5.2 The Spinel Structure 28

1.5.3 Structural Distortions 33

1.5.4 The Superconducting Spinels 37

1.6 Scope of the Present Work 49

CHAPTER 2 THE MEASUREMENT OF ANHARMONICITY 51

2.1 The Harmonic Approximation 51

2.2 Anharmonicity 55

2.2.1 Local Atomic Potential Wells 55

2.2.2 High Temperature Anharmonicity 56

2.2.3 Low Temperature Anharmonicity 58

2.3 Anharmonic Contributions to Heat Capacity 60

CHAPTER 3 SAMPLE PREPARATION AND HEAT CAPACITY APPARATUS 67

3.1 Preparation of Samples 67

3.1.1 Preparation of $CuRh_2Se_4$ 68

3.1.2 Preparation of $LiTi_2O_4$ 70

Page No.

3.2 X-Ray Diffraction Analysis 74

3.2.1 Data Handling 77

3.2.2 Some Crystallographic Results 77

3.3 Apparatus for Heat Capacity Measurements over the Temperature Range 1.5 - 300°K 82

3.3.1 Heat Capacity Apparatus for 1.5 - 30°K. 82

3.3.1(a) The Thermometer 85

3.3.1(a) (i) Cleaning Procedure 86

3.3.1(a) (ii) Marking Procedure 86

3.3.1(a)(iii) Diffusion Technique 87

3.3.1(a) (iv) Etching Process 90

3.3.1(a) (v) The Electrical Contacts to Silicon 94

3.3.1(a) (vi) Calibration of Silicon Resistance Thermometers 96

3.3.1(b) Heater 97

3.3.1(c) Cryostat Construction 97

3.3.2 Heat Capacity Apparatus for 30 - 300°K 104

3.3.2(a) Calorimeter 107

3.3.2(b) Adiabatic Radiation Shield 108

3.3.2(c) Thermometry 109

3.4 The Electrical Circuits for Heat Capacity Measurements 111

CHAPTER 4 EXPERIMENTAL PROCEDURE AND RESULTS 116

4.1 Electrical Resistivity Measurements 116

4.1.1 Introduction 116

4.1.2 Measurement Technique 116

4.1.3 Results for $LiTi_2O_4$ 117

4.1.4 Results for $CuRh_2Se_4$ 124

4.2 Heat Capacity Measurements over the Temperature Range 1.5 - 30°K 124

4.2.1 The Thermal Relaxation Method 124

4.2.2 Experimental Procedure 128

Page No.

4.2.3 Determination of Heat Capacity 131

4.2.3(a) Thermal Conductance 131

4.2.3(b) The Relaxation Time Constant 132

4.2.4 Test of the Method of Measurement 132

4.2.5 Results from Heat Capacity Measurements at low temperatures (1.5 - 30°K) 133

4.2.5(a) Heat Capacity for the Empty Calorimeter 133

4.2.5(b) Results for $LiTi_2O_4$ over the Range 4 - 30°K 137

4.2.5(c) Results for $CuRh_2Se_4$ over the Range 1.5 - 30°K 141

4.3 Measurements of Heat Capacity over the Temperature Range 30 - 300°K 145

4.3.1 Experimental Procedure 145

4.3.2 Method of Calculation 146

4.3.3 Estimated Accuracy of Results 147

4.3.4 Results from Heat Capacity Measurements at High Temperatures (30 - 300°K) 148

4.3.4(a) Heat Capacity for the Empty Calorimeter 148

4.3.4(b) Results for $LiTi_2O_4$ over the Range 30 - 300°K 151

4.3.4(c) Results for $CuRh_2Se_4$ over the Range 30 - 300°K 154

4.4 Summary of Smoothed Heat Capacity Results 157

4.4.1 Smoothed Molar Heat Capacity Data for $LiTi_2O_4$ 157

4.4.2 Smoothed Molar Heat Capacity Data for $CuRh_2Se_4$ 159

CHAPTER 5 ANALYSIS AND DISCUSSION 163

5.1 Superconducting Transition Temperatures 163

5.2 Analysis of Low Temperature Heat Capacity Data 166

5.2.1 Heat Capacity Coefficients 166

5.2.2 Thermodynamic Critical Fields 168

Page No.

5.3 Analysis of High Temperature Heat Capacity Data 174

5.3.1 The High Temperature Parameters 174

5.3.2 The Electronic Heat Capacity Coefficient at High Temperatures 175

5.3.3 Estimation of the McMillan-Hopfield η Parameter 179

5.4 Discussion 183

CHAPTER 6 CONCLUSIONS AND SUGGESTIONS FOR FUTURE WORK 188

6.1 Conclusions 188

6.2 Suggestions for Future Work 189

APPENDIX The Nearly Free Electron Approximation 191

ACKNOWLEDGEMENTS 194

REFERENCES 195

LIST OF IMPORTANT SYMBOLS

The following list includes definitions of most of the important symbols used throughout this thesis.

a_o	lattice parameter
A	cross sectional area
B_c	critical magnetic field ($=\mu_o H_c$)
C_E	electronic heat capacity
C_L	lattice contribution including the effects of anharmonicity
C_p	heat capacity at constant pressure
C_v	heat capacity at constant volume
D	constant that is dependent on the phonon density of states
e	electronic charge
$F(\omega)$	phonon density of states
h	Planck's constant = 6.6262×10^{-3} Jsec ($\hbar = h/2\pi$)
$H_c(O)$	critical magnetic field strength at O^oK
$H_c(T)$	temperature dependent thermodynamic critical field
$< I^2 >$	square of the electron-phonon matrix element average over the Fermi level.
J_c	critical current density
k	thermal conductivity linking the sample to the heat reservoir
k_B	Boltzmann's constant = 1.38×10^{-23} Jdeg^{-1}
m*	effective mass of electrons in crystals
$N(\varepsilon_F)$	density of single electron states of one spin in the normal state at Fermi level
$N(\varepsilon)$	density of phonon modes
P	power put into the sample

r	nearest neighbour separation of atoms in a solid
R	gas constant = 8.314 Jmole^{-1}deg^{-1}
'S'	Mössbauer 'S' parameter
S_L	constant volume lattice entropy
$S_s(T_c)$	superconducting state entropy at T_c
$S_n(T_c)$	normal state entropy at T_c
T_c	superconducting transition or critical temperature
T_1	^{51}V nuclear spin-lattice relaxation times
V	molar volume
V_o	velocity of sound
$V(r)$	potential energy
$W(O)$	superconducting ground state energy at $0^{o}K$
α	coefficient of linear expansion
$\alpha^2(\omega)$	average electron-phonon interaction
β	low temperature heat capacity coefficient (or isothermal compressibility)
γ	high temperature electronic heat capacity coefficient
γ_o	low temperature electronic heat capacity coefficient
γ_b	band structure electronic heat capacity coefficient
2Δ	energy gap of superconductor
ε	energy of an electron
ε_F	Fermi energy
ε_o	permittivity of free space = $10^7/4\pi c^2$ (c = velocity of light)
η	McMillan-Hopfield parameter $\{\eta = N(\varepsilon_F) < I^2 > \}$
θ, θ_D	Debye temperature
θ_E	Einstein characteristic temperature
ω	phonon frequency
$< \omega^2 >$	mean square phonon frequency

ω_o	maximum phonon frequency
ω_c	an average phonon cut-off frequency
ω_D	Debye limiting frequency
ω_E	Einstein limiting frequency
ω_s	phonon frequency of the normal mode s
λ	electron-phonon coupling constant
μ	chemical potential
μ^*	Coulomb pseudopotential interaction parameter
τ_1	thermal relaxation time constant
χ_p	Pauli susceptibility

LIST OF TABLES

Table		Page No.
1.1	Experimental values for the exponent of the isotope effect.	10
1.2	Some values of $2\Delta/k_BT_c$ obtained from C_E - T curves.	13
1.3	Some values of C_E at T_c.	15
1.4	Some high T_c superconductors.	20
1.5	A selection of mineral spinels.	29
1.6	Space group Fd3m : No 227.	32
1.7	Crystallographic and superconducting properties of selenide and sulphide spinels.	39
1.8	Electronic parameters characterizing the conduction electrons in $LiTi_2O_4$, derived from magnetic susceptibility measurements.	46
1.9	Heat capacity data and derived quantities for several $Li_{1+x}Ti_{2-x}O_4$ spinel compounds.	47
2.1	The low temperature electronic heat capacity coefficient, γ_o, the band structure electronic heat capacity coefficient, $\gamma_b = \gamma_o(1 + \lambda)^{-1}$, and the low temperature Debye temperature, θ_o, for vanadium-base compounds.	65
2.2	Various parameters found in high temperature analysis of the heat capacity data. The units of γ and A are $mJ/^oK^2$ g-atom.	65
3.1	Preparation conditionsof spinel $LiTi_2O_4$ from Li_2CO_3 and TiO_2.	73
3.2	X-ray data for $LiTi_2O_4$ with spinel structure.	80
3.3	X-ray data for $CuRh_2Se_4$ with spinel structure.	81
4.1	Heat capacity of empty calorimeter with 6 mg of a thermally conductive compound.	136
4.2	The experimental values of the observed heat capacity of $LiTi_2O_4$ between 4.2 and 30^oK.	138

Table		Page No.
4.3	The experimental values of the observed heat capacity of $CuRh_2Se_4$ between 1.5 and 30°K.	142
4.4	Heat capacity of empty calorimeter together with 26.2 mg of thermally conductive compound.	150
4.5	The experimental values of the observed heat capacity of $LiTi_2O_4$ between 30 and 300°K.	152
4.6	The experimental values of the observed heat capacity of $CuRh_2Se_4$ between 30 and 300°K.	155
4.7	Smoothed heat capacity data for $LiTi_2O_4$.	158
4.8	Smoothed heat capacity data for $CuRh_2Se_4$.	160
5.1	Comparison of transition temperatures, T_c, obtained from resistivity measurements and specific heat measurements.	164
5.2	Reported transition temperatures, T_c, for spinel compounds.	165
5.3	Various normal state parameters obtained from the low-temperature analysis of the heat capacity results. Comparison between the values obtained from this and earlier work.	167
5.4	Comparison with BCS theory.	169
5.5	Some parameters found in the high-temperature analysis of the heat capacity data.	177
5.6(a)	Electronic parameters for $LiTi_2O_4$ and $CuRh_2Se_4$.	180
5.6(b)	Various parameters found in the high-temperature analysis of the heat capacity data.	180
5.7	Parameters significant for the strong-coupling superconductivity theory.	182

CHAPTER 1

INTRODUCTION

CHAPTER 1

INTRODUCTION

1.1 The Phenomenon of Superconductivity

Superconductivity was discovered by Kamerlingh Onnes in 1911, three years after the successful liquefaction of helium. He observed, during an investigation of the electrical resistivity of metals, that the resistance of mercury dropped abruptly to a value which he could not distinguish from zero at just below 4.2°K. He also found that below this temperature the resistance remained effectively immeasurable (Figure 1.1). The existence of a new state of mercury, characterized by an absence of electrical resistivity, thus came to be recognized and is now known as the superconducting state. The temperature at which a superconductor loses resistance is called its superconducting transition or critical temperature, T_c, and can be extremely sharp if the specimen is pure and physically perfect. However, the transition may be considerably broadened due to impurities and imperfections of the specimen (see Figure 1.2) and in this case the critical temperature is usually defined as that at the mid-point of the transition. In some cases, however, authors quote the temperature at which the transition begins as T_c - see for example Matthias, Geballe, Geller and Corenzwit (1954).

When a superconductor is cooled through the transition temperature, there is not only an abrupt loss of electrical resistance, as discovered by Onnes, but also abrupt changes in many of the other properties of the material. Among these aspects of physical behaviour, which arise with superconductivity, the magnetic and thermodynamic properties are particularly important.

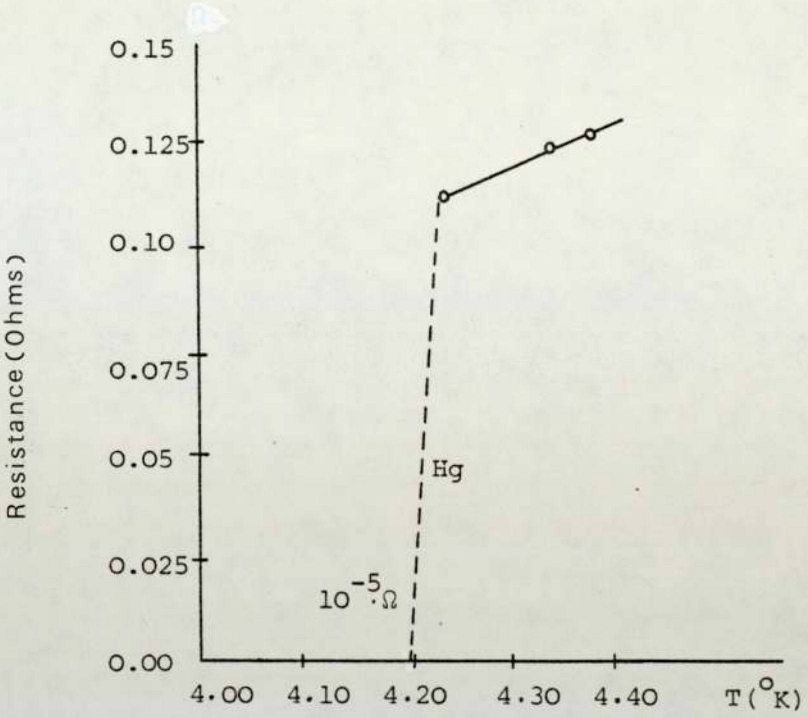

FIGURE 1.1 The electrical resistance of several metals drops discontinuously at a material dependent critical temperature, T_c. The diagram shows Kamerlingh-Onnes' results on mercury (Kamerlingh-Onnes, 1911).

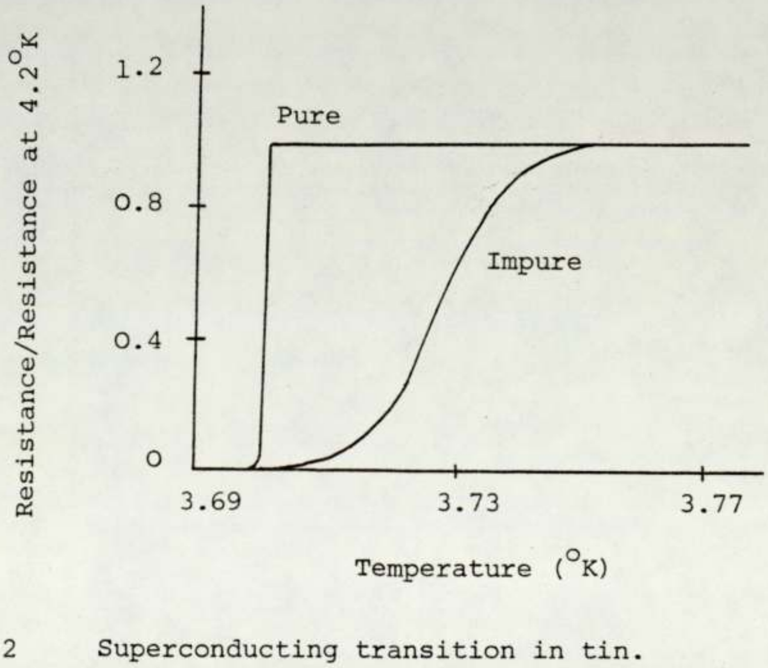

FIGURE 1.2 Superconducting transition in tin.

Much of the modern understanding of superconductors has been derived from measurements of their specific heat. The specific heat of a superconductor consists, like that of a normal metal, of a contribution from the conduction electrons as well as from the crystal lattice. Indeed, measurements of specific heat made immediately after the discovery of superconductivity showed no notable difference between the heat capacities of the superconductive and normal phases. With improvements in thermometry, however, Keesom and Kok (1932) discovered that the specific heat of tin increases sharply and discontinuously as the temperature is lowered through its T_c (see Figure 1.3). In such an experiment, the heat capacity of the normal state of the same sample can be obtained by the application of a magnetic field strong enough to normalize the superconductor. In this way, it has been observed that as the temperature nears absolute zero, the heat capacity in the superconducting state is less than that in the normal state. However, on the assumption that the properties of the lattice (crystal structure, Debye temperature, etc.) are virtually unchanged in the superconducting state, the lattice contribution to the specific heat must be the same in both phases. Hence, it has been concluded that the difference between the specific heat values in the superconducting and normal states can arise only from a change in the electronic specific heat. In many cases, this contribution has been found to vary exponentially with the reciprocal of the temperature, suggestive of excitation of electrons across an energy gap and it is now believed that such a gap is very characteristic, though not a general, feature of the superconducting state.

In 1933, Meissner and Ochsenfeld found that if a superconductor is cooled in a weak magnetic field to below its transition temperature, then at the transition the specimen spontaneously becomes perfectly diamagnetic with the result that all internal magnetic flux is ejected.

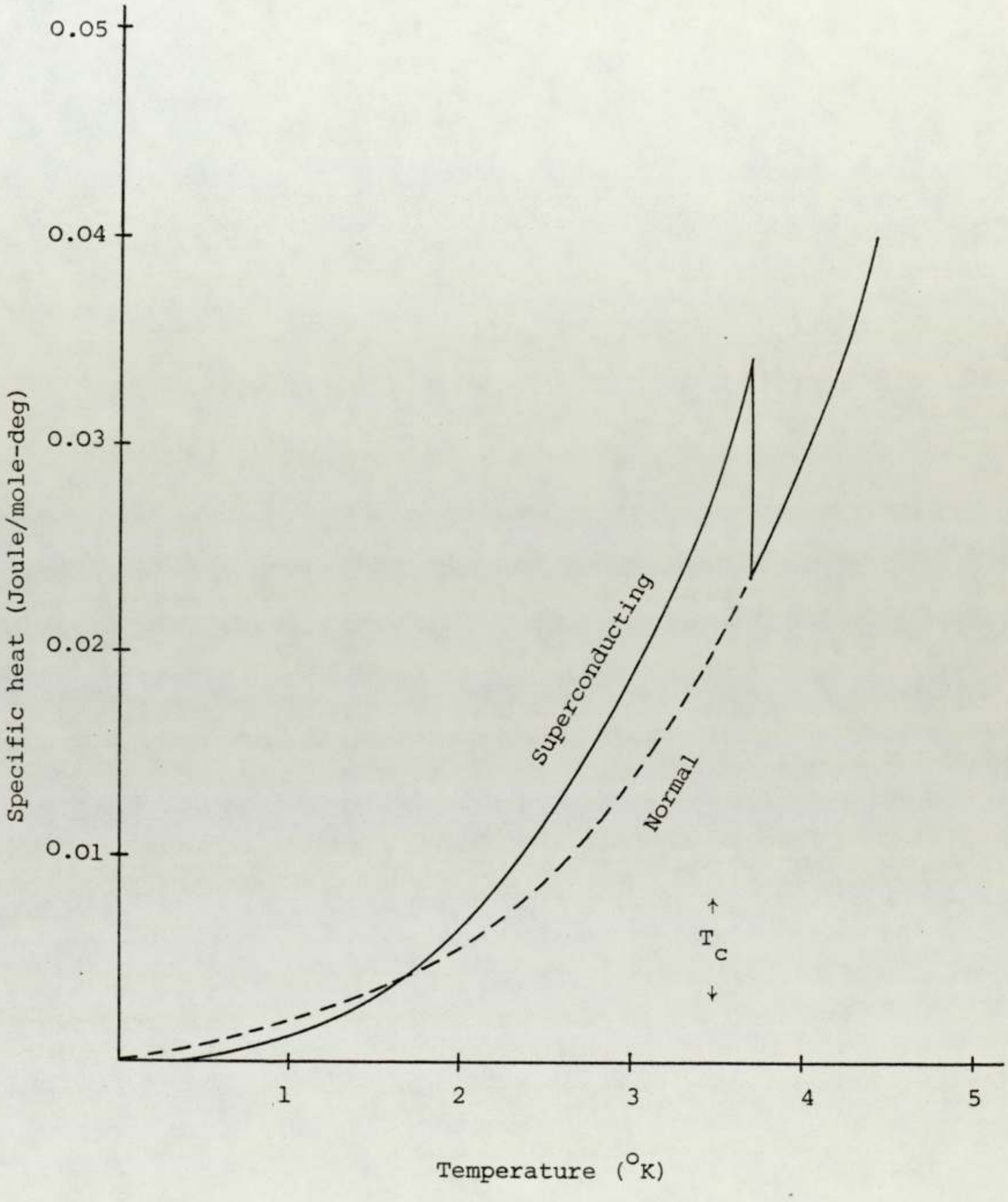

FIGURE 1.3 Specific heat of tin in normal and superconducting states (Keesom and Kok, 1932).

This phenomenon is now called the "Meissner effect". The perfect diamagnetism is destroyed if the magnetic field is excessively powerful or if a sufficiently high current is passed through a superconductor. A superconducting material is therefore often characterized by its critical magnetic field, B_c, and critical current density, J_c, as well as its transition temperature, T_c.

The results from investigations of the heat capacity and magnetic behaviour of superconductors stimulated the development of macroscopic phenomenological theories of superconductivity. For example, F. and H. London (1935 a, b) developed a model for low frequency electromagnetic behaviour which is based on a relation between the current density and the vector potential associated with a magnetic field. Similarly, Gorter and Casimir (1934 a, b) worked on a thermodynamic treatment and presented a two-fluid model, dealing with the ground state of electrons and excited electrons. However, a deeper understanding of superconductors had to await the advent of the microscopic theory of Bardeen, Cooper and Schrieffer (1957) before the unique properties of superconductors could be accounted for in quantum mechanical terms.

1.2 Microscopic Theory

The development of the microscopic theory of superconductivity was assisted by a number of deductions suggested by experimental facts. One of these was based upon the success of the two-fluid model of Gorter and Casimir in accounting for the thermodynamic properties of superconductors. This had made it seem plausible that some of the conduction electrons in a superconductor were condensed into a lower energy phase. Similarly, the fact that the superconductor can only exist below a critical temperature, T_c, indicates that the energy difference between the normal and superconducting phases at absolute zero, which is of the order of k_BT_c per electron where k_B is Boltzmann's constant, is of the order of 10^{-4} eV for a critical temperature of 4°K. This energy difference is much smaller than the Fermi energy of the conduction electrons in a metal, which is in the order of 3-10 eV. In addition, there have been a number of measurements of specific heat of superconductors which indicate the exponential variation of the electronic contribution corresponding to an energy gap, that is, that a certain minimum energy must be required to excite a single electron from the condensed to the normal state.

In an attempt to show that an electron could condense into a low energy state at low temperature, Fröhlich (1950) developed a theory on the assumption that there was an interaction between electrons and the crystal lattice vibrations (phonons). This theory, however, was later shown to be unsatisfactory although one of its predictions, the dependence of critical temperature on isotopic mass, was confirmed experimentally for mercury by Maxwell (1950) and, at the same time, by Reynolds, Serin, Wright and Nesbitt (1950). This demonstrated that the phenomenon of superconductivity indeed arose from an interaction between electrons and phonons.

The first successful microscopic theory of superconductivity was eventually developed by Bardeen, Cooper and Schrieffer in 1957. This was based on the fact, established by Cooper (1956), that if there is an attractive interaction, however weak, between a pair of electrons in the neighbourhood of Fermi Surface, these electrons can condense into a state of lower energy in which each electron is paired with one of equal and opposite momentum and spin. The key idea was that when such an attraction exists between a pair of electrons through the interchange of virtual phonons, this attraction may dominate over the screened Coulomb repulsion. The mechanism can be best described with the aid of a Feynmann Diagram (see Figure 1.4) in which the straight lines represent the electron paths and the wavy line a phonon path. An electron of wave vector $\vec{k}$ emits a virtual phonon $\vec{q}$ which is absorbed by the second electron $\vec{k}'$. The first electron is scattered into $\vec{k} - \vec{q}$ and the second into $\vec{k}' + \vec{q}$. The process occurs rapidly so that, because of the Uncertainty Principle, energy need not be conserved, hence the name virtual process. From the quantum mechanical point of view, if $\varepsilon - \varepsilon' < \hbar\omega$, where ε and ε' are the energies of the first electron before and after the virtual emission of the phonon and $\hbar\omega$ is the phonon energy, the net result of the emission and absorption process is that there is an attraction between the electrons. There is also, of course, the Coulomb repulsion between the electrons; whether the net interaction is attractive or repulsive thus depends on whether the phonon energy exceeds the electronic energy change or vice versa.

On the assumption that all the interactions, except the electron-phonon interaction, are the same for the superconducting and normal state at $0^{O}K$, Bardeen et al. were able to calculate the superconducting ground state energy, W(O), due to the Cooper pair and Coulomb interactions, as:

$$W(O) = \frac{-2N(\varepsilon_F)(\hbar\omega_C)^2}{\exp\{2/N(\varepsilon_F)V\} - 1} \qquad \ldots\ldots (1.1)$$

where $N(\varepsilon_F)$ is the density of single electron states of one spin in the normal state at the Fermi Surface, ω_c is an average phonon cut-off frequency related to the Debye temperature, θ, and V is a parameter describing the Cooper pair and Coulomb interactions between two electrons. To ease the mathematical difficulties, V was assumed to be independent of the individual momenta of all electrons in a narrow shell of energy less than $\hbar\omega_c$ around the Fermi Surface and zero elsewhere.

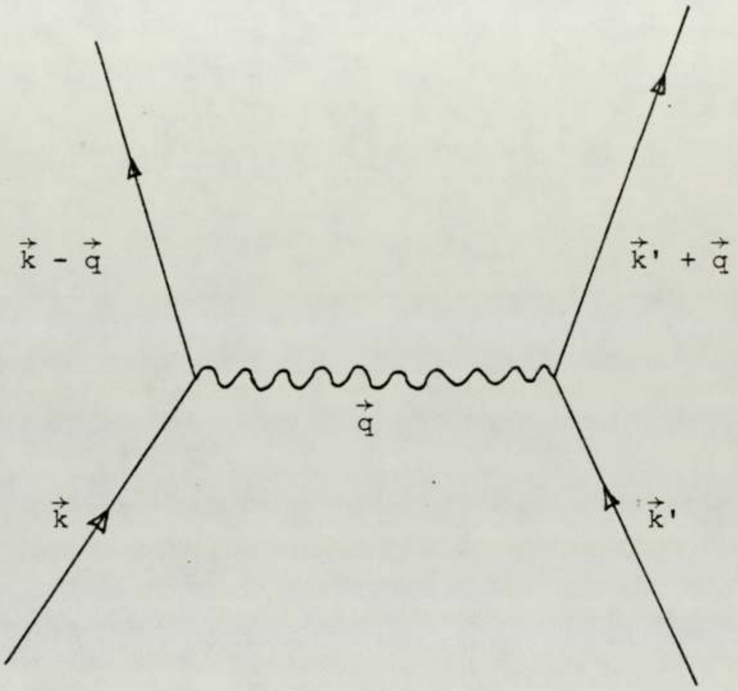

FIGURE 1.4 Feynmann Diagram of Electron-Phonon Coupling. Two electrons, with wave vector $\vec{k}$ and $\vec{k}'$, are scattered into $\vec{k} - \vec{q}$ and $\vec{k}' + \vec{q}$ respectively, by exchange of a virtual phonon $\vec{q}$.

The isotope effect now follows, for the numerator of equation (1.1) involves the electron-phonon interaction with a cut-off frequency related to the Debye temperature, θ, and hence to the isotopic mass, viz:

$$W(0) \propto (\hbar\omega_c)^2 \simeq (k_B\theta)^2 \propto M^{-1} \qquad \ldots\ldots (1.2)$$

However, Maxwell (1950) and Reynolds et al. (1950) showed that the critical temperature of mercury isotopes depends on the isotopic mass, M, according to the relation:

$$T_c M^a = \text{constant} \qquad \ldots\ldots (1.3)$$

According to the BCS theory, the exponent, a, involved in the isotope effect should equal 0.5. Table 1.1 contains the experimental and theoretical values of this exponent. It is noted that in all the non-transition metals, with the exception of molybdenum, the results are consistent with the BCS theory (i.e., $a = 0.5$) but the transition metals show marked differences and do not conform.

The energy difference between the normal and superconducting phases was also calculated and this showed that there was an energy gap for the excitation of electrons from the superconducting state. The theory predicts that the width of this gap decreases to zero as the temperature rises from 0^oK to T_c. At 0^oK, the energy gap has the value 2Δ given by the relation:

$$2\Delta = 4(\hbar\omega_c) \exp\left\{\frac{-1}{N(\varepsilon_F)V}\right\} \qquad \ldots\ldots (1.4)$$

Among the predictions of the BCS theory, the expression for the superconducting transition temperature is derived in the form:

$$k_B T_c = 1.14\,(\hbar\omega_c)\exp\left\{\frac{-1}{N(\varepsilon_F)V}\right\} \qquad \ldots\ldots (1.5)$$

TABLE 1.1

Experimental values for the exponent of the isotope effect.

SUPERCONDUCTOR	a EXPERIMENTAL	a THEORETICAL
Hg	0.50	0.46
Mo	0.37	0.3
Os	0.23	0.25
Pb	0.48	0.47
Re	0.39	0.41
Ru	0.00	0.35
Sn	0.47	0.42
Tl	0.5	0.43
Zr	0.00	0.30

Note: The BCS theory predicts a = 0.5 for all superconductors. The theoretical values of a given above are from the work of Morel and Anderson (See, Claeson and Lundquist, 1974).

Thus, combining equation (1.4) and (1.5) allows for the width of the energy gap and T_c to be linked directly:

$$2\Delta = 3.52\ k_B T_c \text{ at } 0^{\circ}K \qquad \ldots\ldots (1.6)$$

Figure 1.5 shows the remarkable quantitative agreement obtained between theory and experiment for indium, tin and lead.

Experimental evidence for the energy gap can be obtained from specific heat measurements which show, for example, that in the superconducting state there is an exponential variation of the electronic specific heat, C_E, given by:

$$C_E \propto \exp\left[-\frac{2\Delta}{k_B T}\right] \qquad \ldots\ldots (1.7)$$

On the other hand, the BCS theory yields:

$$\frac{C_E}{\gamma_o T_c} \simeq 8.5 \exp\left[-1.44\ T_c/T\right], \quad 2.5 < T_c/T < 6 \qquad \ldots\ldots (1.8)$$

$$\simeq 26 \exp\left[-1.62\ T_c/T\right], \quad 7 < T_c/T < 12 \qquad \ldots\ldots (1.9)$$

where γ_o is the low temperature electronic heat capacity coefficient. In practice, the form of the specific heat curves closely resemble equation (1.8) and some values of $2\Delta/k_B T_c$ determined by fitting this equation are given in Table 1.2. For widely different metals, the values do cluster around the idealised 3.52 of the BCS theory, which, incidentally, assumes the metal to be isotropic.

Further numerical predictions of the BCS theory include:

$$\frac{C_E(T_c)}{\gamma_o T_c} = 2.43 \ldots\ldots \qquad \ldots\ldots (1.10)$$

and

$$\frac{\gamma_o T_c^2}{H_c^2(0)} = 0.170 \qquad \ldots\ldots (1.11)$$

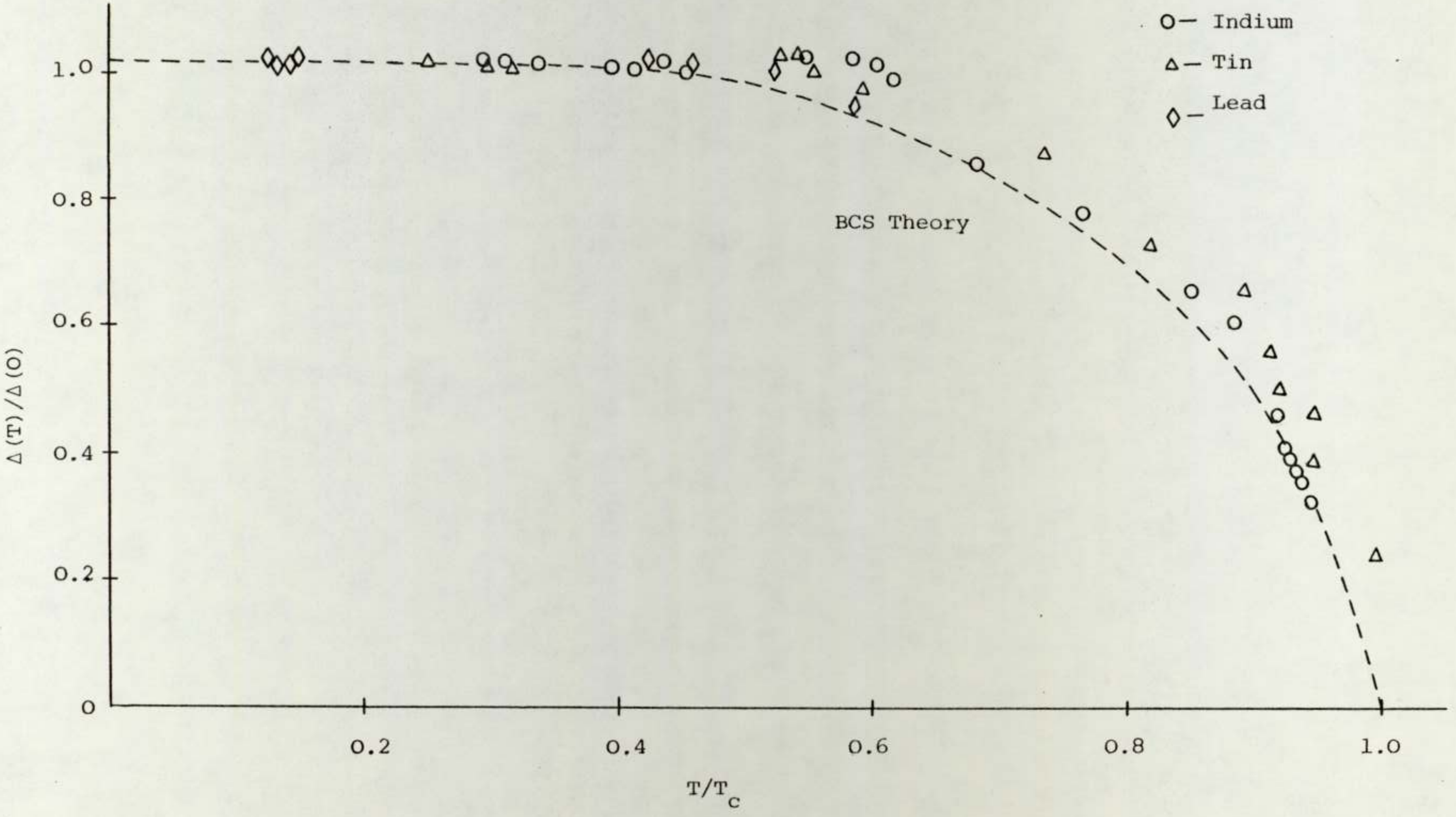

FIGURE 1.5 The gap parameter, Δ(T), decreases with increasing temperature and becomes zero at $T = T_c$. The dashed line is the solution of the gap equation, while the points are experimental points determined by the tunneling technique (Giaever and Megerle, 1961).

TABLE 1.2

Some values of $2\Delta/k_B T_c$ obtained from C_E - T curves

(Goodman, 1959).

Element	Energy gap ($2\Delta/k_B T_c$)
Aluminium	2.9
Indium	3.9
Niobium	4.4
Tantalum	3.6
Thallium	3.2
Tin	3.6
Vanadium	3.6
Zinc	2.5

where $H_c(0)$ is the critical magnetic field strength at $0^{\circ}K$. However, as Table 1.3, taken from Bardeen and Schrieffer (1961) shows, only a few metals satisfy equation (1.10) reasonably well.

Similarly, Pokrovskii (1961) and Pokrovskii and Ryvkin (1962) have investigated the effects of anisotropy on thermal and magnetic properties. They found that in anisotropic superconductors the specific heat ratio $\frac{C_E\ (T_c)}{\gamma_o T_c}$ is smaller than 2.43 and the value of $\frac{\gamma_o\ T_c^{\ 2}}{H_c^{\ 2}(0)}$ is larger than 0.170. Furthermore, measurement of the critical magnetic field variation with temperature by Swihart, Scalapino and Wada (1965) shows large differences between the theory and experiment for lead and mercury (see Figure 1.6).

All these discrepancies indicate the need to refine the details of the BCS theory. In particular, it is believed that the assumption that the interaction parameter V is constant, isotropic and instantaneous is unnecessarily restrictive. Usually, one is interested in excitation energies which are of the order of k_BT_c and the BCS assumption, based on the isotropic model, really only works satisfactorily when k_BT_c is very much less than $\hbar\omega_c$, this condition being referred to as the "Weak-Coupling Limit". This may be expressed as $T_c << \theta$ since $\hbar\omega_c \simeq k_B\theta$. However, this condition does not hold for a number of elements, in particular for Pb and Hg. These are therefore called "strong-coupling" superconductors in which the electron-phonon interaction is so strong that the attraction mediated by the heavy ions is retarded, that is to say that there is a delay between the emission and absorption of the virtual phonon.

By using a more realistic energy dependence for the interaction parameter V than that assumed in the BCS theory, and with the addition of an expression $(\lambda - \mu^*)$ for $N(\varepsilon_F)V$, λ being the electron-phonon coupling constant and μ^* the Coulomb pseudopotential interaction

TABLE 1.3

Some values of C_E at T_c

(Bardeen and Schrieffer, 1961).

Element	$\frac{C_E\ (T_c)}{\gamma_o T_c}$
Lead	3.65
Mercury	3.18
Niobium	3.07
Tin	2.60
Aluminium	2.60
Tantalum	2.58
Vanadium	2.57
Zinc	2.25
Thallium	2.15

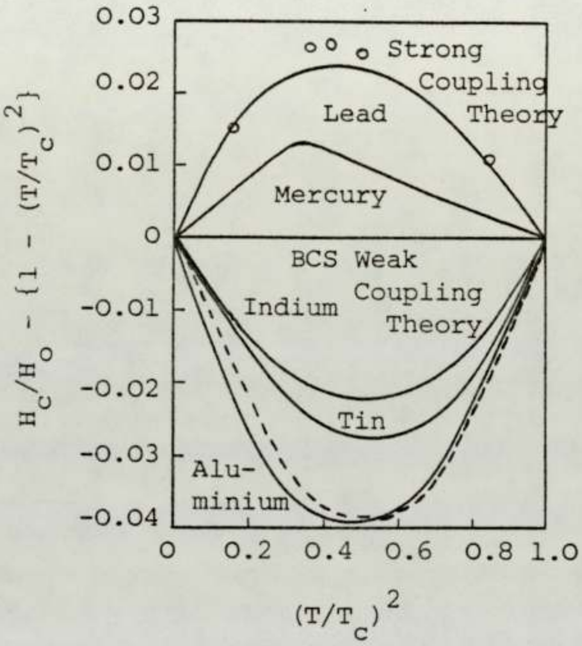

FIGURE 1.6 The normalized critical magnetic field does not quite show a parabolic dependence upon temperature. Full lines are experimentally determined while the dashed line is obtained from the original BCS theory. Note that the curve for a weak coupling superconductor like Al agrees excellently with the BCS weak coupling theory, but the strong coupling superconductors Pb and Hg deviate considerably. The circle denotes values for Pb obtained from a strong coupling modification of the BCS theory by Swihart et al., (1965).

parameter, Morel and Anderson (1962) have been able to develop a "strong-coupling BCS" theory which describes the anomalous superconductors more exactly.

1.3 High Transition Temperature Superconductivity

1.3.1 Background History

The study of high-temperature superconductivity began in 1941 when Aschermann, Friederich, Justi and Kramer discovered superconductivity in the NaCl-structure compound NbN at 15°K. The highest superconducting transition temperature known to date for compounds in the NaCl-structure class was found by Matthias in 1953 to be 18°K for $NbN_{0.7}C_{0.3}$.

Since 1953, there have been no reports of higher T_c for compounds in the NaCl class. However, in that year, Hardy and Hulm reported that the cubic A15 structure compound V_3Si became superconducting at 17°K. Subsequently, Matthias, Geballe, Geller and Corenzwit (1954) have found a T_c of 18°K for Nb_3Sn which also has an A15 structure. With these discoveries, it became apparent that the A15 structure was peculiarly favourable for high-temperature superconductivity. Considerable effort in searching for materials with higher transition temperature over the following twelve years resulted in the discovery of a large number of compounds and alloys which were superconductors, but all the materials studied had transition temperatures below 18°K. However, in 1966, Nb_3Ga was observed by Kunz and Saur (1966) to show traces of superconductivity up to 19.5°K and in the following year $Nb_3Al_{0.75}Ge_{0.25}$ was observed to become superconducting at 20 - 21°K (Matthias, Geballe, Longinotti, Corenzwit, Hull, Willens and Maita, 1967).

Further progress in raising the T_c of A15 compounds has continued right up to the present time. Thus, in 1973, Gavaler made an important advance by obtaining a T_c above 22°K for Nb_3Ge sputtered on to hot substrates at high argon pressure and, using similar techniques, Testardi, Wernick and Royer (1974) subsequently found an even higher onset of T_c at 23.2°K for the same material, which is now the highest reported T_c known.

However, several compounds which have a crystal structure not belonging to either the A15 or the NaCl type have been recently reported to become superconducting at above 10°K. Another, first discovered by Chevrel, Sergent and Prigent (1971) which was also found to become superconducting (Matthias, Marezio, Corenzwit, Cooper and Barz, 1972; Marezio, Dernier, Remeika, Corenzwit and Matthias, 1973), was the rhombohedral-crystal structure of ternary molybdenum sulfides of the composition $M_xMo_3S_4$ ($x \simeq 0.5$, M = Pb, Sn, Cu, Ag . . .). The highest transition temperatures for these ternary sulfides, somewhere around 15°K, were found for M being Sn and Pb phases. Another non-cubic crystal, hexagonal $Li_xTi_{1.1}S_4$ ($0.1 < x \leqslant 0.3$), was reported to become superconducting over the temperature range 10 - 15°K (Barz, Cooper, Corenzwit, Marezio, Matthias and Schmidt, 1972). Recently, the metastable compounds $(Th_{1-x}M_x)_2C_3$ (M = La, Y, Lu . . .) with the body-centred cubic Pu_2C_3 crystal structure, have been synthesized under high-temperature - high pressure conditions and found to become superconductors with transition temperatures up to 17°K (Giorgi, Szklarz and Krupka, 1972).

Finally, superconductivity in oxide compounds has been observed at temperatures below 7°K for $Rb_{\sim 0.1}WO_3$, with hexagonal crystal structure, by Remeika, Geballe, Matthias, Cooper, Hull and Kelly (1967). However, in 1973, the compound $LiTi_2O_4$ with the cubic spinel structure was found to be superconducting at temperatures approaching 14°K (Johnston, Prakash, Zachariasen and Viswanathan). This is not only by far the highest transition temperature superconducting oxide known, but also the lowest density superconducting material discovered to date. Table 1.4 lists a number of some high transition temperature superconductors.

1.3.2 Empirical Developments

At present, it does not seem possible to encompass all superconductors within a unified description or theory. However, empirical rules for the occurrence of superconductivity and a criterion for the transition temperature have been established for elements and may be summarized as follows (Matthias, 1957; Matthias, Geballe and Compton, 1963):

1) Superconductivity is excluded from non-metals and from metals with less than two or more than eight electrons per atom.
2) High T_c's correspond to metallic elements with five or seven valence electrons per atom.
3) There are three crystal structures which are most favourable for superconductivity - namely, face-centred cubic, body-centred cubic and closed-packed hexagonal.
4) Transition elements tend to have the highest T_c's and their isotope effects are anomalous, for example, no isotope effect is observed with Ru and Os.

Matthias et al. (1963) have also studied superconductivity in compounds and found that, with the exception of NaC and NbN which have the cubic NaCl-type structure, most of the high-temperature superconductors have the β -tungsten or A15 structure.

Furthermore, in 1968, by using the correlation between transition temperature and valence-electron density, instead of valence electrons per atom as Matthias had suggested, Pessall, Gold and Johansen

TABLE 1.4

Some high T_c superconductors.

Compounds	T_c (^oK)	Crystal structure types
V_3Sn	8.3	A15
V_3Si	17.1	A15
Nb_3Au	11.5	A15
Nb_3Sn	18.3	A15
Nb_3Al	18.9	A15
Nb_3Ga	20.3	A15
Nb_3Ge	23.2	A15
$TaC_{0.989}$	9.7	NaCl
$NbC_{0.977}$	11.1	NaCl
NbN	17.0	NaCl
$(NbN)_{0.8}(TiC)_{0.2}$	18.0	NaCl
$NbC_{0.3}N_{0.7}$	18.0	NaCl
$Pb_{0.5}Mo_3S_4$	15.2	Rhombohedral
$Rb_{\sim 0.1}WO_3$	7.0	Hexagonal
$LiTi_2O_4$	13.7	Spinel

(1968) found that the T_c-valence electron density correlation is the most successful empirical method of systematizing both A15 and NaCl-structure compounds (see Figure 1.7). Moreover, Pessall et al. (1968), Phillips (1972) and Zeller (1972) all find a significant correlation between T_c and relative volume available to the transition metal atoms in NbN and related compounds (see, for example, Figure 1.8), while Testardi (1972) working on the strain dependence of T_c in the A15 alloys has emphasized the importance of volume per atom.

1.3.3 Theoretical Advances

Using strong-coupling modifications to the original BCS theory of superconductivity, McMillan (1968) has derived a modified relationship between the transition temperature, T_c, and the various microscopic parameters of the form:

$$T_c = \frac{\theta}{1.45} \exp\left[\frac{-1.04\ (1+\lambda)}{\lambda - \mu^*\ (1+0.62\lambda)}\right] \qquad \text{...... (1.13)}$$

where θ is the Debye temperature, μ^* the Coulomb pseudopotential interaction parameter of Morel and Anderson (1962) which is generally accepted to have a value close to 0.13 for transition metals and the electron-phonon coupling constant, λ, is defined through:

$$\lambda = 2 \int_0^{\omega_0} \alpha^2(\omega)\ F^2(\omega)\ \frac{d\omega}{\omega} \qquad \text{...... (1.14)}$$

where ω_0 is the maximum phonon frequency, $F(\omega)$ is the phonon density of states, $\alpha^2(\omega)$ is an average electron-phonon interaction which, if constant, leads to:

$$\lambda = \frac{N(\varepsilon_F)\ \langle I^2 \rangle}{M \langle \omega^2 \rangle} \simeq \frac{\eta}{M \langle \omega^2 \rangle} \qquad \text{...... (1.15)}$$

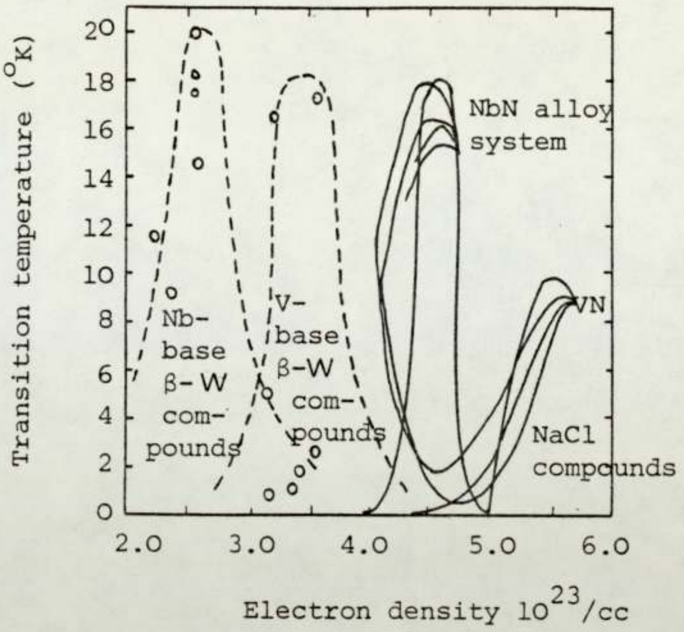

FIGURE 1.7 T_c - electron density relationships for Nb- and V-base β-W compounds and carbonitrides with the NaCl crystal structure. (Pessall et al., 1968).

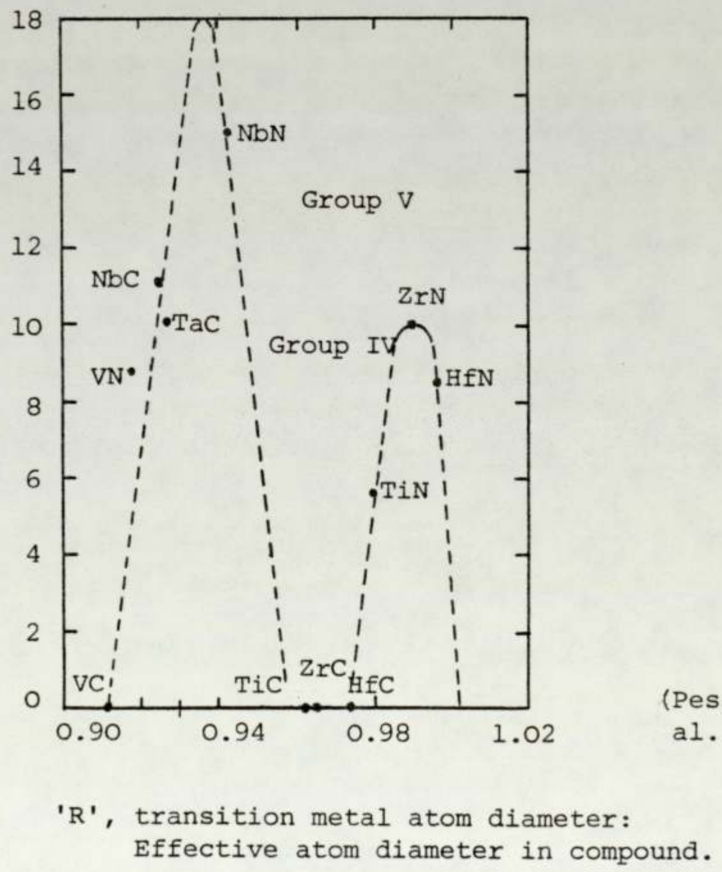

(Pessall et al., 1968).

FIGURE 1.8 Transition temperatures of interstitial compounds as a function of the OD (optimised distance) ratio R.

where $$< \omega^2 > = < \omega > / < \omega^{-1} > \qquad \text{...... (1.16)}$$

$N(\varepsilon_F)$ is the electronic density of states at the Fermi energy, ε_F, M is the atomic mass, $< \omega^2 >$ is the mean square phonon frequency and $< I^2 >$ is the square of the electron-phonon matrix element averaged over the Fermi Surface.

While investigating the dependence of the coupling constant on the various metallic properties, McMillan found that for a given class of materials the electronic factor $N(\varepsilon_F) < I^2 >$ (or η) remains nearly constant. He suggested, therefore, that the electron-phonon coupling parameter, λ , and, hence T_c, is governed primarily by the phonon factor and not by the electronic band structure. This idea was supported by Hopfield (1969) who showed how η can be regarded as a local "chemical" property of an atom in a crystal, while Gaspari and Gyorffy (1972) discovered a simple way of calculating η by muffin-tin approximation when the electron scattering phase shifts of the crystal potential are known.

A remarkable feature of McMillan's theory is that he was able to derive an expression for the maximum transition temperature, T_c max, attainable within a given class of material, viz:

$$T_c / T_c \text{ max} = \left(\frac{2}{\lambda}\right)^{\frac{1}{2}} \exp \left(\tfrac{1}{2} - \frac{1}{\lambda}\right) \qquad \text{...... (1.17)}$$

Now in his assumption of a maximum T_c, for a group of compounds, it is necessary that the average phonon frequency be capable of indefinite reduction. McMillan noted, however, that this is likely to drive a phonon mode unstable, resulting in lattice transformation before T_c max can be attained.

Coincidentally, it was at this time that experimentalists and in particular those associated with Matthias's group, began to realize that the compounds with predicted high T_c according to Matthias's rules would not form. The implication seemed to be that instability was an essential requirement for high T_c superconductivity.

1.4 Lattice Instabilities in High T_c Superconductors

The realization of the importance of lattice instabilities with respect to superconductivity was initially very disconcerting, since these instabilities could lead to phase transformations. It was expected, as indeed appeared to be experimentally true, that A15 compounds with theoretically predicted high transition temperatures would either not form at all or, even if formed would transform to a low T_c or even non-superconducting state.

The importance of stability rules, as derived from the expression for the strain energy of a crystal, was first emphasized by Born (1940) who pointed out that, for cubic crystals, the elastic constants must satisfy the following conditions:

$$\begin{aligned} (C_{11} + 2C_{12}) &> 0 \\ (C_{11} - C_{12}) &> 0 \qquad \qquad \ldots\ldots (1.18) \\ C_{44} &> 0 \end{aligned}$$

These conditions are related to the velocity of sound in the crystal. Any structural defect may lead to an elastic relaxation corresponding to one of these conditions. Ultrasonic measurements of the velocity of sound and, therefore, of the elastic constants have been made on a number of high T_c A15 superconductors (Testardi, Soden, Greiner, Wernick and Chirba, 1967). They found that whilst elastic instability occurred in polycrystalline samples of all of the high T_c A15 superconductors, it did not occur in the isostructure compounds with low T_c. Initially, Testardi suggested that lattice softening affected the T_c via its effect upon the electronic band structure which, in turn, required the involvement of low frequency phonons. However, Shirane and Axe (1971) have shown, from their subsequent neutron diffraction studies, that it is the high frequency transverse acoustic (TA) modes that actually soften (see Ramakrishnan, 1973). In his more recent work, Testardi (1972) has shown that the observed high strain dependence of T_c was not a function of the band structure at all, but depended upon the phonon behaviour. Significantly perhaps, it was also at around this time that theoretical studies based on strong coupling theory indicated that, under certain circumstances, the transition temperature could depend primarily upon the phonon frequencies and, moreover, that some local or chemical property of the crystal structure might also be involved (McMillan, 1968; Hopfield, 1969).

The A15 structure is rather unusual in that the atoms of the transition element component are arranged as three mutually perpendicular systems of chains, while the atoms of the non-transition element are contained within icosahedral 'cages' (see Figure 1.9) which are relatively oversized (Grimes, 1976). This latter condition might well account for the intrinsic hydrostatic instability of the structure and correlates with the low temperature anharmonicity found by Shier and Taylor (1968) in their Mössbauer investigations of Nb_3Sn.

Similar characteristics seem to arise with other crystal structures which are favourable to high transition temperature superconducitivity. For example, the compounds related to NbN with the rock-salt structure have transition temperatures which are sensitive functions of the volume available to the transition metal atoms with, once again, a hydrostatic instability thought to be involved (Phillips, 1972). Phillips also concluded that there is a lattice instability present in the

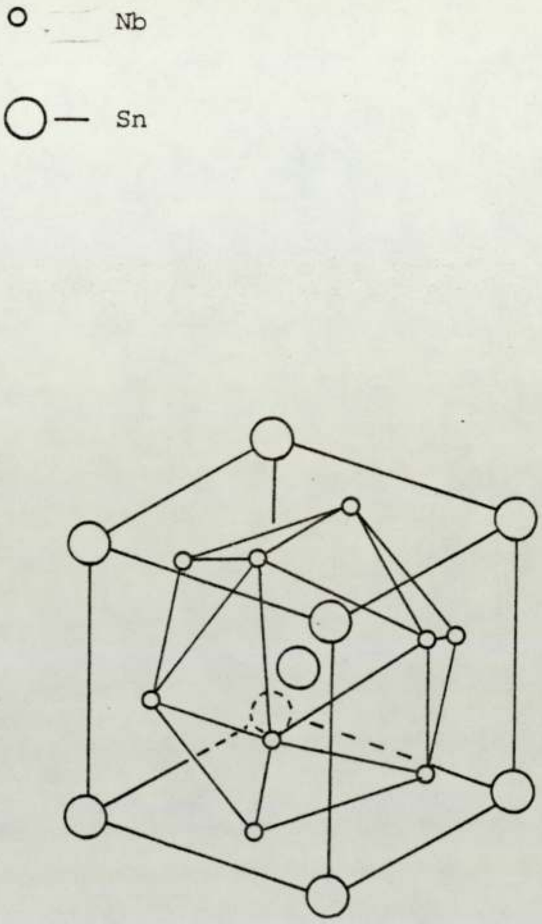

FIGURE 1.9 The Nb_3Sn (β-tungsten) structure, emphasizing the icosahedral co-ordination of Sn. (Grimes, 1976).

high T_c members of this group which is greatest for the highest T_c. Furthermore, he also suggested that McMillan's version of strong-coupling is able to predict T_c max not only for elemental structures but also for binary families of materials.

Other work concerned with looking into the reasons for high transition temperatures has been based upon electronic properties. In particular, the model of Labbé and Friedel (1967a) correlates an extremely narrow d- band in the electronic density of states near the Fermi Energy, $N(\varepsilon_F)$ with the high T_c members of the A15 group (e.g., Nb_3Sn). This model has been used to explain the occurrence of very soft TA modes in these compounds (Labbé and Friedel, 1967b). An important assumption is that the electron-phonon coupling does not change as the mode softens and that changes in $N(\varepsilon_F)$ are solely responsibile for both phenomena. However, as Ramakrishnan (1973) has pointed out, the softening of the lattice at a phase change merely produces those phonons (high frequency, TA) necessary for increased electron-phonon coupling and, therefore, enhanced T_c. Clearly lattice instability and high T_c cannot be separated and the degree of dependence of T_c on $N(\varepsilon_F)$ is not absolute.

1.5 Superconductivity amongst Compounds with the Spinel Structure

1.5.1 Spinel Compounds

Compounds having a molecular formula of the form $A B_2X_4$, in which A and B are metal ions and X is an anion, frequently crystallize with a structure related to that of the mineral $MgAl_2O_4$, known as Spinel. These compounds with spinel structure are conveniently classified into oxide, sulphide, selenide and telluride spinels according to the anion X^{2-}. The cations A and B in such compounds may be substituted by a wide range of metal ions. For example, a large variety of divalent cations may be substituted for Mg^{2+} in $\left[Mg^{2+}Al^{3+}O_4{}^{2-} \right]$, and almost any trivalent cation for Al^{3+}. Hence, it is perhaps not surprising to find that there are more than two hundred different kinds of spinels currently known.

Not only spinel itself but also a dozen or more minerals occur naturally (see Table 1.5). Some of them are commercially important metalliferous ores, while others have extensive uses in industry. However, for further details, the reader is referred to the general review of the modern application of the spinel materials by Grimes (1975).

1.5.2 The Spinel Structure

According to the conventional description, the Spinel structure is based upon a nearly close packed cubic arrangement of the anions in which the metal ions occupy certain interstitial positions. The essential features of the large unit cell, containing eight molecular units as shown in Plate 1.1 and also Figure 1.10, were first described by Nishikawa (1915) and by W. H. Bragg (1915) who studied both $MgAl_2O_4$ and Fe_3O_4.

Two types of interstices arise and, in the arrangement described as the Normal structure, ⅛ of the 64 possible tetrahedral positions (A-sites) are occupied by the divalent cations while ½ of the 32 possible octahedral interstices (B-sites) contain trivalent cations. The local site symmetries and overall symmetry then correspond to the crystallographic space group Fd3m, the details of which are given in Table 1.6. The cations are in special positions and the structure is centrosymmetrical about the B-site. The anion positions are specified completely through a single positional parameter, the u-parameter, which, for an ideal spinel where the oxygen sublattice is perfectly packed, has a value of 0.375.

In practice, u is often larger than this value, and for

TABLE 1.5

A selection of mineral spinels (Grimes, 1975).

Mineral	Characteristic
$MgAl_2O_4$	Spinel itself, base for natural gemstones.
$ZnAl_2O_4$	Gahnite, a transparent diamagnetic spinel.
$FeAl_2O_4$	Hercynite, a classical paramagnet.
γ-Fe_2O_3	Maghemite, a natural material for magnetic recording.
$FeCr_2O_4$	Chromite, the chrome ore of Rhodesia.
Mn_3O_4	Hausmannite, a natural tetragonal spinel.
Fe_3O_4	Magnetite, the ancient navigators' lodestone.
Fe_3S_4	Greigite, a ferrimagnetic semimetal.
$NiFe_2O_4$	Trevorite, a ferrimagnetic semiconductor.
$ZnFe_2O_4$	Franklinite, the paramagnetic ferrite.
$CuCo_2S_4$	Carrollite, a natural metallic spinel.
Fe_2TiO_4	Ulvöspinel, with giant magnetostrictive properties.
Mg_2SiO_4	The high pressure spinel polymorph of Forsterite, thought to comprise the inner mantle of the earth.

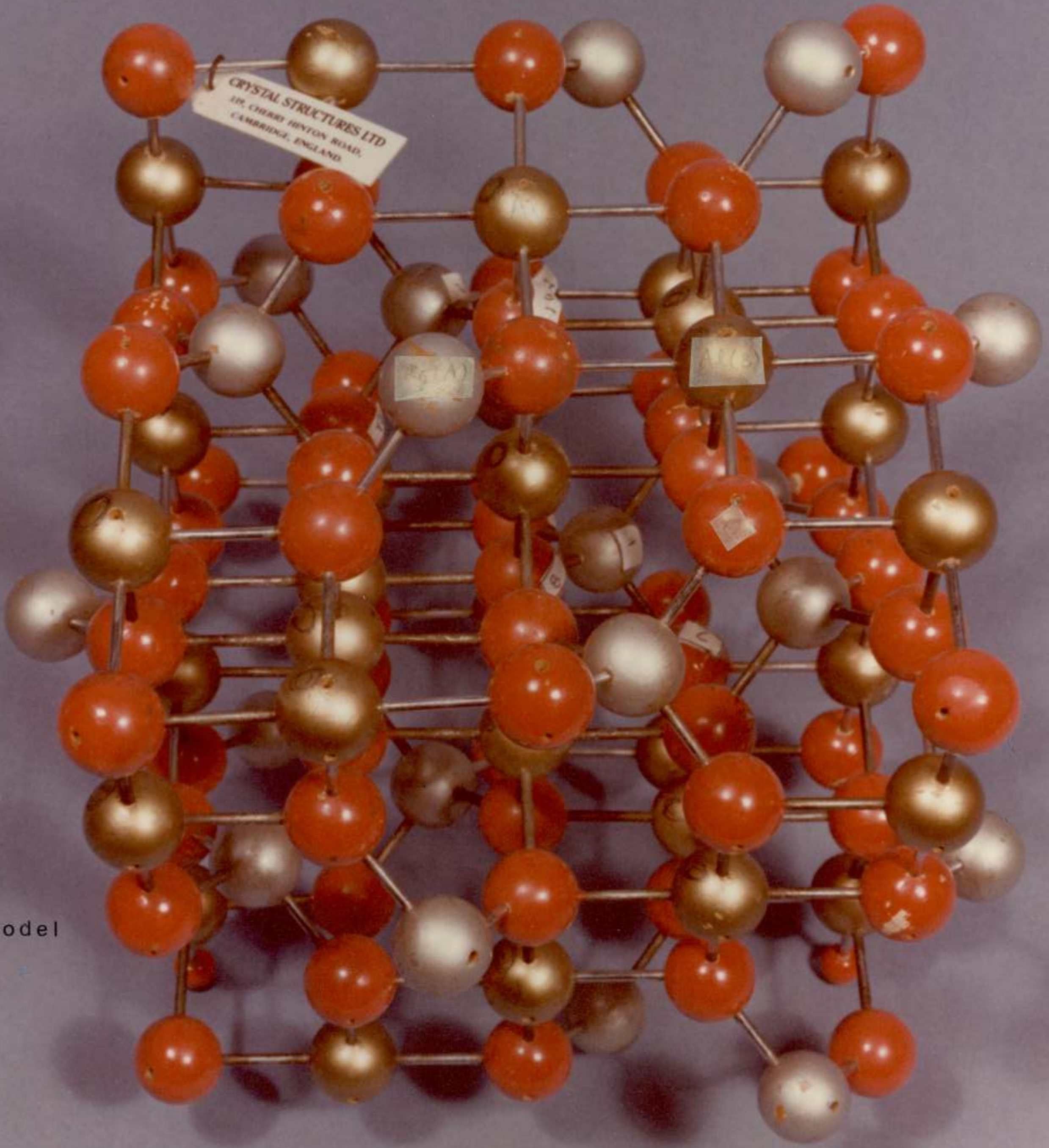

Plate 1.1 $MgAl_2O_4$
spinel model

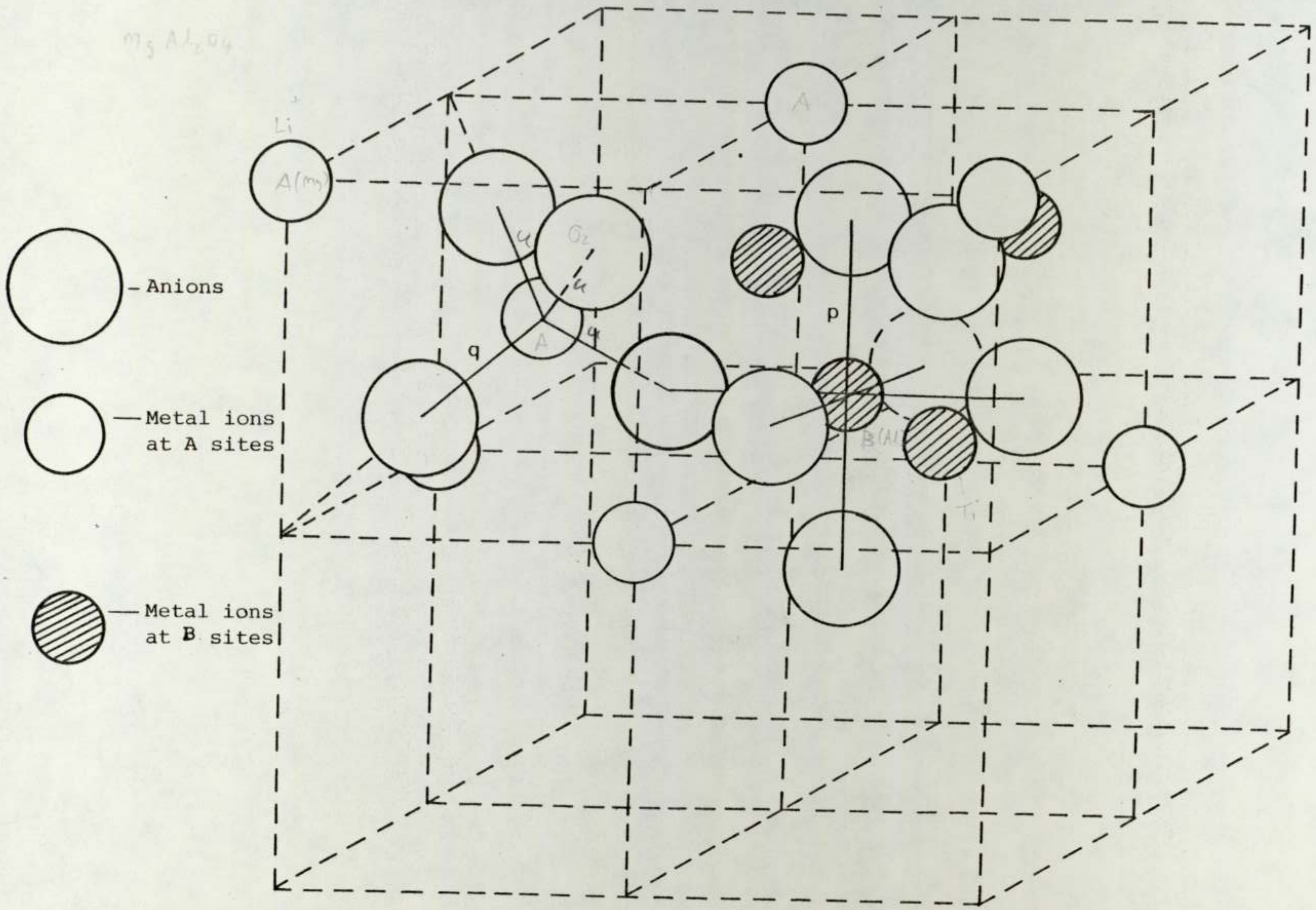

FIGURE 1.10 Spinel Structure (Gorter, 1954).

TABLE 1.6

Space group Fd3m : No 227

+ fcc translations $(0,0,0;\ 0,\frac{1}{2},\frac{1}{2};\ \frac{1}{2},0,\frac{1}{2};\ \frac{1}{2},\frac{1}{2},0;)$

(i) Origin at $\bar{4}3m$

Number of positions	Point symmetry	Fractional Coordinates
8 Mg	$\bar{4}3m$	$0,0,0;\ \frac{1}{4},\frac{1}{4},\frac{1}{4};$
16 Al	$\bar{3}m$	$\frac{5}{8},\frac{5}{8},\frac{5}{8};\ \frac{5}{8},\frac{7}{8},\frac{7}{8};$ $\frac{7}{8},\frac{5}{8},\frac{7}{8};\ \frac{7}{8},\frac{7}{8},\frac{5}{8};$
32 O	3m	$u,u,u;\ \frac{1}{4}-u,\frac{1}{4}-u,\frac{1}{4}-u;$ $u,\bar{u},\bar{u},\ \frac{1}{4}-u,\frac{1}{4}+u,\frac{1}{4}+u;$ $\bar{u},u,\bar{u},\ \frac{1}{4}+u,\frac{1}{4}-u,\frac{1}{4}+u;$ $\bar{u},\bar{u},u,\ \frac{1}{4}+u,\frac{1}{4}+u,\frac{1}{4}-u;$

(ii) Origin at centre $\bar{3}m$

Number of positions	Point symmetry	Fractional Coordinates
8	$\bar{4}3m$	$\frac{3}{8},\frac{3}{8},\frac{3}{8};\ \bar{\frac{3}{8}},\bar{\frac{3}{8}},\bar{\frac{3}{8}};$
16	$\bar{3}m$	$0,0,0;\ 0,\frac{1}{4},\frac{1}{4};\ \frac{1}{4},0,\frac{1}{4};\ \frac{1}{4},\frac{1}{4},0;$
32	3m	$x,x,x;\ x,\frac{1}{4}-x,\frac{1}{4}-x;$ $\bar{x},\bar{x},\bar{x};\ \bar{x},x-\frac{1}{4},x-\frac{1}{4};$ $\frac{1}{4}-x,x,\frac{1}{4}-x;\ \frac{1}{4}-x,\frac{1}{4}-x,x;$ $x-\frac{1}{4},\bar{x},x-\frac{1}{4};\ x-\frac{1}{4},x-\frac{1}{4},\bar{x};$

$u > 0.375$ the anions move in $< 111 >$ directions outwards from the nearest tetrahedral site cation. This movement destroys the perfect octahedral geometry surrounding the B-sites and results in a distortion from cubic point symmetry m3m to the lower trigonal point symmetry $\bar{3}$m.

In the description so far the cation distribution has been assumed to be that corresponding to the "Normal Spinel structure" which was thought for many years to be common to all compounds isomorphous with $MgAl_2O_4$. However, in 1932, Barth and Posnjak were able to prove that other distributions of the cations over the A and B-sites were possible. In one arrangement which they proposed, for example, the tetrahedral sites are occupied by half of the trivalent cations while the octahedral sites were shared randomly between the remaining trivalent cations and the divalent cations. This configuration is now known as the "Inverse Spinel structure" and is adopted by compounds like $NiFe_2O_4$. It is also possible for the cation distributions to be intermediate to the above cases, the structure then being said to be partially inverted (e.g., $NiAl_2O_4$). Sometimes, indeed, ordering of the different cations over the interstitial sites can take place and this leads to the formation of other structures with quite different overall symmetries, see for example Gorter (1954) and Cheary (1971).

1.5.3 Structural Distortions

In the description of spinel so far, the structure has been assumed to be cubic. However, crystallographic phase transitions from cubic to tetragonal or lower symmetry are extremely common among spinel compounds and these are thought to be caused by the presence of certain transition ions subject to the Jahn-Teller effect (Dunitz and Orgel, 1957). The transition ions concerned are Cu^{2+}, Fe^{2+} and Mn^{3+}. These ions, because of their particular electronic configurations, tend to produce instabilities when placed in a symmetrical environment. The consequence is usually to produce local distortions of the crystal structure which, at sufficiently low temperatures, can co-operate to give rise to an overall transformation to a structure of lower symmetry.

The existence of structural distortion in the cubic phase of spinels whose compositions include a Jahn-Teller ion was supported initially by the X-ray studies of Cervinka (1965) who found that the Debye-Waller factors of such compounds were usually rather higher than might be expected. Further evidence then emerged from investigations of the ^{57}Fe Mössbauer spectra in $FeCr_2O_4$ and FeV_2O_4 (Tanaka, Tokoro and Aiyama, 1966) and from studies of the infra-red absorption spectra in the spinel series $Mn_xFe_{3-x}O_4$ (Brabers, 1969).

In contrast to compounds of this kind, a cubic spinel series such as $Mg\left[Cr_xAl_{2-x}\right]O_4$, in which the octahedral sites are occupied by the Cr^{3+} ion, would be expected to remain free from structural distortion. Since magnetic susceptibility measurements on $MgCr_2O_4$ by Lotgering (1962) have shown that the electronic ground states of Cr^{3+} ion in the octahedral sites is without orbital degeneracy, Cr^{3+} is not a Jahn-Teller ion. Nevertheless, X-ray diffraction studies by Grimes and Hilleard (1970) showed that increasing chromium content in $MgCr_xAl_{2-x}O_4$ was accompanied by a substantial increase in the Debye-Waller factor in exact analogy with the earlier observations on the Jahn-Teller series, $Mn_xFe_{3-x}O_4$, made by Cervinka (1965). It was therefore concluded by Grimes (1971) that structural distortions must also exist in the chromite spinel series.

This conclusion is in agreement with the results from studies of the electron spin resonance spectrum of the Cr^{3+} ion in natural spinel by Stahl-Brada and Low (1959) which indicated an exceptionally strong trigonal field with a $[111]$ direction as an axis of symmetry. Very similar conclusions were reached by Lou and Ballentyne (1968) who observed the optical fluorescence spectra from a series of synthetic single crystals of the $Mg\left[Cr_xAl_{2-x}\right]O_4$ spinel group. Their results showed further that the distortions increase in severity with increasing chromium content and also that the site occupied by Cr^{3+} has 3m symmetry. This latter observation is incompatible with the crystallographic space group Fd3m to which the spinel structure is normally referred but is consistent with the results from the X-ray diffraction experiments and observations of infra-red absorption spectra by Grimes and Collett (1971) if the structure of $Mg\left[Cr_xAl_{2-x}\right]O_4$ spinels is described according to the space group F$\bar{4}$3m in which the network of octahedrally co-ordinated metal ions is modified so that alternate tetrahedral groups expand and contract (see Figure 1.11).

Finally, in recent examination of electron diffraction patterns from single crystals, weak reflections of the type $\{h\ k\ o\}$ with $(h + k) = 4n + 2$, i.e. (200), (420), (600), etc., have been observed for $MgAl_2O_4$ and $MgFe_2O_4$ by Hwang, Heuer and Mitchell (1973) and for $MnFe_2O_4$ by van den Berg, Lodder and Mensinga (1976). Such reflections are forbidden in the space group Fd3m but allowed under F$\bar{4}$3m.

An important feature of the newly discovered distortions is that they occur exclusively among the non-metallic spinels (Grimes, 1972) and this fact together with the absence of a Jahn-Teller effect led Grimes (1971) to propose that the distortions are produced as a consequence of the local potential conditions in the neighbourhood of the octahedral sites. This idea is supported by theoretical investigations by Hudson and Whitfield (1967) which indicate the presence of a potential maximum at the centre of the octahedral site and by Mössbauer experiments which reveal a negative electric field gradient

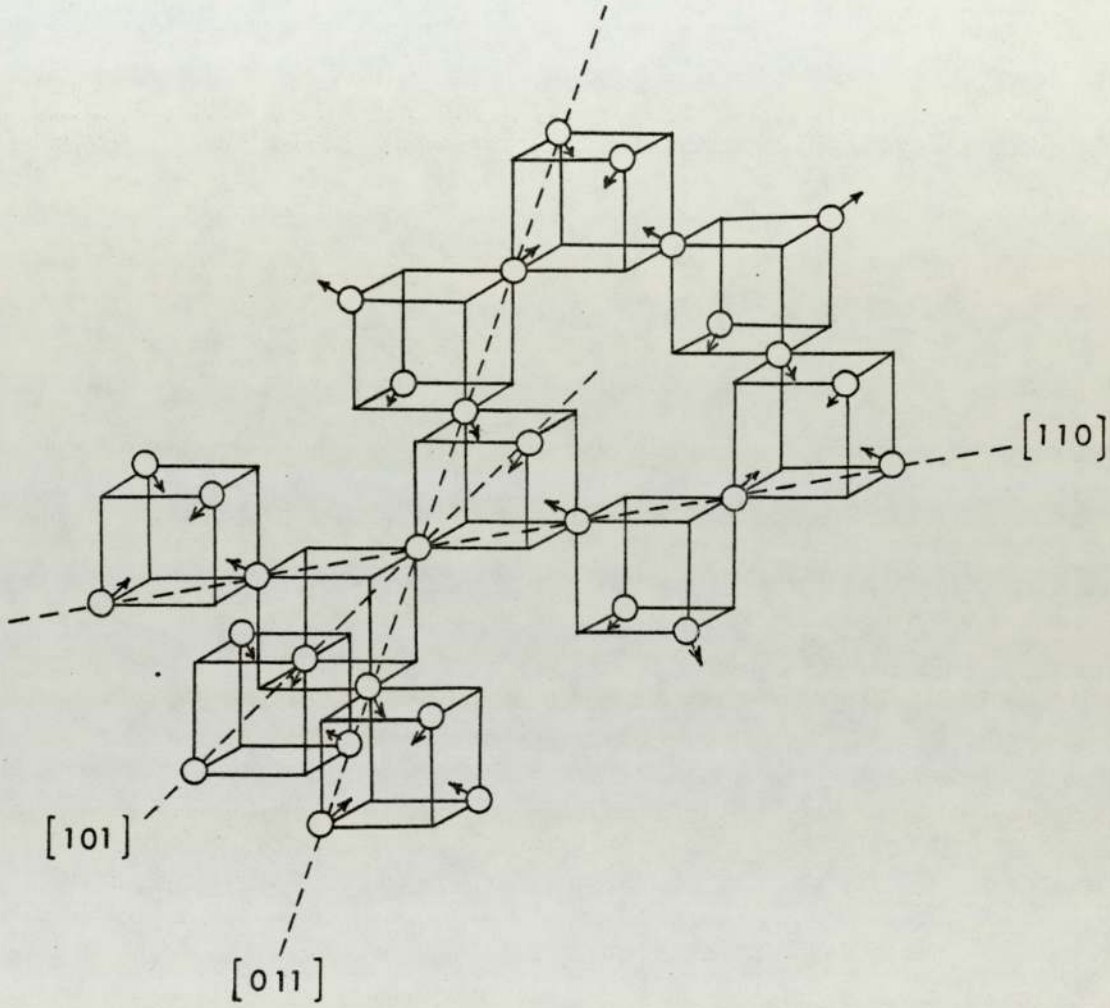

FIGURE 1.11 Octahedral ion sublattice (Grimes, 1973).

at this structural position in $ZnFe_2O_4$ and $CdFe_2O_4$ (Evans, Hafner and Weber, 1971). Further information concerning the new structural model has been derived from measurements of the heat capacity of $ZnFe_2O_4$, where analysis by Grimes (1974) suggests a potential distribution along a [111] axis through the octahedral site of the form shown in Figure 1.12, and a potential barrier between the two off-centre minima of 14.8×10^{-3}eV.

In contrast to this description, it is believed that off-centre ions cannot exist in the metallic spinels because of their good electrical conductivity and that in the case of these compounds the structure symmetry is best described by the space group Fd3m (see, for example, Williamson and Grimes, 1974). In certain circumstances, however, notably large anion to octahedral cation radius ratio, it has been suggested that the potential at the octahedral sites could be locally quite flat, so that the octahedrally co-ordinated cation is then anharmonically bound (Dawes and Grimes, 1975). Such conditions are now thought to be of importance in connection with the appearance of superconductivity among the metallic spinels.

1.5.4 The Superconducting Spinels

Superconductivity among spinels was discovered initially in the compounds $CuRh_2Se_4$, $CuRh_2S_4$ and CuV_2S_4 by van Maaren, Schaeffer and Lotgering (1967) and, independently, by Robbins, Willens and Miller (1967). Their results are given in Table 1.7 together with data from other authors. Even before this, however, it had been noted that these compounds are unusual. Thus, for example, Robbins (1967) had found $CuRh_2Se_4$ to be a p-type metal with a carrier concentration of about 5×10^{21} cm^{-3}. Similarly, Lotgering and van Stapele (1968) found $CuRh_2S_4$ and $CuRh_2Se_4$ to be paramagnetic while the corresponding chromium compounds $CuCr_2S_4$ and

Δ = Barrier height

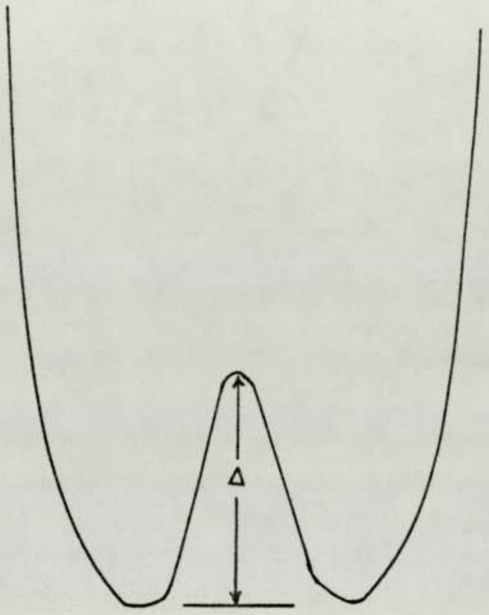

FIGURE 1.12 Potential energy distribution along a [111] axis through an octahedral site (Grimes, 1974).

TABLE 1.7

Crystallographic and superconducting properties

of selenide and sulphide spinels

Spinel	Lattice parameter (Å)	T_c °K	ΔT_c (°K)	Reference
$CuRh_2Se_4$	10.34	3.49	0.19	van Maaren et al. (1967)
	10.263	3.50	0.09	Robbins et al. (1967)
	-	3.48	-	Schaeffer et al. (1968)
	10.2603 ± 0.0004	3.50	0.50	Dawes and Grimes (1975)
	10.262 ± 0.002	3.49	0.02	Shelton et al. (1976)
	10.260 ± 0.001	3.38	0.01	
$CuRh_2S_4$	9.78	4.80	0.50	van Maaren et al. (1967)
	9.790 ± 0.001	4.35	0.38	Robbins et al. (1967)
	9.790 ± 0.001	4.37	-	Schaeffer et al. (1968)
	9.7877 ± 0.0005	4.07	0.7	Dawes and Grimes (1975)
	9.792 ± 0.001	3.81	0.05	Shelton et al. (1976)
	9.790 ± 0.001	4.70	0.10	
	9.787 ± 0.001	4.76	0.06	
CuV_2S_4	9.82	4.45	1.3	van Maaren et al. (1967)

$CuCr_2Se_4$ were ferromagnetic. More interestingly, and following the discovery of the superconducting properties, Robbins, Menth, Miksovsky and Sherwood (1970) were able to show from a magnetic and crystallographic investigation that, in the series $CuCr_{2-x}V_xS_4$, increasing V content led to increasing delocalization of the d-electrons associated with the octahedral transition metal (see, for example, Figure 1.13).

Cr^{3+}

This explains why the lattice of $CuCr_2S_4$ is smaller than CuV_2S_4

Detailed studies of the critical field and low temperature heat capacity of $CuRh_2S_4$ and $CuRh_2Se_4$ were made by Schaeffer and van Maaren (1968) who noted in particular, that these materials possess an unusually high density of states at the Fermi level. Subsequently, van Maaren and Harland (1969) investigated the Hall effect in the series $CuRh_{2-x}Sn_xSe_4$ and found dramatic changes in the apparent number of charge carriers per molecule and in the sign of the Hall coefficient, and concluded that conduction takes place in at least two bands, of which one has n-type character for $x < 0.5$ (see Figure 1.14). The superconductivity, in their view, was associated with the occurrence of electrons in this band and disappeared with the electron contribution to conductivity at $x \sim 0.5$.

Heat capacity measurements for the same series of specimens were reported in the following year by van Maaren, Harland and Havinga (1970) who analysed their results from these experiments to provide values for the coefficient of the electronic contribution γ . γ was expected to be proportional to $n^{-1/3}$, where n is the number of current carriers per mole, assuming a band of parabolic shape. They found, however, that γ was enhanced in the superconducting region of the compositional range ($x < 0.5$) indicating behaviour characteristic of a strong-coupled system rather than the expected BCS behaviour. Thus, knowing T_c and the Debye temperature θ from previous work, van Maaren et al. were able to calculate λ from McMillan's equation, 1.13, and hence with a suitable value of $\mu *$ the linear result illustrated in Figure 1.15 was obtained,

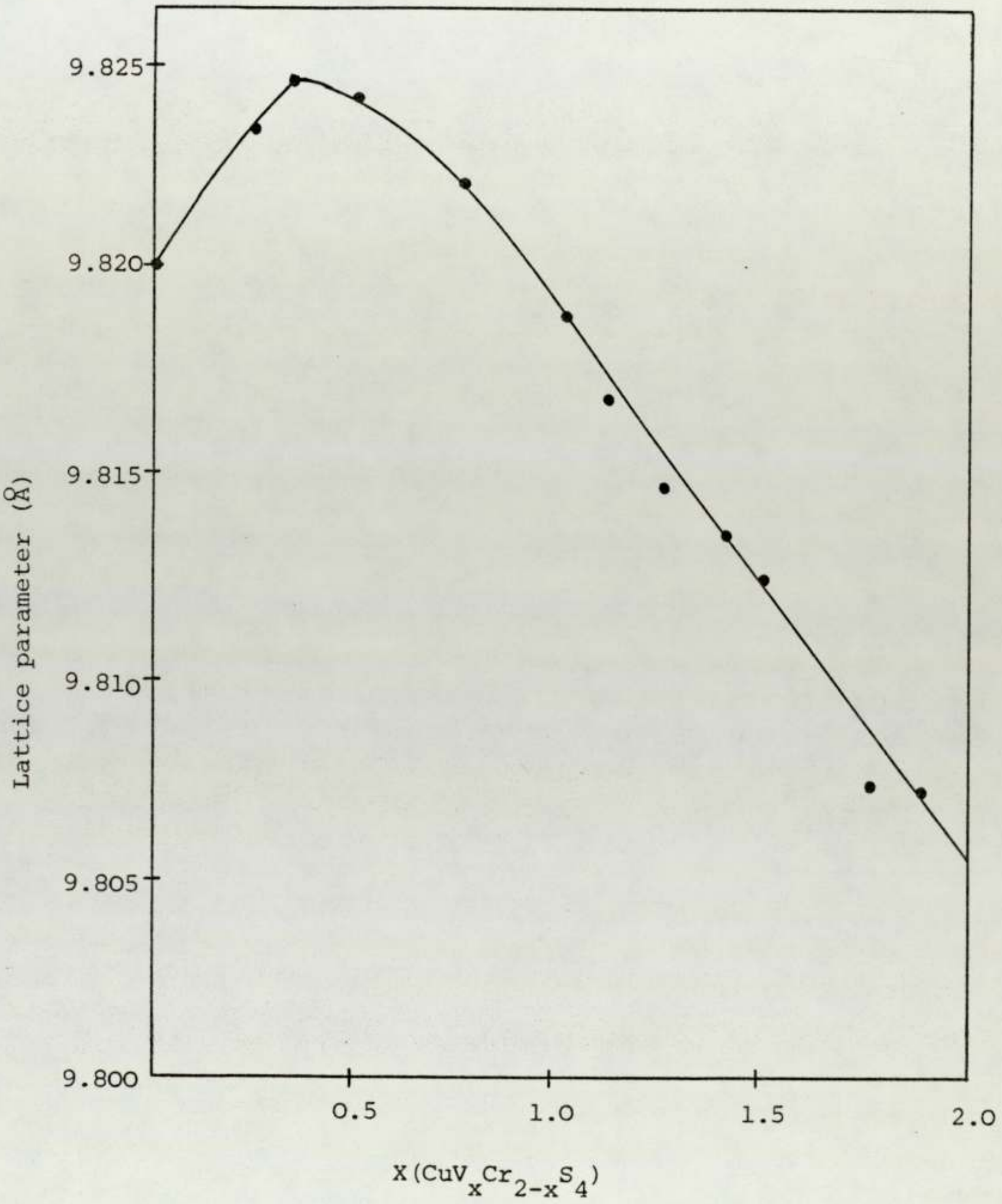

FIGURE 1.13 Lattice parameters versus composition (X) for the system CuV$_x$Cr$_{2-x}$S$_4$ (Robbins et al., 1970).

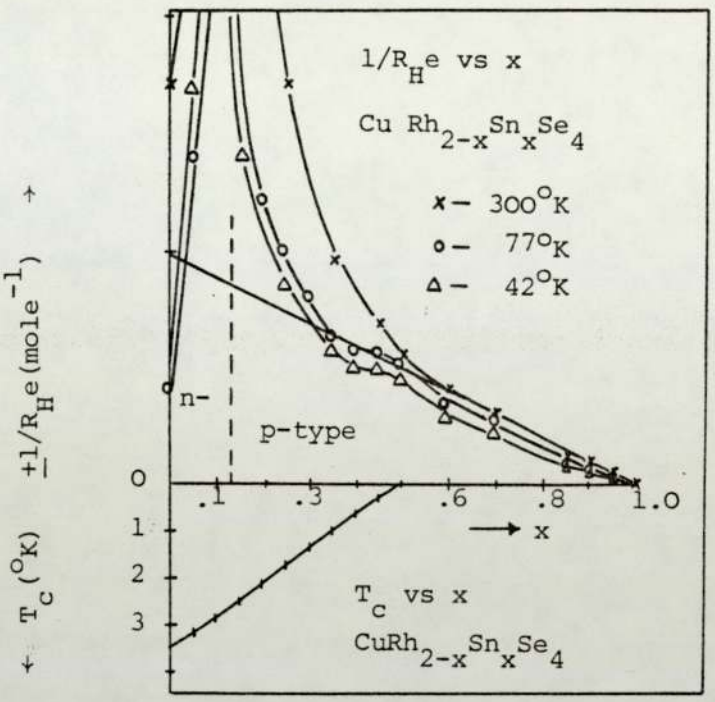

FIGURE 1.14 The apparent number of current carriers per molecule from $1/R_He$, and T_c, for $CuRh_{1-x}Sn_xSe_4$ (van Maaren et al., 1969).

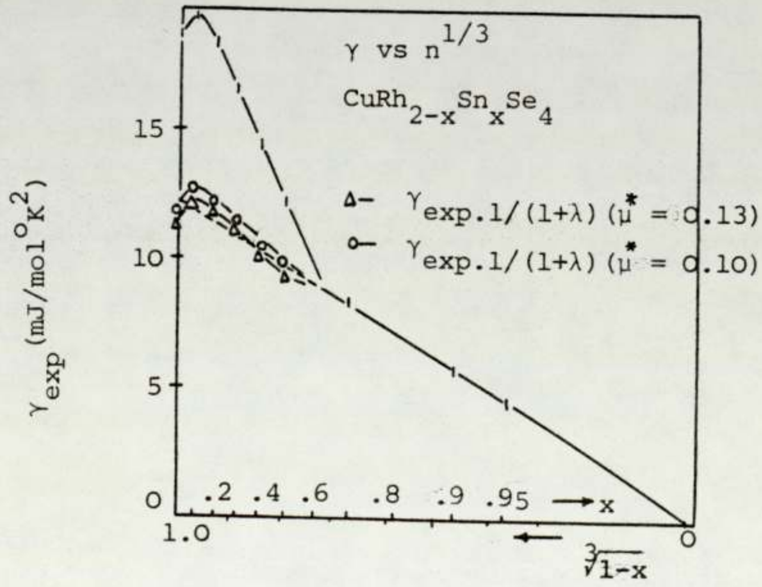

FIGURE 1.15 The electronic heat capacity coefficient, γ_{exp}, of $CuRh_{2-x}Sn_xSe_4$ as measured and after a phonon-enhancement correction (van Maaren et al., 1970).

this being interpreted as meaning that the change in shape at $x \sim 0.5$ is entirely due to strong coupling in the superconducting compositional range.

These conclusions, taken together with results from X-ray diffraction investigations of the same materials, led Dawes and Grimes (1975) to suggest that the mechanism for superconductivity in spinels was very closely allied to that existing in the A15 and NbN systems. The bond distances at the octahedral sites, in particular, seemed anomalously large, indicating weak bonding of the octahedrally co-ordinated cation and a locally flattened potential well.

Further evidence for the validity of this model for the superconducting mechanism was subsequently obtained by exploiting the Mössbauer effect to measure the recoil-free fraction of ^{119}Sn in the spinel series $CuRh_{2-x}Sn_xSe_4$ (Dawes, 1975). The isotope ^{119}Sn is one of the more suitable for Mössbauer investigations and was found to occupy the octahedral site throughout the superconducting compositional range. Again experimental results were consistent with the presence of anharmonicity and the flattened region of the potential well at the octahedral sites was estimated to have a mean diameter of the order of 0.1Å (Dawes, Grimes and O'Connor, 1974).

At about this time, an entirely new spinel superconductor, $LiTi_2O_4$, was discovered by Johnston, Prakash, Zachariasen and Viswanathan (1973), this material being remarkable because it is an oxide and possessed a transition temperature, T_c, which could be in excess of 13°K. $LiTi_2O_4$ can be regarded as one end member of a range of spinel phases in the Li-Ti-O system, the other end member being $Li_{4/3}Ti_{5/3}O_4$ which is a colourless electrical insulator. According to Johnston (1976), who studied the variation in T_c with composition x for $Li_{1+x}Ti_{2-x}O_4$ the compositions in the vicinity of $LiTi_2O_4 (x = 0)$ are all superconducting with a T_c which is nearly independent of composition but T_c decreases with increasing parameter x until no superconductivity is observed for $x \leqslant 0.1$. Electrical resistivity measurements, on the other hand, indicated that this disappearance of superconductivity was associated with a large increase in the resistivity at room temperature and with a quantitative change in its temperature dependence (Figure 1.16). This suggested that the occurrence of a composition-induced metal-semiconductor transition at about the same composition is the factor responsible for the disappearance of superconductivity. However, magnetic susceptibility measurements (Johnston, 1976) showed that, for all compositions studied within the homogeneity range of the spinel phase, the intrinsic susceptibilities are almost independent of temperature for most of the range below room temperature, indicating that, if a composition-induced metal-semiconductor transition does occur at $x \simeq 0.1$, this transition is not accompanied by discrete localization of the electrons outside of closed shells. Details of relevant superconducting parameters are given in Table 1.8.

In the same year, McCallum, Johnston, Luengo and Maple (1976) also made a detailed investigation of the heat capacity of $LiTi_2O_4$ compounds over the temperature range 1 - 25°K (see Table 1.9). These authors found that (a) the discontinuity of the heat capacity of the T_c, (b) the thermodynamic critical field at zero temperature and (c) the superconducting-state electronic heat capacity are all in close agreement with the predictions of the BCS theory of superconductivity. Since the electron-phonon coupling constant, λ , is much less than one and T_c is very much less than the Debye temperature, it was inferred that these materials belong to the class of weak-coupled superconductors. However, it is difficult to understand how this could be so in view of the evidence from the investigations of the $CuRh_2Se_4$ and $CuRh_2S_4$ systems and

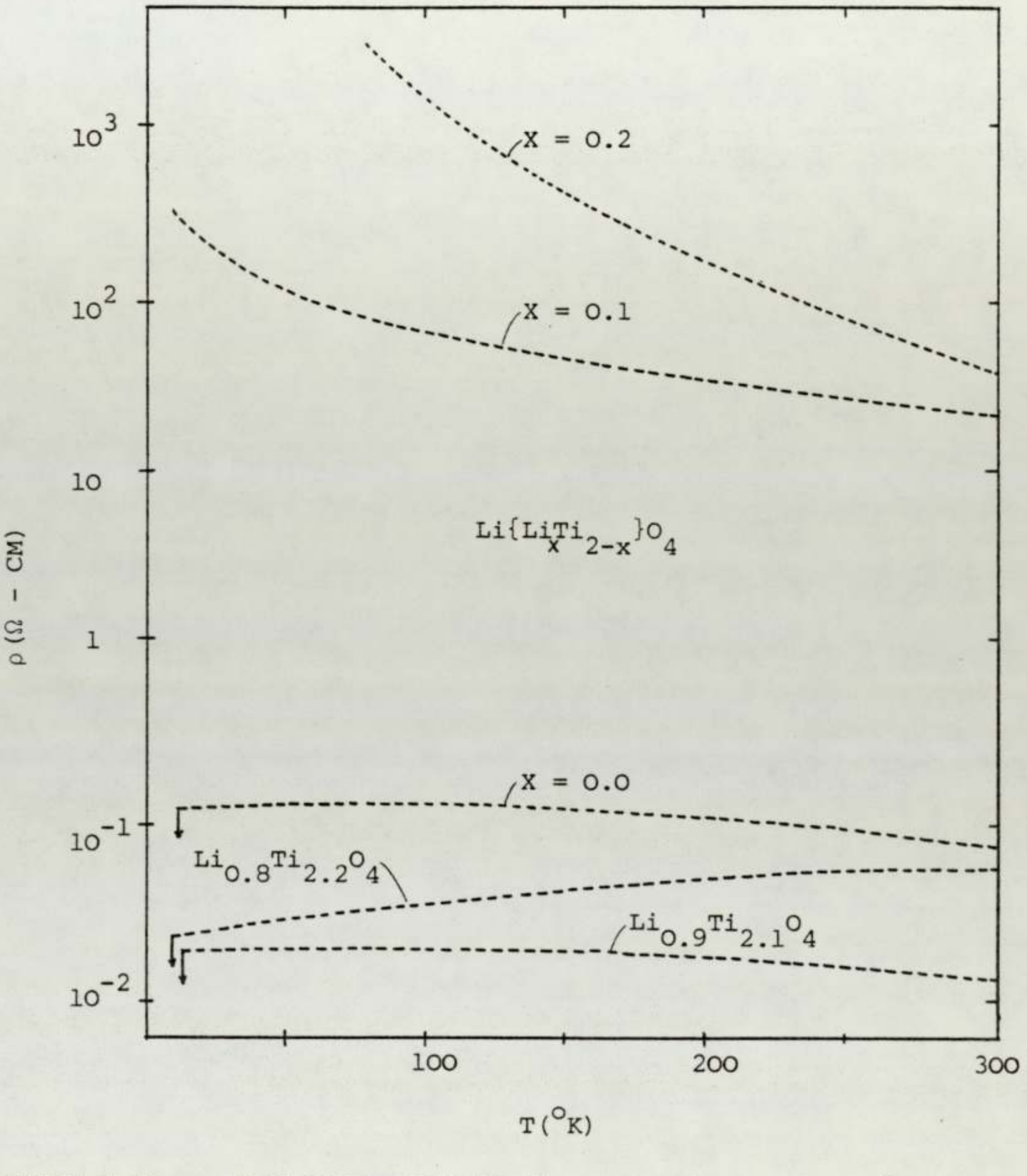

FIGURE 1.16 Electrical resistivity versus temperature for several $Li_{1+x}Ti_{2-x}O_4$ samples (Johnston, 1976).

TABLE 1.8

Electronic parameters characterizing the conduction electrons in $LiTi_2O_4$, derived from magnetic susceptibility measurements (Johnston, 1976).

Property	Value
(a) a_o, Å	8.402
(b) N/V, cm^{-3}	1.349×10^{22}
(c) V_m, cm^3/mole	44.67
(d) $\chi^{Pauli}_{free\ el.}$, cm^3/mole	23.5×10^{-6}
(e) χ_M, cm^3/mole ($T < 50^oK$)	220×10^{-6}
(f) m*/m	9.4
(g) $N(\varepsilon_F)$, states/eV-atom	0.97

a Lattice parameter.

b Conduction electron concentration.

c Molar volume.

d Calculated Pauli paramagnetism for free electrons.

e Measured susceptibility, corrected for impurity and ion core contributions.

f Conduction electron band structure effective mass.

g Density of electron energy states at the Fermi surface, for both electron spin directions.

TABLE 1.9

Heat capacity data and derived quantities for several $Li_{1+\chi}Ti_{2-\chi}O_4$ spinel compounds.

Quantity[a]	χ = 0.0[b]	χ = 0.05	χ = 0.1[c]	χ = 0.2	χ = 1/3
a_o, Å	8.407	8.400	8.384	8.374	8.359
V_m, cm^3/mole	44.75	44.64	44.38	44.23	43.99
γ, mJ/mole $°K^2$	21.4 (21.8)	19.7 (20.3)	10.9 (12.1)	3.6 (3.6)	0
β, mJ/mole $°K^4$	0.043 (0.029)	0.054 (0.037)	0.097 (0.064)	0.05 (0.066)	0.060
θ, °K	685 (774)	630 (716)	520 (598)	~650 (590)	610
α, mJ °K/mole	-	-	Small	29	-
T_c, °K	11.7	12.0	9.6	-	-
ΔT_c, °K	1.2	2.0	2.4	-	-
T_c/θ	0.0171 (0.0151)	0.0190 (0.0168)	0.0184 (0.0161)	- -	- -
$\Delta C/T_c$, mJ/mole $°K^2$	34	34	15	-	-

TABLE 1.9 (continued)

Quantity[a]	χ = 0.0[b]	χ = 0.05	χ = 0.1[c]	χ = 0.2	χ = 1/3
$\Delta C/\gamma T_c$	1.59 (1.56)	1.73 (1.68)	1.4 (1.2)	-	-
$H_c(0)$,G	1970	1970	-	-	-
$N(\varepsilon_F)(1+\lambda)$, states/eV atom	1.30 (1.32)	1.19 (1.23)	0.66 (0.73)	-	-

a The symbols are defined as follows: a_o, lattice parameter; V_m, molar volume; γ, β, and α, coefficients of the linear, cubic and inverse square temperature components of the normal state heat capacity; θ, Debye temperature; T_c, midpoint temperature of the superconducting transition; ΔT_c, superconducting transition width; ΔC, specific heat discontinuity at T_c; $H_c(0)$, thermodynamic critical field at zero temperature; $N(\varepsilon_F)$, band structure density of states at the Fermi level; λ, attractive electron-phonon interaction parameter.

b Nominal composition: $LiTi_2O_{3.95}$.

c Nominal composition: $Li_{1.1}Ti_{1.9}O_{3.95}$. (McCallum et al., 1976) the fact that $LiTi_2O_4$ has such a high transition temperature compared with that of any other known oxide superconductor (see, for example, comments by Matthias, 1975).

Finally, it should be noted that recent measurements of the upper critical field for several Li-Ti-O compounds (Foner and McNiff, 1976) indicate that these compounds possess a rather high value of critical field - 160 KGauss, similar to that found in the Chevrel compounds, $M_xMo_3S_4$, by Foner, McNiff and Alexander (1974).

1.6 Scope of the Present Work

From the review of the physical behaviour of the superconducting spinels outlined in Section 1.5, it will be evident that there is considerable scope for further work to be carried out before a proper understanding of these materials can be said to have been achieved.

In previous experimental work in our research group, Mössbauer investigations were carried out by Dawes (1975) to detect the presence of low temperature anharmonicity in the superconducting spinels through measurements of the recoil-free fraction of ^{119}Sn in the spinel series $CuRh_{2-x}Sn_xSe_4$. These measurements also provided new estimates for the electron-phonon interaction parameter, λ, and some indication of the validity of the McMillan theory as applied to spinels. Further information concerning anharmonicity, however, is clearly desirable and could be obtained from extended heat capacity measurements. A method of analysing the heat capacities of V_3X compounds, for example, has recently been described by Knapp, Bader, Culbert, Fradin and Klippert (1975) to provide a separated anharmonic component which may be related to λ and hence T_c for these materials. The principle of their method of data analysis, which was also used as the basis for the present investigation, is discussed in Chapter 2.

In the work to be described, attention has been concentrated upon making measurements of the heat capacity of two superconducting spinel compounds, $LiTi_2O_4$ and $CuRh_2Se_4$, over the temperature range 1.5 - 300°K. The apparatus used for these heat capacity measurements was designed and constructed as detailed in Chapter 3. The results of the measurements for $LiTi_2O_4$ and $CuRh_2Se_4$ are then presented in Chapter 4. Finally, these results are analysed and discussed at length in Chapter 5 and the main conclusions arising from this discussion brought together in summary in Chapter 6.

CHAPTER 2

THE MEASUREMENT OF ANHARMONICITY

CHAPTER 2

THE MEASUREMENT OF ANHARMONICITY

2.1 The Harmonic Approximation

It should be emphasized that, in describing experiments on the heat capacity of a solid, the parameter which is always measured is C_p, i.e., the heat capacity at constant pressure, because of the difficulty of preventing thermal expansion. Nevertheless, the forces between atoms in a solid are so large that a considerable amount of work is done against them in the small expansion which takes place and this effect is included in the internal energy which is the quantity of real theoretical interest (see, for example, Roberts and Miller, Heat and Thermodynamics, 4th Edition, 1951, page 209). Therefore, experimental data are always first corrected to constant volume before attempting a comparison with theory and this may be achieved via a suitable relation such as that due to Nernst and Lindemann:

$$C_p - C_v = AC_p^2T \qquad \ldots\ldots (2.1)$$

in which A is thought to be a nearly temperature independent constant which can be evaluated at, for example, room temperature, from the relation:

$$A \simeq \frac{9\alpha^2 V}{\beta C_p^2} \qquad \ldots\ldots (2.2)$$

where α = coefficient of linear expansion,

V = molar volume,

β = isothermal compressibility.

With this correction it is found that the heat capacity behaviour of simple solids is remarkably similar. In particular, near room temperature they all tend to have a value approaching 25 Joules per mole per $^{\circ}$K which is Dulong and Petit's Law and exhibit a decrease from this value with decreasing temperature. Moreover, the form of the heat capacity temperature dependence is nearly independent of the substance, i.e., there is a law of corresponding states:

$$C_V = f(\frac{T}{\theta}) \qquad \text{......} \quad (2.3)$$

where T is the absolute temperature and θ a characteristic temperature for the solid.

This very simple behaviour suggested, many years ago, that a crystal could usefully be regarded as a system of simple harmonic oscillators. For example, according to the theory proposed by Einstein (1907), it was supposed that there was some characteristic angular frequency, ω_E, with which each atom in a given solid would vibrate (Figure 2.1(a)). This assumption leads to the relation:

$$C_V = 3Nk_B \left(\frac{\theta_E}{T}\right)^2 \frac{\exp(\theta_E/T)}{\left[\exp(\theta_E/T) - 1\right]^2} \qquad \text{......} \quad (2.4)$$

where N is Avogadro's number, 6.022×10^{23} mole^{-1}, k_B the Boltzmann's constant and θ_E the Einstein characteristic temperature defined as $\hbar\,\omega_E/k_B$.

Although the Einstein theory leads to the Dulong-Petit limit at high temperature, it was not successful in providing an adequate explanation of the low temperature heat capacity behaviour, as equation (2.4) falls off too quickly with temperature in the neighbourhood of 0°K, i.e., $C_V \propto \exp(-\theta_E/T)$. Subsequently, Nernst and Lindemann (1911) pointed out that experimental observations could be fitted better if two frequencies, ω_E and $\frac{1}{2}\omega_E$, were used instead of ω_E alone. Nevertheless, significant discrepancies remained. The reason for this was that real solids actually possess a spectrum of vibrational frequencies and in the model proposed by Debye (1912), based on an isotropic continuum crystal, the frequency distribution is parabolic up to a certain limiting frequency, ω_D, as shown in Figure 2.1(b). In the Debye approximation, the velocity of sound, V_o, was taken as constant for all modes of vibration. The density of modes, $N(\omega)$, is then of the form:

$$N(\omega) = (3\omega^2 V/2\pi^2 V_o^3), \qquad 0 < \omega < \omega_D \qquad \text{......} \; (2.5)$$

The corresponding predicted heat capacity has the form:

$$C_V = 9Nk_B \left(\frac{T}{\theta}\right)^3 \int_o^{x_D} \frac{x^4 e^x}{(e^x - 1)^2} dx \qquad \text{......} \; (2.6)$$

where θ is the Debye characteristic temperature, $x = \hbar\omega/k_B T$ and $x_D = \hbar\,\omega_D/k_B T \equiv \frac{\theta}{T}$. The expression (2.6) behaves more satisfactorily at low temperatures ($T << \theta$) viz:

$$C_V = \frac{12\pi^4}{5} Nk_B \left(\frac{T}{\theta}\right)^3 \qquad \text{......} \; (2.7)$$

that is, C_V is proportional to T^3.

The Debye theory was so successful in describing the temperature dependence of the heat capacity of simple crystals that it was the basis for interpreting thermal behaviour for many years. Slowly however, when accurate values of heat capacity at low temperatures became available with improved calorimetric technique, it was found that equation (2.6) for C_V did not fit the experimental results exactly. For example, the Debye theory assumes a constant value for θ whereas, in practice, variations of θ with temperature are often observed (see, for example, Berg and Morrison, 1957).

The fundamental deficiency in the Debye theory is the inadequate treatment of effects arising from the discreteness of atomic arrangements in real crystals. The periodicity of the lattice causes the medium to be dispersive; i.e., the velocity of propagation of lattice

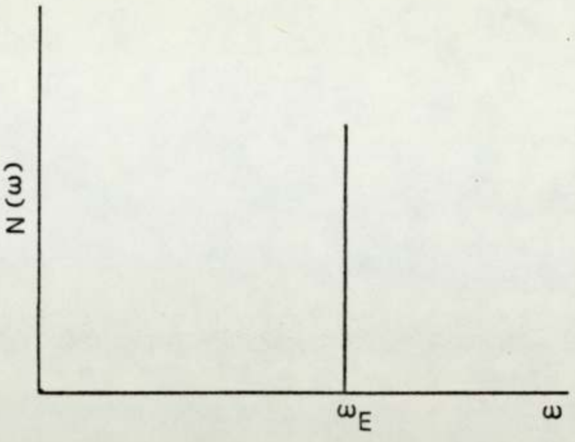

(a) Einstein

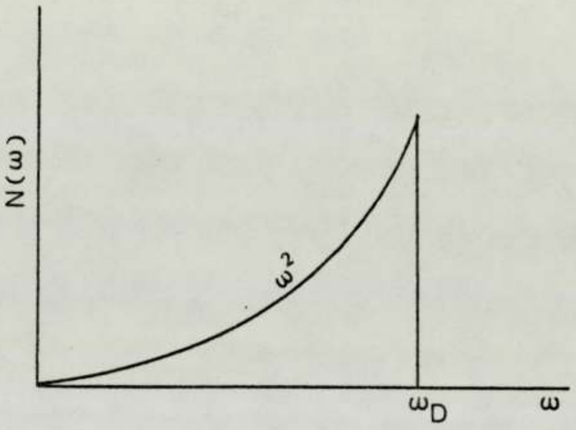

(b) Debye

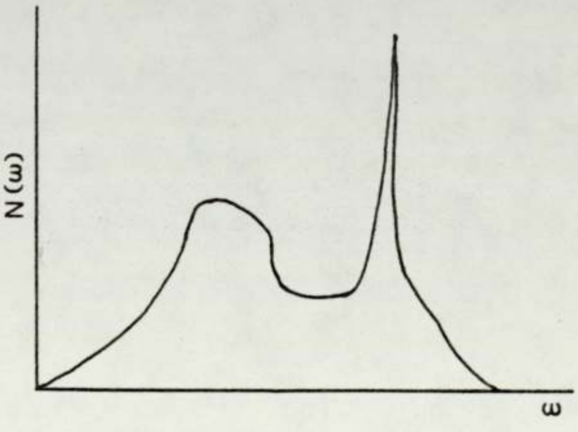

(c) Real Crystal

FIGURE 2.1 Mode spectra for the (a) Einstein and (b) Debye approximations and (c) Real Crystal.

waves is a function of their frequency. This phonon dispersion was correctly taken into account in the model proposed by Born and van Kármán (1912). In particular, they showed that a limiting wave vector rather than limiting frequency should be employed in heat capacity theory and therefore that the frequency distribution for a real solid cannot be as smooth as assumed by Debye but must possess considerable structure as shown in Figure 2.1(c). Moreover, they also distinguished between acoustic modes (where ω tends to zero as wave vector $\vec{q}$ tends to zero) and optic modes (where ω remains finite as $\vec{q}$ tends to zero) as well as between longitudinal and transverse polarization. This recognition of the complexity of vibrational spectrum is the real characteristic of the modern approach.

Finally, it should be emphasized that even this complex description of heat capacity temperature dependence neglects contributions which may arise from excitations other than the vibrational spectra.

2.2 Anharmonicity

2.2.1 Local Atomic Potential Wells

For an atom in a real crystal, the potential energy at a particular atomic location can be thought of as made up of two separate contributions, one long range and predominantly attractive and the other a short range repulsive component. In a simple ionic solid, for example, this potential energy might have the form:

$$V(r) = \frac{-Ae^2}{4\pi\varepsilon_o r} + B\exp\left(-\frac{r}{\rho}\right) \qquad \ldots\ldots (2.8)$$

where r is the nearest neighbour separation, e is the electronic charge and A, B and ρ are constants. Here, the first term is Coulombic and attractive (the Madelung energy) whilst the second is a repulsive Born-Mayer energy term which decreases very rapidly to negligible value with increasing r. Figure 2.2 shows the variation with r produced by adding these components, the total potential energy passing through a minimum value at $r = a$ which corresponds to the equilibrium separation of the positive and negative ions in the crystal at $0^{\circ}K$. In this region, the resultant of the sum of two terms is expected to be a potential function of approximately parabolic shape, i.e., $V(r)$ proportional to $(r - a)^2$.

In fact, if the potential wells were exactly parabolic, the harmonic model for the solid would also be exact and properties such as thermal conductivity and thermal expansion could not exist. In reality, the potential wells are not so ideal and deviate from the parabolic model in a manner and to an extent which depends upon the nature of the atomic interactions involved.

2.2.2 High Temperature Anharmonicity

It is assumed that for simple solids the parabolic approximation is a good one in the neighbourhood of the low temperature equilibrium atomic separation. At higher temperatures, however, the amplitude of vibration will be greater and also more asymmetric with respect to $r = a$. The deviation from the ideal parabolic curve may be represented by the expression:

$$V(r) = C(r - a)^2 - D(r - a)^3 - E(r - a)^4 \qquad \ldots\ldots (2.9)$$

where C, D and E are all positive coefficients which become successively smaller in magnitude. Discrepancies between the measured values of physical properties and the values predicted by harmonic theory are then attributed to the presence of the higher order terms.

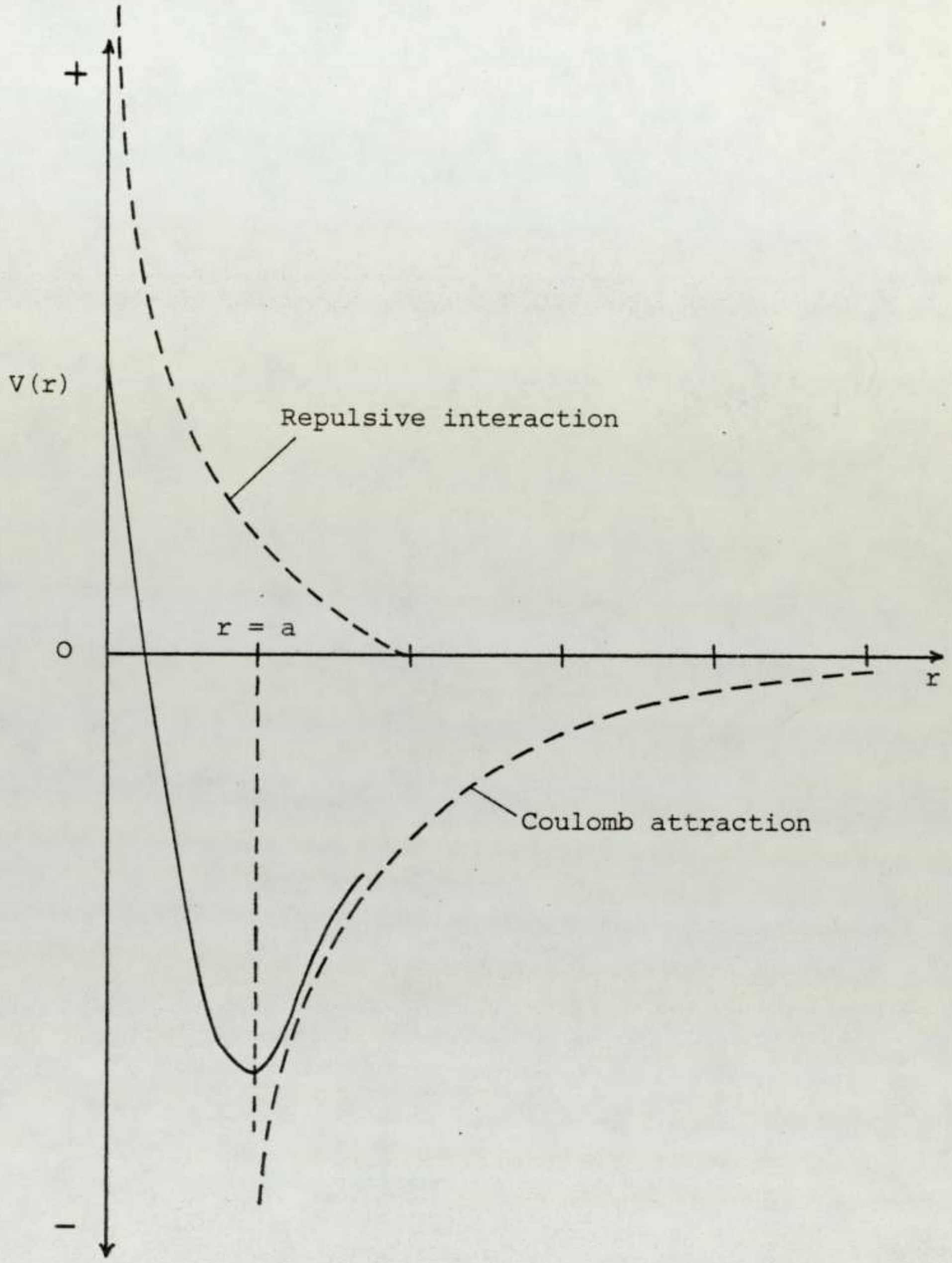

FIGURE 2.2 Potential energy of an ion in a crystal. The solid curve is the resultant of the sum of an attractive and repulsive component (both shown dotted).

2.2.3 Low Temperature Anharmonicity

The conditions described in Section 2.2.2 are not the only ones leading to anharmonicity. The existence of dipole moments owing to polarizability of some ions or covalency or, in the case of a metal, a free electron gas introduces a much more complex interaction. There are, in fact, a number of classes of materials for which the harmonic approximation is actually rather poor even at low temperatures. In some cases, it is now believed that the resultant V(r) may have a form with off-centre valleys as shown in Figure 2.3(a) while in others the attractive and repulsive parts may cancel over an appreciable range to give a potential well which is locally quite flat (see Figure 2.3(b)).

Examples of substances in which this kind of behaviour might occur have recently been reviewed by Dash, Johnson and Visscher (1968). These materials are thought to include ferroelectrics such as $BaTiO_3$, in which the Ti ions occupy wells with off-centre valleys, and high transition temperature superconductors like Nb_3Sn in which tin atoms occupy flat-bottomed wells.

Evidence for this includes Mössbauer effect (Shier and Taylor, 1967, 1968), acoustic relaxations (Testardi, 1972), anomalous thermal expansion behaviour (Smith, Finlayson and Shelton, 1975) and, most recently, heat capacity behaviour (Knapp et al., 1975). The information given by these different techniques, however, is not the same. For example, the Mössbauer effect measures the local binding of a particular atom to the crystal matrix through the recoil-free fraction and also, from the isomer shift, an indication of the electronic density of states (for details, see Shier and Taylor, 1968; Taylor and Craig, 1968; Kitchens, Taylor and Craig, 1970; Dawes, 1975).

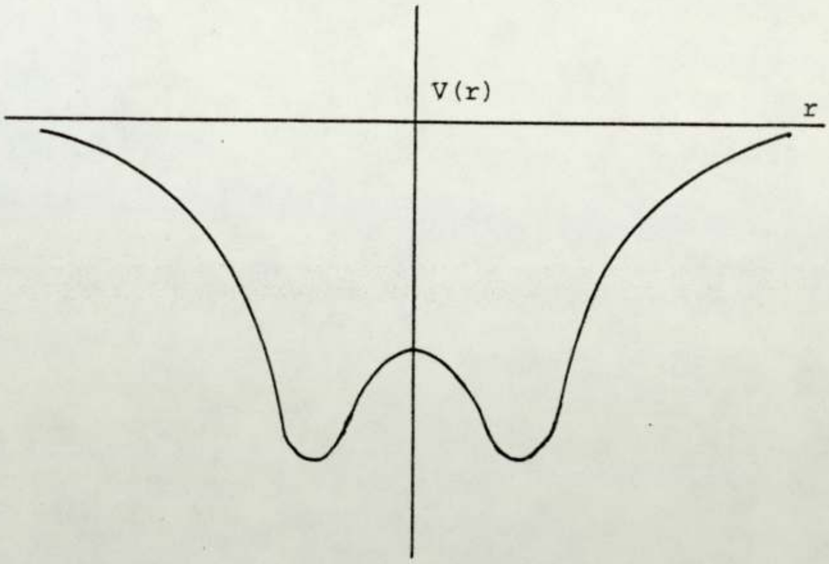

(a) Potential well with off centre valleys for ThO_2.

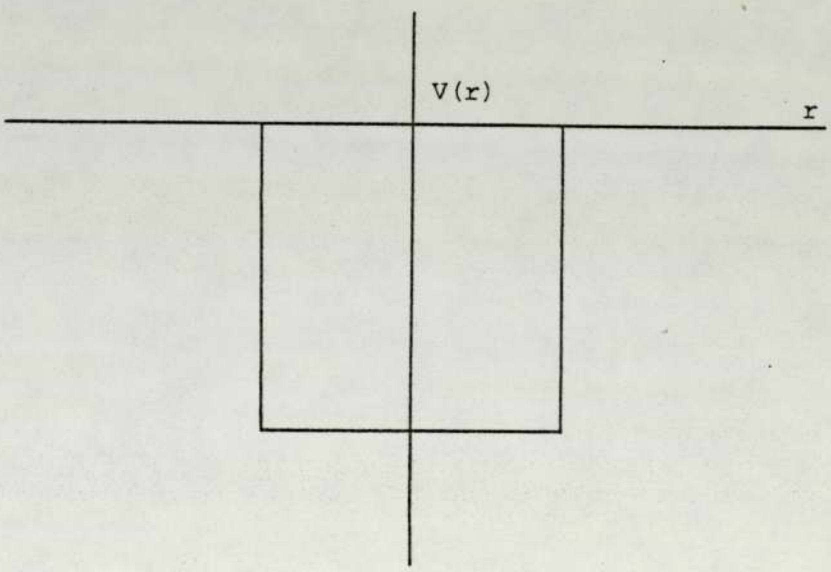

(b) Potential well model for Nb_3Sn.

FIGURE 2.3 (a) Potential well with off centre valleys for ThO_2 (Shechter, Dash, Erickson and Ingalls, 1970).
(b) Potential well model for Nb_3Sn (Dash, Johnson, and Visscher, 1968).

2.3 Anharmonic Contributions to Heat Capacity

As explained in Section 2.1, the conventional description of the temperature dependence of the heat capacity of simple solids is a harmonic theory and ignores not only elastic anisotropy but also any contributions arising from excitations other than the vibrational spectrum. Superconducting materials, however, especially those with high transition temperature, are generally metallic in character, so that their heat capacity invariably includes an important electronic component superimposed upon the dominant lattice contribution. For these materials therefore:

$$C_V = C_E + C_L \qquad \ldots\ldots \ (2.10)$$

where C_V is the total constant volume heat capacity, C_E is the conduction electronic contribution including electron-phonon renormalization effects and C_L, the lattice contribution including the effects of anharmonicity.

According to the current understanding of high T_c superconductivity, this last hidden term in the heat capacity might be expected to be anomalously large in certain circumstances. Therefore, there has recently been considerable interest in the possibility of devising a method of extracting the anharmonic component and in relating this quantity to the parameters of the strong coupling theory for superconductivity. In the method devised by Knapp and his collaborators (Knapp and Jones, 1972; Knapp, Bader, Culpert, Fradin and Klippert, 1975), this was considered as follows.

At low temperatures, C_V in the normal state can be represented by an odd power of T series:

$$C_V = \gamma . T + \frac{234R}{\theta_o^3} . T^3 + D.T^5 + \ldots\ldots \qquad \ldots\ldots \ (2.11)$$

in which the linear term is the electronic heat capacity which is related to the band structure electronic density of states at the Fermi surface, $N(\varepsilon_F)$ and to the electron-phonon interaction parameter, λ. In particular, since the electronic heat capacity coefficient is defined as $\gamma(T) = C_E(T)/T$, the low temperature coefficient:

$$\gamma_o = \lim_{T\to 0} \frac{C_E(T)}{T} = \frac{2}{3}\pi^2 k_B^2 N(\varepsilon_F)(1 + \lambda) \qquad \text{......} \; (2.12)$$

where k_B is Boltzmann's constant. γ_o can be quite accurately determined at low temperatures because the electronic contribution is then the dominant one. Moreover, for a superconductor, when the experimental data are fitted to the 3-term expansion of equation (2.11), there is the useful additional constraint that normal state and superconducting state entropies must be equal at T_c. The low-temperature Debye temperature, θ_o, and D are inevitably much less well characterized because the lattice contribution to the heat capacity is small in the low temperature region but the values for these parameters are not required for the separation of the anharmonic component.

At higher temperatures, the electron-phonon interaction parameter, λ, tends to zero and, indeed, according to Grimvall (1968), is already negligible at a temperature of $2\theta_D$. Above this temperature, therefore, γ is the band structure electronic heat capacity which at low temperature would be:

$$\gamma_b = \frac{2}{3}\pi^2 k_B N(\varepsilon_F) \qquad \text{......} \; (2.13)$$

where $$\gamma_o = \gamma_b(1 + \lambda) \qquad \text{......} \; (2.14)$$

According to Barron (1965) and Miller and Brockhouse (1971), the constant volume lattice entropy, S_L, of anharmonic crystals can be calculated, to at least their lowest order in anharmonicity, by using the frequencies determined by inelastic neutron scattering in the appropriate quasi-harmonic expression, viz:

$$S_L = k_B \sum_{s=1}^{3N} \{ \beta\hbar\omega_s n_s + \ln(n_s + 1) \} \qquad \ldots\ldots (2.15)$$

where $\beta = {}^1/k_BT$, $n_s = \{ \exp(\beta \hbar \omega_s) - 1\}^{-1}$ and ω_s is the phonon frequency of the normal mode s observed at temperature T, and is now temperature dependent. The corresponding heat capacity is given by:

$$C_L = T\left(\frac{\partial S}{\partial T}\right)_V = k_B \sum_{s=1}^{3N} n_s(n_s + 1)(\beta \hbar \omega_s)^2 \left(1 - \frac{T\omega'_s}{\omega_s}\right) \qquad \ldots\ldots (2.16)$$

where $\omega'_s = \{(\partial\omega_s)/(\partial T)\}_V$. Thus, for small anharmonicity, $k_BT \Sigma\, \omega'_s/\omega_s << 1$, and, in the high temperature limit, the lattice heat capacity can be expressed in the form:

$$C_L = 3R\left(1 - \frac{\hbar^2 < \omega_s^2 >}{12(k_BT)^2}\right) - k_BT \sum_{s=1}^{3N} \frac{\omega'_s}{\omega_s} \qquad \ldots\ldots (2.17)$$

where $< \omega^2_s > = \frac{1}{3N} \sum_{s=1}^{3N} \omega^2_s$.

At high temperatures, the lattice heat capacity in equation (2.17) approaches its classical Dulong-Petit value, 3R, due to the vanishing of a T^{-2} temperature dependence term, as in harmonic theory, with in addition, a linear term associated with the anharmonicity. At the temperatures at which equation (2.17) is valid, the electronic heat capacity is approximately linear in temperature, $C_E = \gamma T$, and the electron-phonon renormalization effects are unimportant. Including the electronic heat capacity, then, equation (2.17) can be re-written as:

$$\frac{C_V - 3R}{T} = -\frac{R\hbar^2 < \omega_s^2 >}{4k_B^2T^3} + (A + \gamma) \qquad \ldots\ldots (2.18)$$

where

$$A = -k_B \sum_{s=1}^{3N} \frac{\omega'_s}{\omega_s} \qquad \ldots\ldots (2.19)$$

so that a plot of high temperature data in the form $(C_V - 3R)/T$ versus T^{-3} should be a straight line whose slope provides the value of $<\omega_s^2>$, i.e., a high-temperature characteristic phonon temperature:

$$\theta_\infty = \left(\frac{5}{3}\frac{\hbar^2 < \omega_s^2 >}{k_B^2}\right)^{\frac{1}{2}} \qquad \text{...... (2.20)}$$

while the high-temperature intercept, $T^{-3} = 0$, yields $A + \gamma$, the sum of the electronic and anharmonic linear heat capacity coefficients (see Figure 2.4).

The validity of this procedure was illustrated by Knapp and his collaborators by analysis of the heat capacities of a number of vanadium-based A15 superconductors - see Figure 2.4. In each case, a good straight line for $(C_V - 3R)/T$ versus T^{-3} was obtained, the intercepts giving values for $A + \gamma$ and it was shown that there was a strong correlation between these values and the corresponding superconducting transition temperatures, T_c, (see Tables 2.1 and 2.2). The sum of $A + \gamma$ was then decoupled in two steps:

(i) the low-temperature γ_b was obtained from the expression $\gamma_b = \gamma_o(1 + \lambda)^{-1}$, using λ obtained from McMillan's formula (1.13) which is re-written in a convenient form finding an empirical electron-phonon coupling constant, λ , from the experimentally determined transition temperature, T_c, and Debye temperature, θ :

$$\lambda = \frac{1.04 + \mu^* \ln(\theta/1.45\,T_c)}{(1 - 0.62\,\mu^*)\ln(\theta/1.45\,T_c) - 1.04} \qquad \text{...... (2.21)}$$

where $\theta = \theta_\infty$ and $\mu^* = 0.13$.

(ii) the high-temperature γ was then obtained using γ_b, measured temperature dependencies of the magnetic susceptibility, T_1T

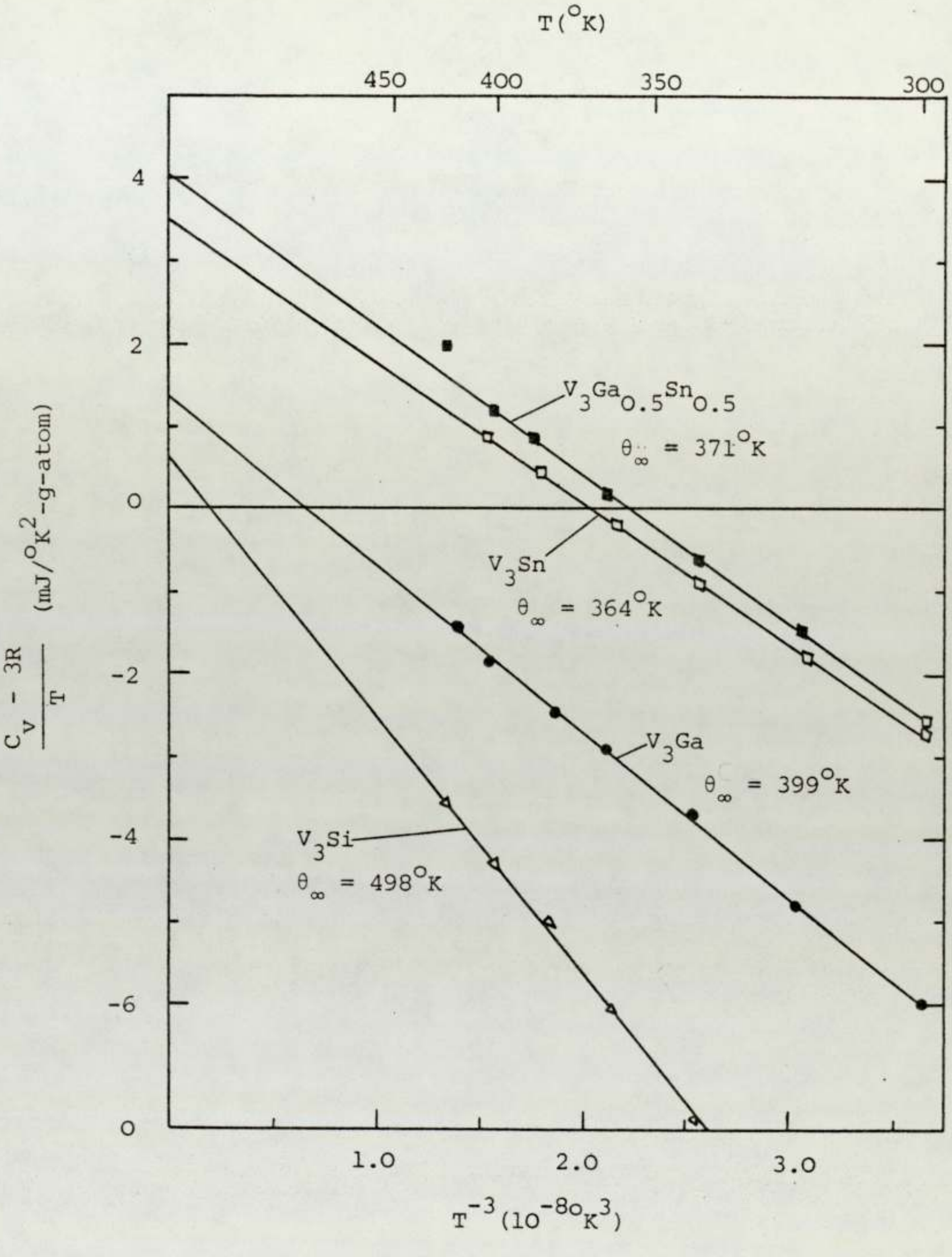

FIGURE 2.4 Heat capacities of the indicated vanadium-base A-15 superconductors plotted as $(C_v - 3R)/T$ vs T^{-3}. The slopes provide the values of $< \omega_s^2 >$, and hence θ_∞. The $T^{-3}=0$ intercepts provide the combined electronic and anharmonic linear heat capacity coefficients at high temperature (Knapp et al., 1975).

TABLE 2.1

The low temperature electronic heat capacity coefficient, γ_o, the band structure electronic heat capacity coefficient, $\gamma_b = \gamma_o(1+\lambda)^{-1}$, and the low temperature Debye temperature, θ_o, for vanadium-base compounds (Knapp et al., 1975).

Compounds	γ_o (mJ/$^oK^2$ g-atom)	γ_b (mJ/$^oK^2$ g-atom)	θ_o (^oK)
V_3Si	16.7	9.18	442 ± 40
V_3Ga	20.3	11.0	343 ± 30
$V_3Ga_{0.5}Sn_{0.5}$	10.2	6.30	321 ± 10
V_3Sn	7.22	4.63	318 ± 10

TABLE 2.2

Various parameters found in high temperature analysis of the heat capacity data. The units of γ and A are mJ/$^oK^2$ g-atom. (Knapp et al., 1975).

Compounds	T_c (^oK)	θ_∞ (^oK)	ϕ (^oK)	γ + A	γ	A
V_3Si	16.5	498	540 ± 150	0.5 ± 1.2	5.4 ± 0.6	-4.9 ± 0.6
V_3Ga	14.3	399	390 ± 120	1.4 ± 1.5	5.6 ± 0.6	-4.2 ± 0.9
$V_3Ga_{0.5}Sn_{0.5}$	5.6	371	4061 ± 320	4.0 ± 1.3	5.8 ± 0.8	-1.8 ± 0.5
V_3Sn	3.8	361	5500 ± 1500	3.6 ± 0.7	4.3 ± 0.2	-0.7 ± 0.5

(where T_1 is the ^{51}V nuclear spin-lattice relaxation time) and, finally, results of model density-of-states computations of the relative temperature dependence of the band structure γ , Pauli susceptibility χ_p, and T_1T.

It should be noted that the complexity of this second stage is really a reflection of the effort required to derive a good approximation to the temperature dependence of γ . At very high temperatures, γ must tend to zero but in the intermediate range may be sensitive to the structure of the electronic density of states. Therefore, the accuracy with which A can be derived must depend on the extent of this sensitivity. Further discussion of this point is deferred until Chapter 5.

CHAPTER 3

SAMPLE PREPARATION AND HEAT CAPACITY APPARATUS

CHAPTER 3

SAMPLE PREPARATION AND HEAT CAPACITY APPARATUS

3.1 Preparation of Samples

Polycrystalline samples having spinel structure can be synthesized by various methods, all of which depend on the degree of homogeneity of a reactant 'mix' as well as the temperature at which the reaction takes place. The sintering method of preparation, for example, consists of compressing and firing suitable reactants at a certain temperature for a certain period of time. In order to obtain a good mix via this method, and also to ensure that the diffusion process can take place, the basic elements have to be brought close together by compressing the mixture under several tons pressure so as to produce a high density. The firing temperature is similarly important because diffusion will not occur if the temperature is too low while if the temperature is too high there is a danger that any spinel phase will decompose.

In addition to the firing temperature, the atmosphere in which the reaction takes place can be a crucial factor, for the degree of sample stoichiometry and impurity may depend on this. However, in some cases, particularly among the oxide spinels, the impurity and lack of stoichiometry arising from this factor can often be alleviated by re-grinding and re-firing the sample several times. Here, the term "stoichiometric" refers to the initial reactant mix and the term "impurity" refers to the foreign phase developed during the process. For oxide spinels, the reactants may be fired in a flowing atmosphere of oxygen, hydrogen, etc; however, it is difficult to obtain a continuously flushed atmosphere for sulphide and selenide spinels. In these latter cases, in order to contain the gaseous elements and, thus, prevent them from being lost from the system, the reactants must be sealed in evacuated tubes. Indeed, one of the difficulties in the preparation of such spinels is that the sample tends to decompose before the reaction is completed.

3.1.1 Preparation of $CuRh_2Se_4$

Previous studies of the preparation of sulphide and selenide spinels by Dawes (1975) have suggested that the firing of a stoichiometric mixture of elements in an evacuated silica tube is the most suitable method for these materials. However, due to the cost of rhodium, the difficulties involved in obtaining the single phase spinels and the limited time available, it was decided that rather than embark on an extensive investigation of the ideal conditions for preparing these compounds, only $CuRh_2Se_4$ spinel would be studied. For this preparation, a mixture of fine powders, less than 100 μm in particle size, of high purity, (more than 99.9% pure as supplied by Koch-Light Ltd.), was prepared following pre-calculation of the weights of the various materials according to the formula:

$$Cu + 2Rh + 4Se \longrightarrow CuRh_2Se_4 \qquad \ldots\ldots (3.1)$$

Weighing was carried out to an accuracy of more than 0.5%; while the error arising from the transfer of elements was kept to a minimum. The elements were thoroughly ground together using a mortar and pestle until visual homogeneity had been achieved. The ground powder was loaded into a steel press with 15 mm diameter polished dies (Plate 3.1), which had been cleaned with acetone, before being pressed under 3 tons pressure into a pellet of approximately 2 gm in weight. However, in the case of electrical resistivity measurements, higher pressures of up

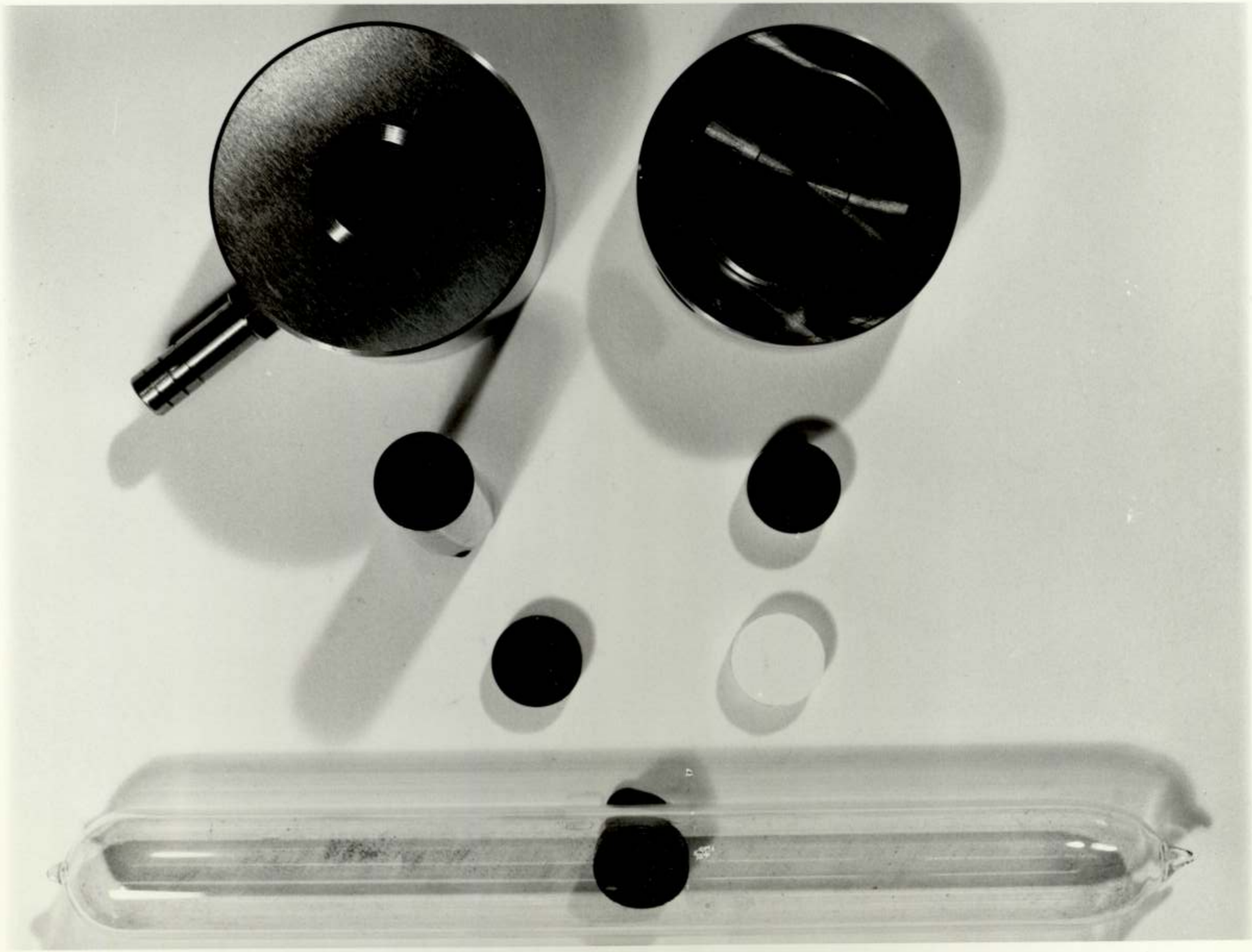

Plate 3.1 Apparatus for Pellet Preparation

to 14 tons were needed to produce a sample in the form of a harder pellet of higher conductivity after sintering.

The pressed pellet was then sealed in an evacuated silica tube (see Figure 3.1), connected to a vacuum line for evacuating to below 10^{-5} torr, flushed thoroughly with pure argon before being re-evacuated. To ensure that the sample was dry, this process was repeated three times, after which the tube was immediately sealed off. Since earlier experiments by Dawes (1975) had shown that a residual pressure $\sim$ 100 torr of argon or helium improves the purity of $CuRh_2Se_4$, a similar practice was adopted throughout this work.

Finally, the sealed tube was heated in a square furnace (Plate 3.2) having a 6 in. "hot zone" with alumina packing around the silica tube. After ensuring that the specimen was in the centre of the hot zone, the temperature of the furnace was allowed to rise slowly to the required value, by means of the temperature controller, to within an accuracy of $\pm 5^{\circ}C$. Although literature reports have suggested a temperature of $800^{\circ}C$ for at least 48 hours for $CuRh_2Se_4$, Dawes found that the reaction was complete within 24 hours and that optimum purity, resulting in a sharp transition temperature, was obtained at a temperature of $600^{\circ}C$ for 48 hours. The latter conditions were, therefore, used for all samples of $CuRh_2Se_4$.

3.1.2 Preparation of $LiTi_2O_4$

Of the several hundred known oxide spinel compounds, only $LiTi_2O_4$ has been found to be superconducting, having, in addition, a high T_c compared with most other oxide superconductors. Consequently, during the course of this work, consideration of the properties of superconductivity in oxide spinel compounds has been limited to $LiTi_2O_4$.

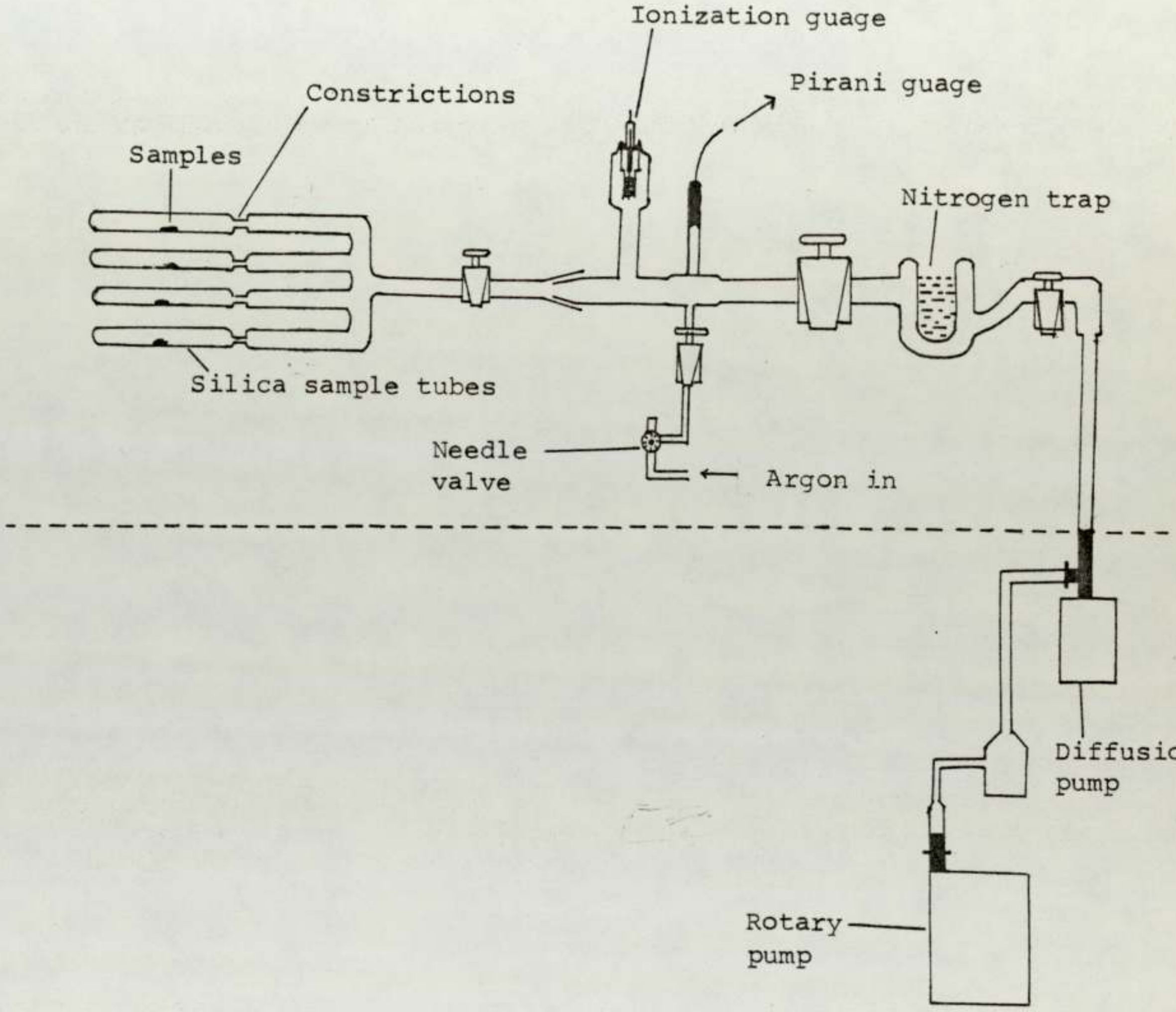

FIGURE 3.1 An Evacuable tube system

Now in the case of oxide spinels, it is usually possible to fire the reactants directly, provided a suitable gas environment is chosen. High transition temperature superconductors, however, have generally been found to be difficult to prepare and $LiTi_2O_4$ has been found to be no exception. Thus, in the experiments carried out by Johnston, Prakash, Zachariasen and Viswanathan (1973) and Johnston (1976), several methods of preparation were tried including (i) the arc-melting of Li_2CO_3, TiO_2 and Ti metal together, (ii) the sintering of mixtures of $Li_2Ti_2O_5$ and Ti_2O_3 under a helium or argon atmosphere and (iii) an attempt to obtain direct synthesis from Li_2CO_3, TiO_{15} and TiO_2, this latter method involving the pressing together of appropriate quantities of Li_2CO_3 and TiO_2 (pre-dried in oxygen) into a pellet, firing in a pure oxygen atmosphere, before grinding together with $TiO_{1.5}$. In this case, the final ground pellet was sealed in a pre-fused quartz tube under helium gas and fired at 750°C - 800°C for 12 - 24 hours. All of these methods, however, tended to produce multi-phase samples and to incur a weight loss during the process such that the final composition was not known precisely.

In an attempt to obtain the single phase spinel of $LiTi_2O_4$ in our laboratory, various gases have been used to flush out the reactants during the sintering and cooling stages of preparation - see Table 3.1 for details. The most successful method of preparation was found to be to sinter a stoichiometric mixture of Li_2CO_3 and TiO_2, under a hydrogen atmosphere, according to the equation:

$$Li_2CO_3 + 4TiO_2 \xrightarrow{H_2} 2LiTi_2O_4 + CO_2\uparrow + H_2O\uparrow \qquad \text{......} \ (3.2)$$

(The Li_2CO_3, of stated purity 99.9%, was obtained from Hopkin & Williams Limited and the TiO_2, of 99.9% purity, from Hopkin & Williams Limited).

Appropriate quantities of Li_2CO_3 and TiO_2 were thoroughly

Sintering Conditions			Remarks
24 h	800°C	in N_2 gas	White, insulator, not spinel.
24 h	800°C	in coal gas after sintered in N_2 gas	Creamy, insulator, not spinel.
24 h	800°C	in coal gas	Gray, poor conductor, spinel + unknown impurity.
24 h	800°C	H_2 gas after sintered twice in N_2 gas and once in coal gas	Gray, poor conductor.
24 h	800°C	in H_2 gas	Dark blue, spinel + Li_2TiO_3 impurity.
24 h	930°C	in H_2 gas	Black, not spinel.
32 h	850°C	in H_2 gas after sintered in coal gas and in H_2 at 800°C	Blue-black, poor conductor, spinel + impurities.
32 h	850°C	in H_2 gas after sintered in H_2 gas 800°C	Blue-black, poor conductor, spinel + impurities.
32 h	850°C	in H_2 gas	Blue-black, superconductor, pure spinel phase.
27 h	850°C	in H_2 gas	Blue-black, poor conductor, spinel + 5% impurity.

TABLE 3.1 Preparation conditions of spinel $LiTi_2O_4$ from Li_2CO_3 and TiO_2.

ground together for 20 - 30 minutes using a mortar and pestle and the ground powder transferred to a glass tube (1 in x 5 in) fitted with a polythene cap. The tube and its contents were then mechanically shaken for 3 hours and the powder reground for 20 - 30 minutes before being pelletised using a steel press with 15 mm diameter clean polished dies. An average pressure of 10 tons/sq. in. was used as standard throughout this work whilst average pellet weights were of the order of 2 gm. However, it was found that the pressed pellets were liable to crack whilst being transferred to the silica tube for sintering if care was not taken. The sintering process was carried out in the centre of the "hot zone" of the furnace, as shown in Plate 3.2, under a hydrogen atmosphere, the rate of hydrogen flow being kept constant throughout. The firing temperature was found to be very critical, as was the firing time. Specifically, it was found that the pure spinel of $LiTi_2O_4$ was obtained on firing at a temperature of 850°C for at least 32 hours. The sample was then blue-black in colour with high conductivity.

3.2 X-Ray Diffraction Analysis

The X-ray diffraction technique was used to identify spinel structure in the prepared samples and to assess their purity. The apparatus used was a Philips automatic powder diffractometer in conjunction with a stabilized X-Ray Generator and Copper K_α radiation (Plate 3.3). The system is equipped with a proportional counter and facilities for automatic continuous scanning across a range of angles in 2θ, where θ is the Bragg Angle, with output to a chart recorder.

The sample to be analysed was ground and sieved to a particle size diameter of less than 65 μm. This powder was pressed flat into the sample holder using a glass plate and mounted in the diffractometer. The counter was set near to $2\theta = 10^\circ$ and driven at a constant angular

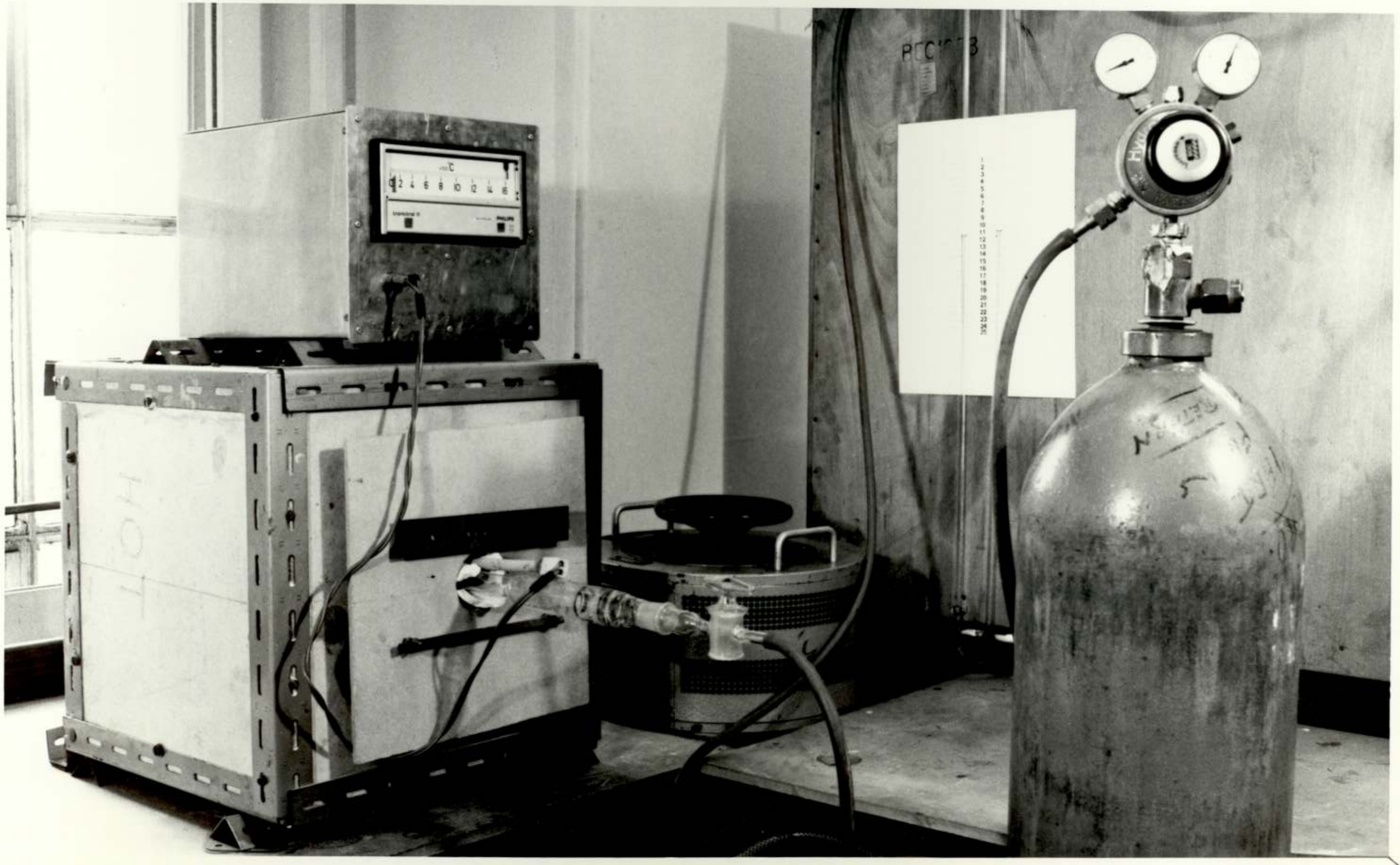

Plate 3·2 Apparatus for Sintering $LiTi_2O_4$

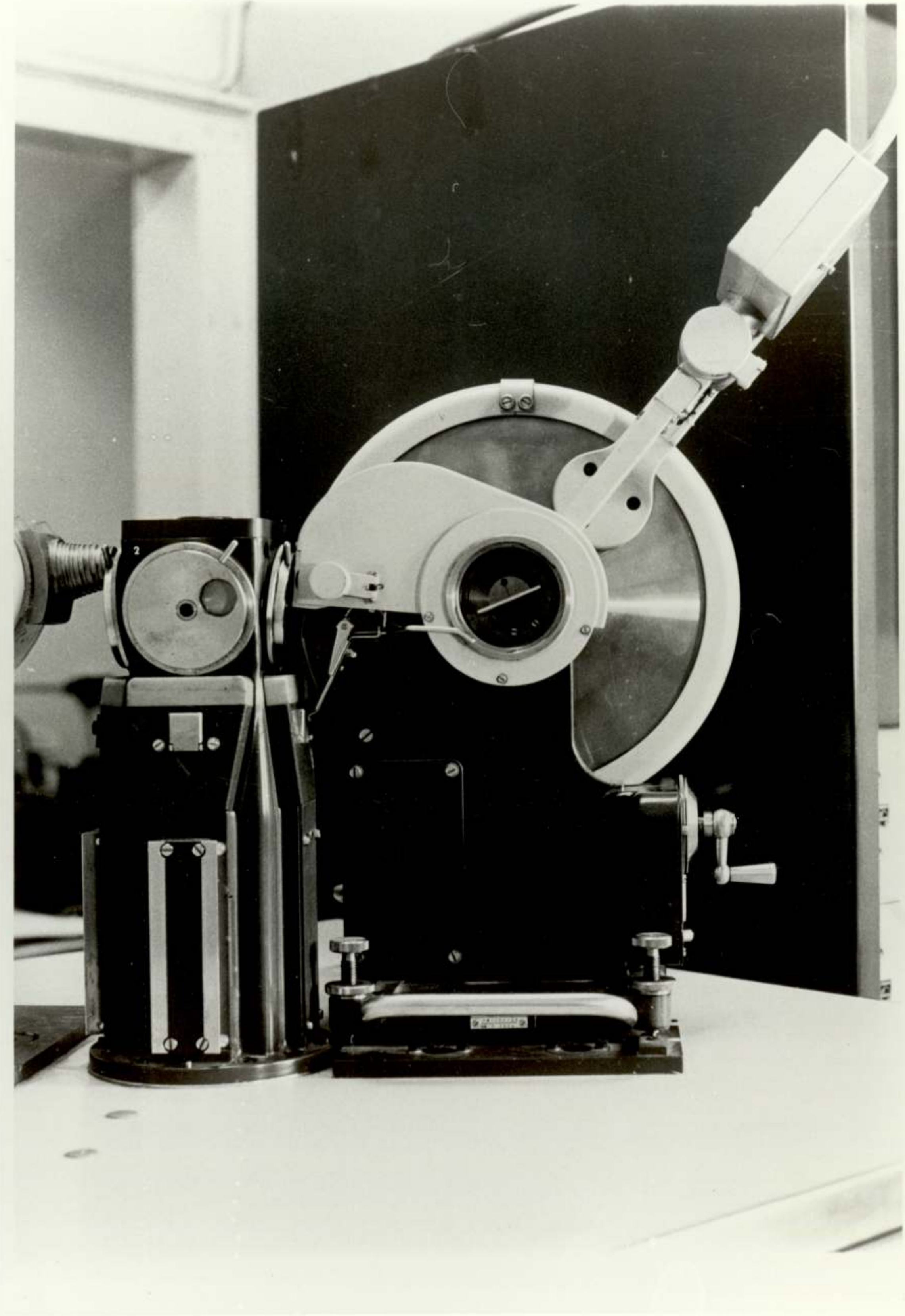

Plate 3.3 X-ray Diffractometer

velocity through increasing values of 2θ until the entire angular range had been 'scanned' and a chart recording obtained. Typical results obtained in this way are shown in Plates 3.4 and 3.5 and provide a record of counts per second (proportional to diffracted intensity) versus diffraction angle, 2θ. The scanning rate used was fixed at 1° change in 2θ /min for all samples.

3.2.1 Data Handling

The observed values of the Bragg angles (2θ), d-spacing, the intensities (I/I_{max}) and indices (h k l) of the lines are indicated in Tables 3.2 and 3.3 for $CuRh_2Se_4$ and $LiTi_2O_4$ respectively. The observed intensities are the peak heights of the diffraction lines as taken from the diffractometer trace. The indices (h k l) are either all odd or all even with the systematic extinction of o o l lines ($l \neq 4n$) and h k o lines (where $\frac{h+k}{2}$ is odd), this extinction being characteristic of the face-centred cubic space group Fd3m of which the spinel structure is an example.

Additionally, the lattice parameters (a_o) were determined by extrapolation to a Bragg angle, 2θ, of 180° using the extrapolation function $\frac{1}{2}(\cos^2\theta/\theta + \cos^2\theta/\sin\theta)$. The Cu K_α doublet was very well resolved at the higher Bragg angles for all samples studied.

3.2.2 Some Crystallographic Results

The X-ray diffraction patterns of the spinel samples, $LiTi_2O_4$ and $CuRh_2Se_4$, are shown in Plates 3.4 and 3.5 respectively. The $CuRh_2Se_4$ sample, sintered at 600°C for 48 hours shows no impurity lines in its diffraction pattern. However, in the case of $LiTi_2O_4$, there are slight traces of impurity lines (approximately 1%) appearing between the lines (111) and (311) in its diffraction pattern.

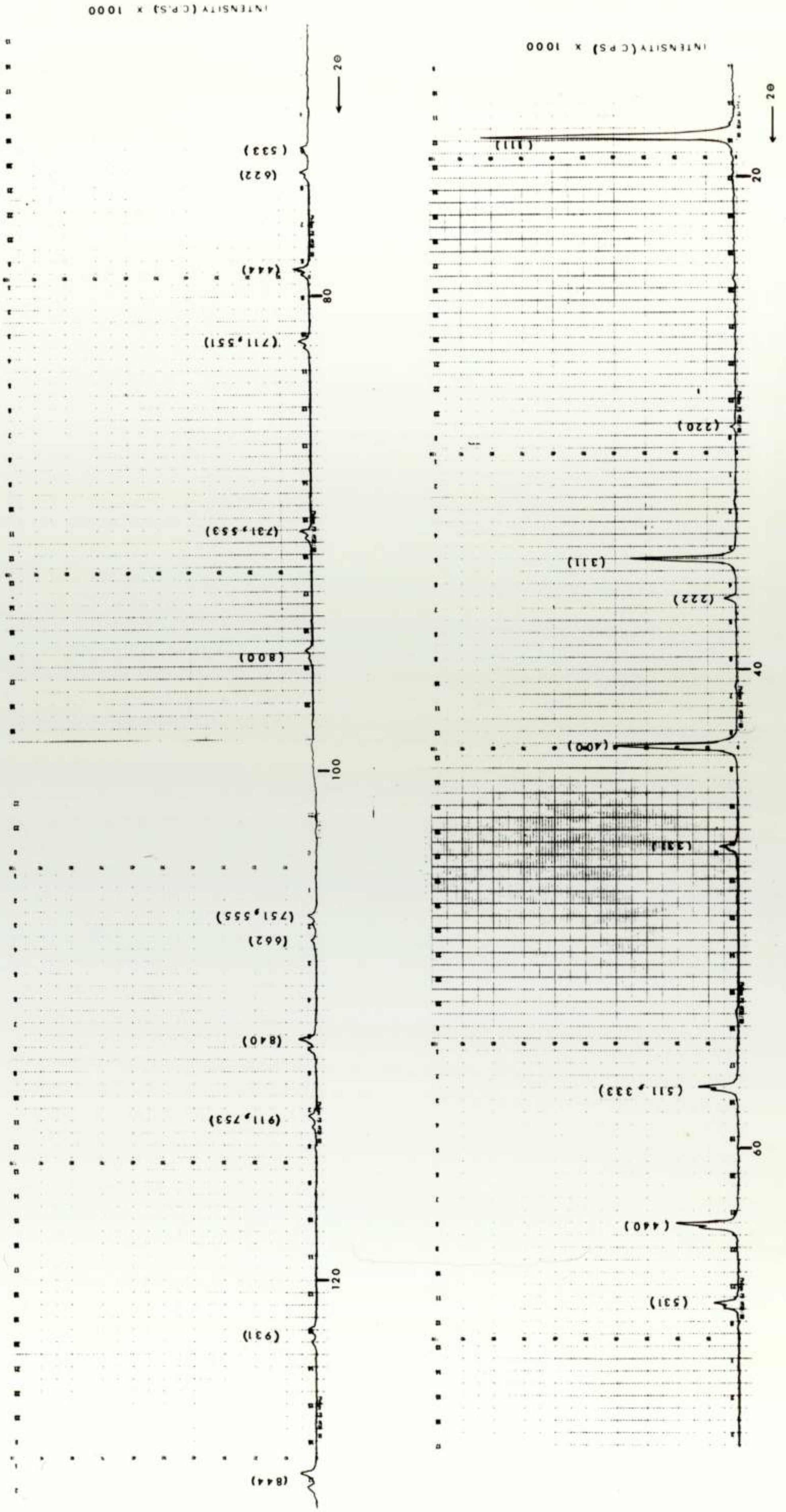

PLATE 3.4 X-RAY DIFFRACTION PATTERN OF SPINEL $LiTi_2O_4$

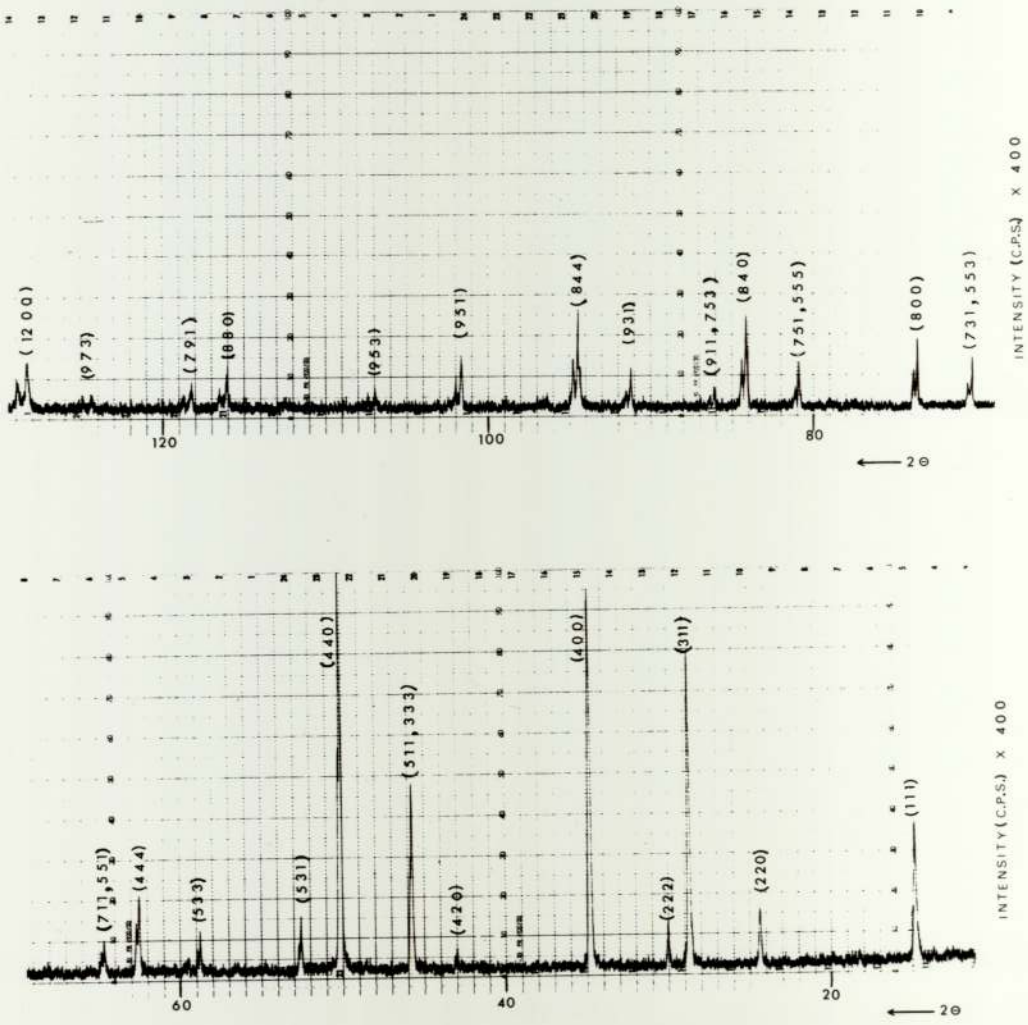

PLATE 3.5 X-RAY DIFFRACTION PATTERN OF SPINEL $CuRh_2Se_4$

TABLE 3.2

X-ray Data for $LiTi_2O_4$ with spinel structure

2θ (observed) $\pm 0.05^{\circ}$	d-spacing (observed)	Intensity (I/I_{max})	Indexing (h k l)
18.35	4.83	100	111
30.10	2.97	1	220
35.50	2.53	42	311
37.15	2.42	5	222
43.10	2.10	49	400
47.20	1.93	7	331
56.96	1.62	15	511,333
62.55	1.49	24	440
65.75	1.42	10	531
73.90	1.282	4	533
74.90	1.268	4	622
78.90	1.213	6.5	444
81.80	1.177	5	711,551
89.57	1.094	5	731,553
94.42	1.051	3	800
105.35	0.969	3.6	751,555
106.15	0.964	7	662
110.40	0.939	3.2	840
113.325	0.923	3.5	911,753
122.25	0.880	3.5	931
128.15	0.857	6.5	844
131.925	0.844	3.0	933

TABLE 3.3

X-ray Data for $CuRh_2Se_4$ with spinel structure

2θ (observed) ±0.05°	d-spacing (observed)	Intensity (I/I_{max})	Indexing (h k l)
14.80	5.99	36	111
24.40	3.65	16	220
28.70	3.11	78	311
30.00	2.98	12	222
34.80	2.58	94	400
43.00	2.10	6	420
45.70	1.99	47	511,333
50.15	1.82	100	440
52.60	1.74	15	531
58.80	1.57	11	533
62.60	1.48	20	444
64.78	1.44	9	711,551
70.30	1.34	13	731,553
73.78	1.284	18	800
81.00	1.186	12	751,555
84.20	1.150	24	840
86.25	1.128	6	911,753
91.40	1.068	11	931
94.65	1.049	26	844
101.83	0.993	14	951
107.22	0.958	6	953
116.28	0.908	12	880
118.45	0.897	8	791
124.70	0.870	5	973
128.65	0.855	12.5	1200

As regards the lattice parameters, a_o, of these two spinels, values of a_o of $\simeq$ 8.403 ± 0.001 Å and 10.261 ± 0.001 Å for $LiTi_2O_4$ and $CuRh_2Se_4$ respectively were obtained (see Figures 3.2 and 3.3).

3.3 Apparatus for Heat Capacity Measurements over the Temperature Range 1.5 - 300°K

Since heat capacity measurements had not previously been carried out in this laboratory, the apparatus used for this purpose had to be designed and tested before experiments could begin. Several factors were considered to be important at this stage. In particular, it was desirable that (i) the apparatus should be suitable for work with small samples, e.g., of the order of 10 gm or less because of the cost of producing $CuRh_2Se_4$, i.e., the high cost of rhodium, (ii) the size of thermometer used, together with its heat capacity at low temperatures, should be very small and of reasonable accuracy, i.e. ~ 1% at low temperatures, (iii) exchange gas should not be used because of the adsorption which might occur at the surface of powdered samples, and, finally (iv) it should be possible to achieve rapid thermal equilibrium.

One additional factor should also be mentioned. Because it is difficult to achieve accuracy and sufficient sensitivity in a thermometer which could cover a wide temperature range, the heat capacity measurements to be described were carried out in two stages covering different temperature ranges. These ranges were taken as 1.5°K up to around 30°K and 30°K up to room temperature.

3.3.1 Heat Capacity Apparatus for 1.5 - 30°K

Traditional approaches to the measurement of heat capacity have been focussed on the design of adiabatic calorimeters (Giauque,

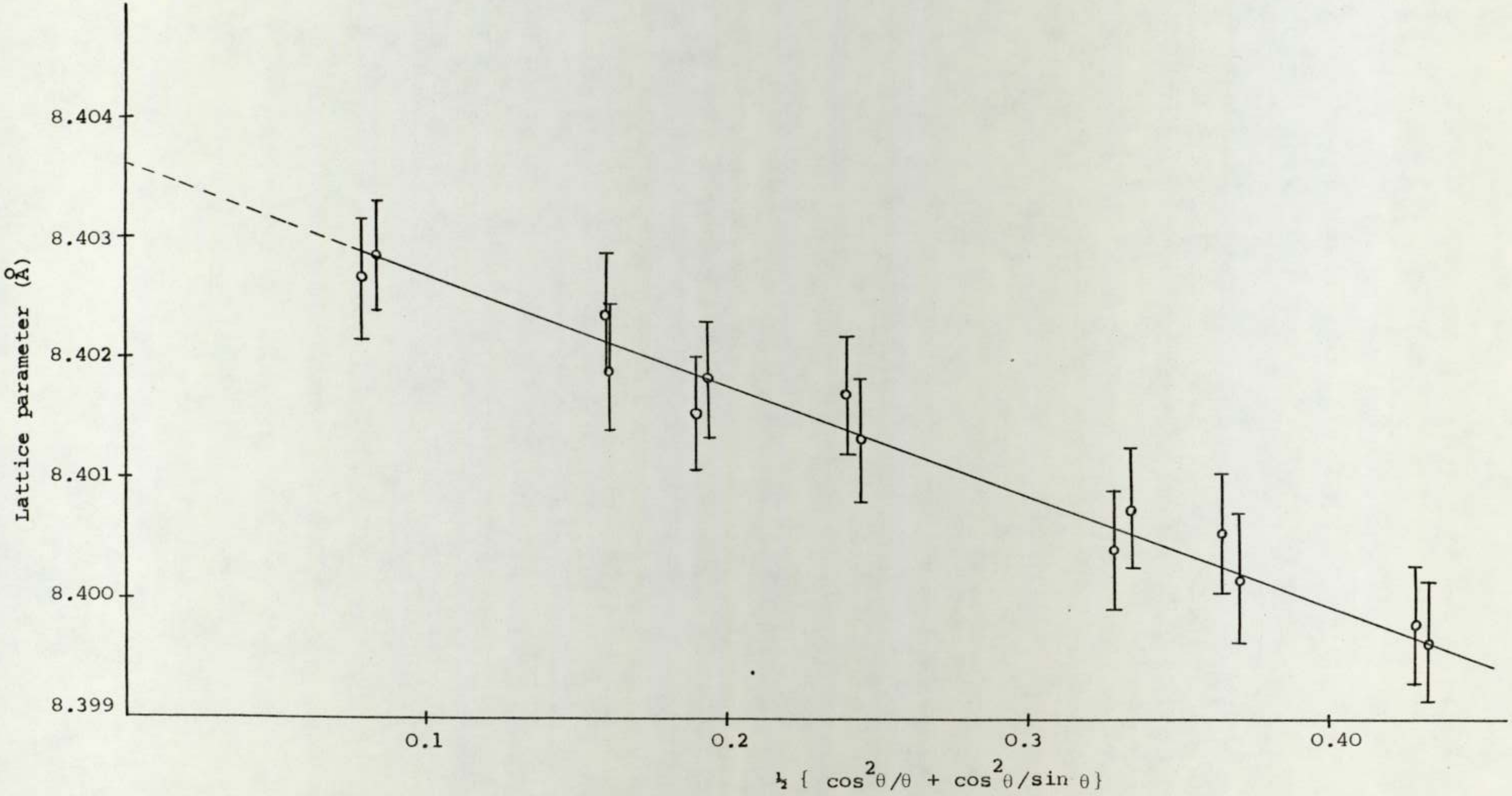

FIGURE 3.2 Extrapolation curve for the determination of the lattice parameter of $LiTi_2O_4$.

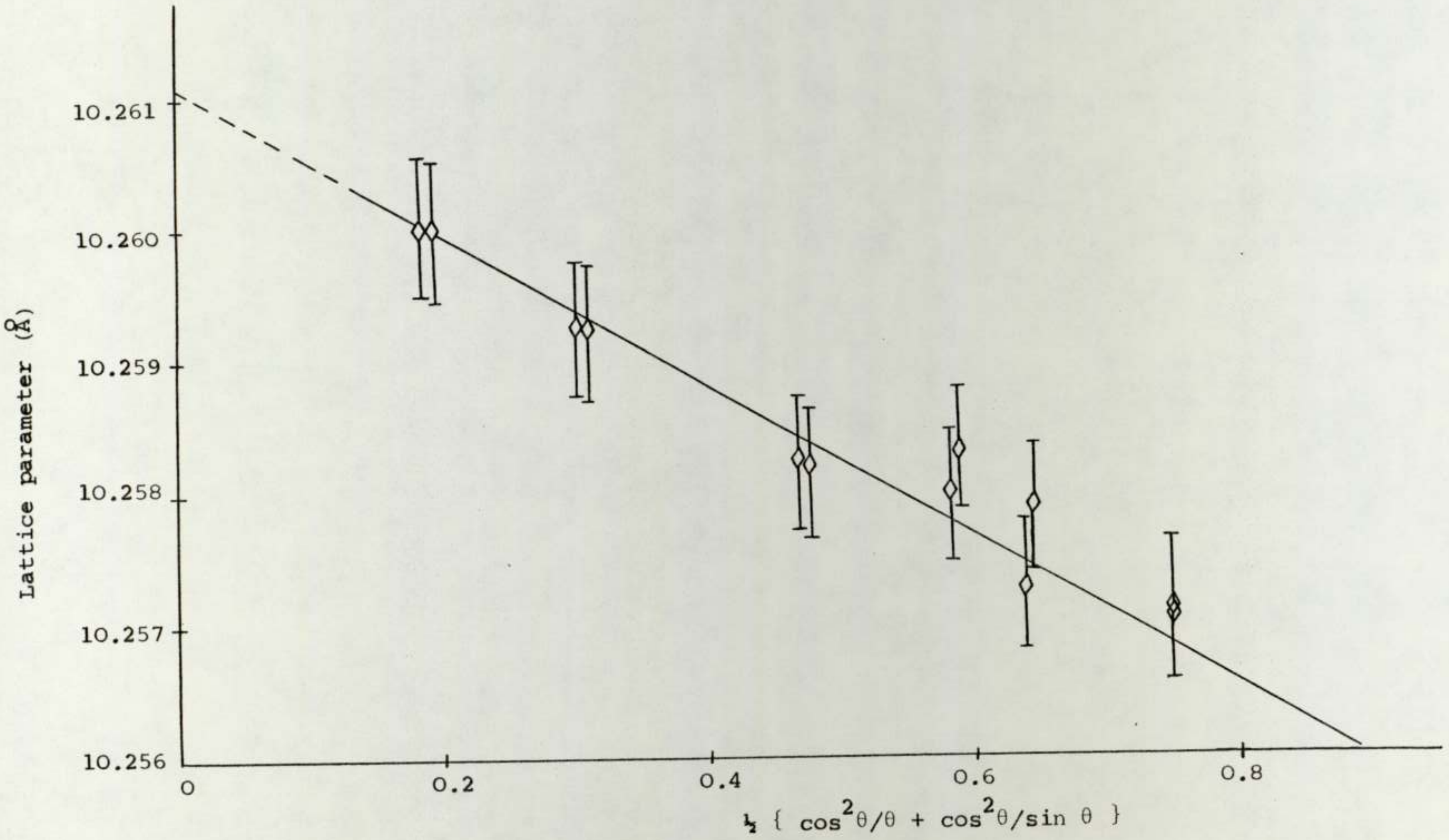

FIGURE 3.3 Extrapolation curve for the determination of the lattice parameter of $CuRh_2Se_4$.

1969). In such calorimeters, a variety of methods have been used to isolate the sample from its surroundings. However, in 1972, Bachmann, DiSalvo, Geballe, Greene, Howard, King, Kirsch, Lee, Schwall, Thomas and Zubeck introduced a new calorimeter for measuring the heat capacity of samples as small as 1 mg over the temperature range 1 - 35°K, using a silicon wafer as sample holder, temperature sensor and sample heater. In addition, the method of measurement used by these authors depends on the principle of thermal relaxation, i.e., upon measuring the thermal relaxation time constant, $\tau_1 = C/k$, where k is the thermal conductance linking the sample to the heat reservoir and C is the heat capacity of the sample. It was decided to adopt this latter technique in the present work, because such an apparatus is capable of measuring very small-sized samples (1 - 500 mg) and the relaxation time, τ_1, can be obtained by choosing a suitable value of k.

The apparatus used for obtaining heat capacity measurements in this way over the temperature range 1.5 - 30°K was therefore constructed as follows.

3.3.1 (a) The Thermometer

The silicon thermometer used in the present work was a semi-conducting resistance thermometer similar in character to the widely used germanium thermometer, the principal difference between the two being that electrical conduction in the silicon device takes place in a thin diffused surface layer rather than in the bulk of the semiconductor. In general, a silicon resistance thermometer can be constructed from a silicon wafer of n- or p-type whose doping is low enough for the material to be non-degenerate, i.e., its resistivity becomes extremely large at low temperatures. In the present work, the starting material consisted of thin slices of phosphorous-doped n-type silicon of about 0.25 - 0.5 mm thickness and impurity concentration $\leqslant 1 \times 10^{18}$ cm^{-3}, and was supplied by R.R.E. Malvern. Surfaces with suitable temperature dependent resistivities were prepared by using a combination of diffusion and etching procedures as will now be described.

3.3.1 (a) (i) Cleaning Procedure

If impurities such as finger grease were not initially removed from the silicon, they tended later to become irremovably infused into the slice after high temperature diffusion had occurred, thus affecting the performance of the thermometer. The utmost cleanliness was therefore observed in order to prevent contamination of the surface of the silicon slices.

The slices were first boiled in trichloroethylene in order to remove hydrocarbons, then boiled in concentrated nitric acid in order to remove the trichloroethylene. This latter process, however, also oxidises a thin surface layer of the silicon and this was removed in turn by dipping the slices into dilute hydrofluoric acid. This cleaning process had to be carried out prior to each diffusion since the silicon surface was easily contaminated and oxidised in air at room temperature.

3.3.1 (a) (ii) Masking Procedure

Silicon dioxide films have been used for selective masking against vapours during diffusion in silicon for semiconductor-device fabrication (Frosch and Derick, 1957). This SiO_2 surface film must be sufficiently thick and continuous in order to provide complete coverage of the silicon surface to be protected.

Masking is produced most effectively by heating the silicon slice in an oxidising atmosphere at high temperatures and then removing the oxide layer from one surface with hydrofluoric acid. This provides both oxidised and unoxidised surfaces on the same sample. In this study, the pre-oxidation step was carried out by heating the cleaned silicon slices, in the diffusion apparatus, at 1150°C for 3 hours (nitrogen, bubbled through the water, initially used as the carrier gas, tended to produce a rough surface on the sample, as observed under the microscope, after removing the silicon dioxide film with hydrofluoric acid; a sample heated in oxygen, on the other hand, exhibited a smooth surface). The oxide layer on one side of the silicon slice was divided into two parts, one of which was preserved by covering with wax whilst the other was removed by immersion in concentrated hydrofluoric acid. Finally, the wax coating was washed away with acetone and the clean surface rinsed with deionised water. The silicon slices were then ready for the diffusion operation.

3.3.1 (a) (iii) Diffusion Technique

The furnace and associated equipment used for the diffusion of phosphorous is shown in Plate 3.6 and illustrated schematically in Figure 3.4. The essential components consist of an elongated ceramic tube, approximately 46 mm in inside diameter and one metre long, extending through two temperature controlled furnace zones. The first zone, A, provides a lower temperature, 300°C, for controlling the vapour content of phosphorous pentoxide (P_2O_5) impurity in the carrier gas, N_2, whilst the second zone, B, provides a higher temperature, around 1150°C, in which the silicon samples are placed. A rising temperature gradient between the two zones avoids the re-deposition of P_2O_5 vapour impurity before the carrier gas reaches the silicon samples. The zone temperatures, measured with Chromel-Alumel thermocouples, were regulated to $\pm 5^\circ C$, whilst a manometer on the outlet to the furnace was used to maintain the

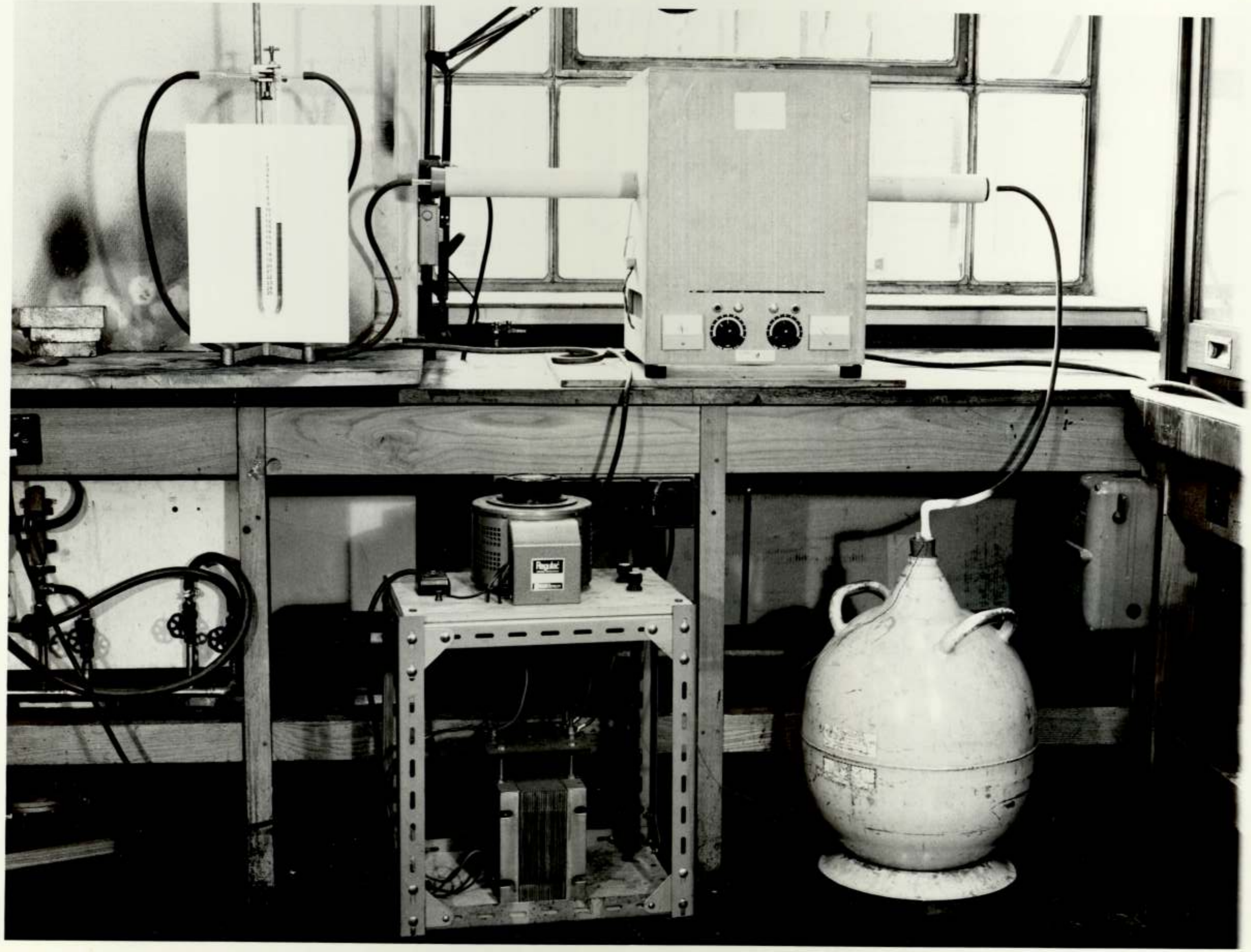

Plate 3.6 Apparatus for Diffusion

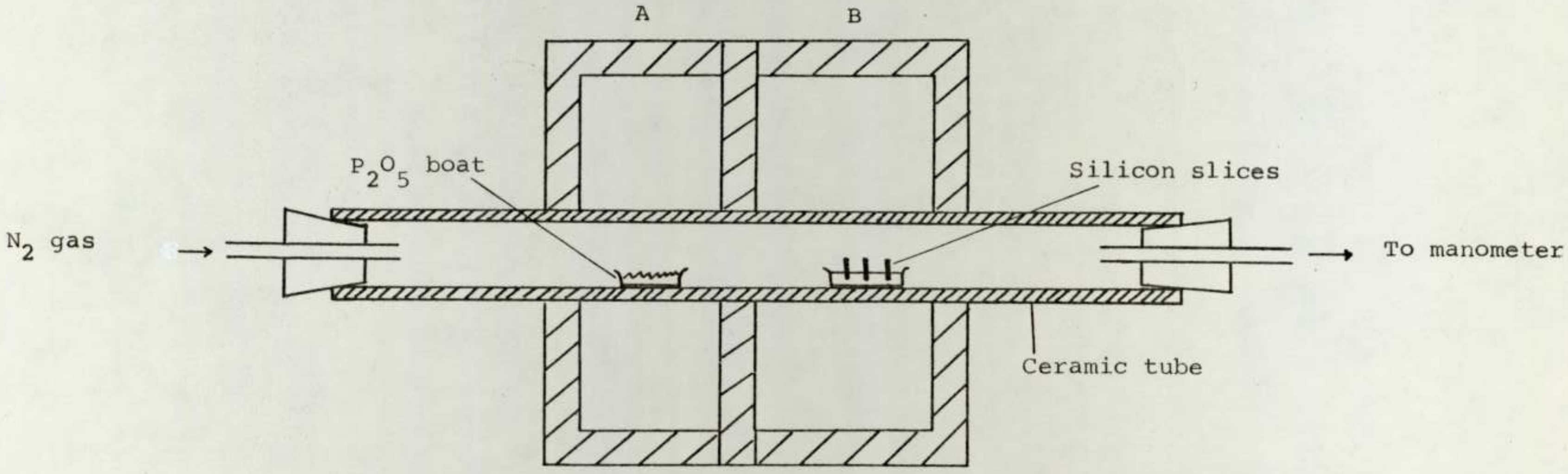

FIGURE 3.4 Schematic diagram illustrating the diffusion process inside the ceramic tube

flow-rate of the N_2 carrier gas at a constant 1000 cc/min during each diffusion run. The effluent carrier gas, which still contained harmful residual phosphorous containing vapour, was carried away via the rubber tube leading from the end of the manometer to a fume cupboard.

So as to ensure uniform contact of the phosphorous vapour in the carrier gas stream with the silicon surfaces, the silicon samples were held vertically in a slotted silica holder as shown in Plate 3.7(b). Additionally, before the silicon samples were inserted for diffusion or oxidation, the carrier gas flow was allowed to continue for several minutes in order to establish a steady-state condition.

For all samples, the P_2O_5 impurity was controlled at 300°C and the diffusion process maintained for a minimum of at least 60 hours. According to Figure 3.5, these conditions resulted in a diffused layer of about 20 μm thickness.

3.3.1 (a) (iv) Etching Process

After the diffusion of phosphorous into the surface layer, the silicon slice was cut into rectangular shaped pieces of approximately 10 x 12 mm in size. The areas which were to serve as contact pads in the thermometer were coated with wax (see Figure 3.6) and the remaining degenerate layer etched off by means of two etching solutions - a fast etch consisting of 1:9 (48%) hydrofluoric acid : (70%) nitric acid, and a slow silver-glycol etch consisting of 400 ml (70%) nitric acid, 10 ml silver nitrate solution (1 gm $AgNO_3$/100 ml of water), 200 ml distilled water, 200 ml of propylene glycol and 10 of hydrofluoric acid.

Each silicon slice was fast-etched using the HF/HNO_3 reagent until its resistance started to change. At this point, the contact pads and active region were coated with wax, whilst the degenerate layer on the sides of the silicon piece was etched off using the fast-etch

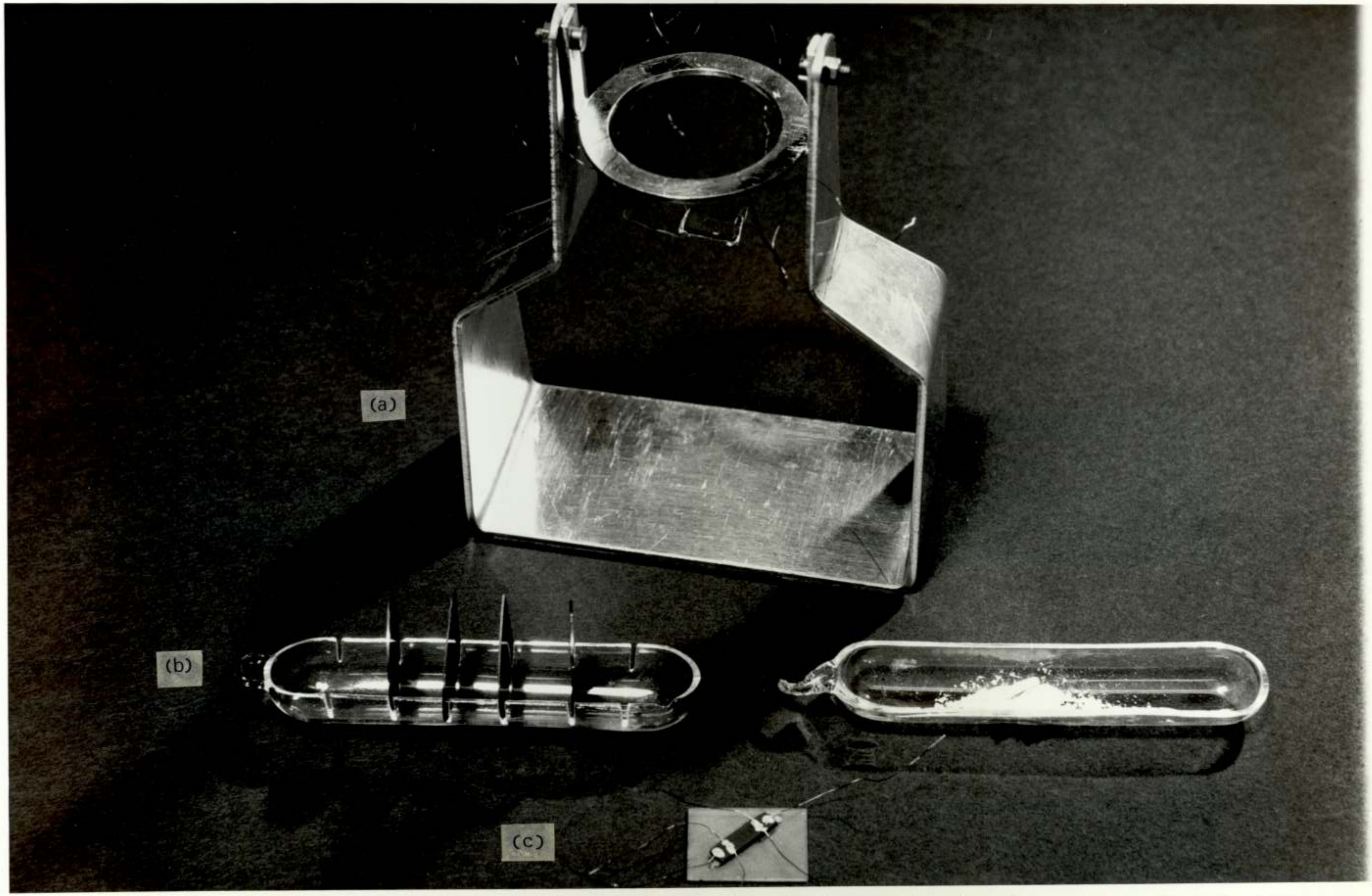

Plate 3.7 (a) Demountable holder for silicon calorimeter (b) Slotted silica holder for silicon slices and P_2O_5 boat.
(c) Resistivity sample

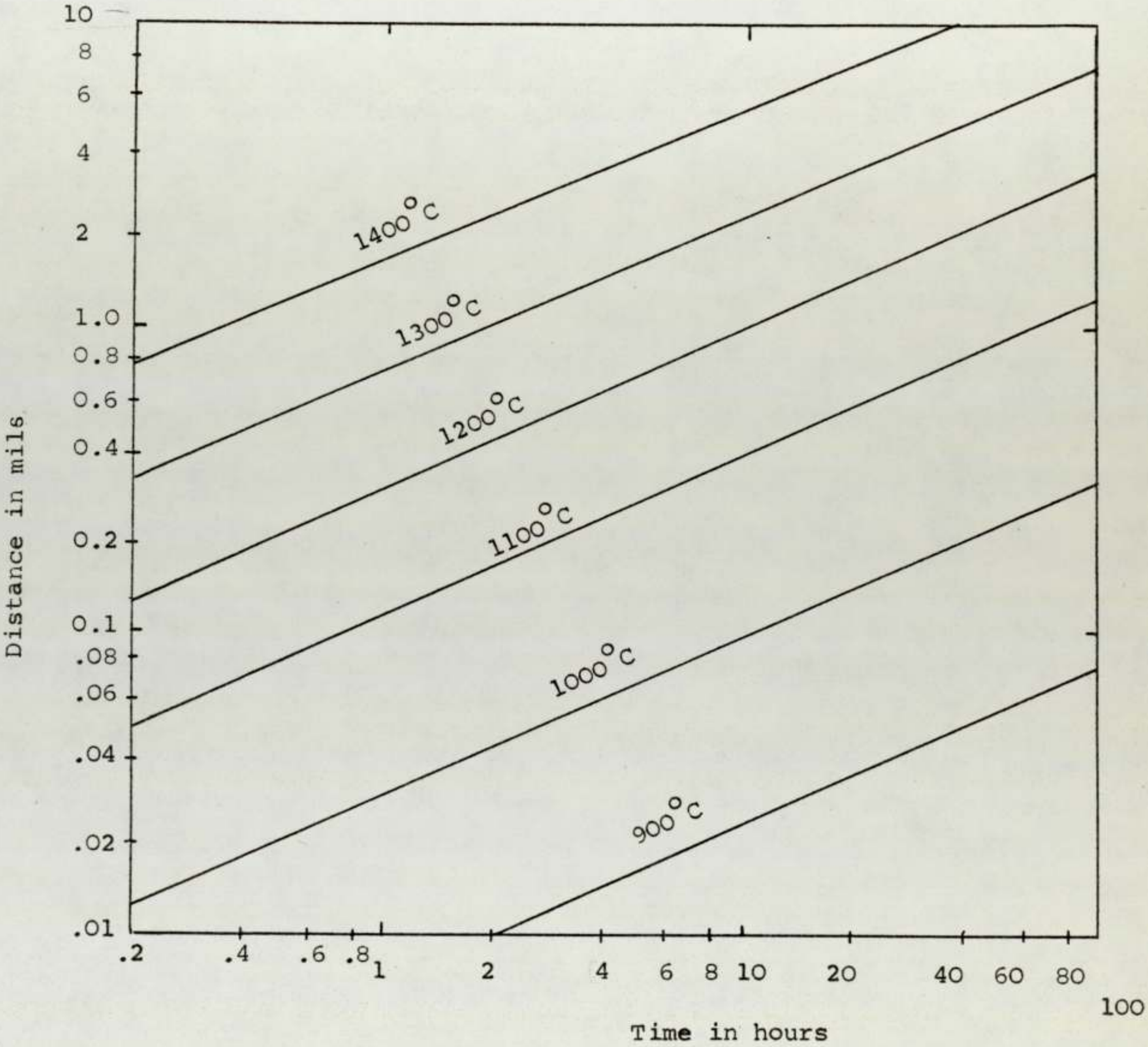

FIGURE 3.5 p-n junction depth as a function of time for the diffusion of boron and phosphorus into silicon containing 10^{16} impurity atoms per cm^3 (Frosch, 1958).

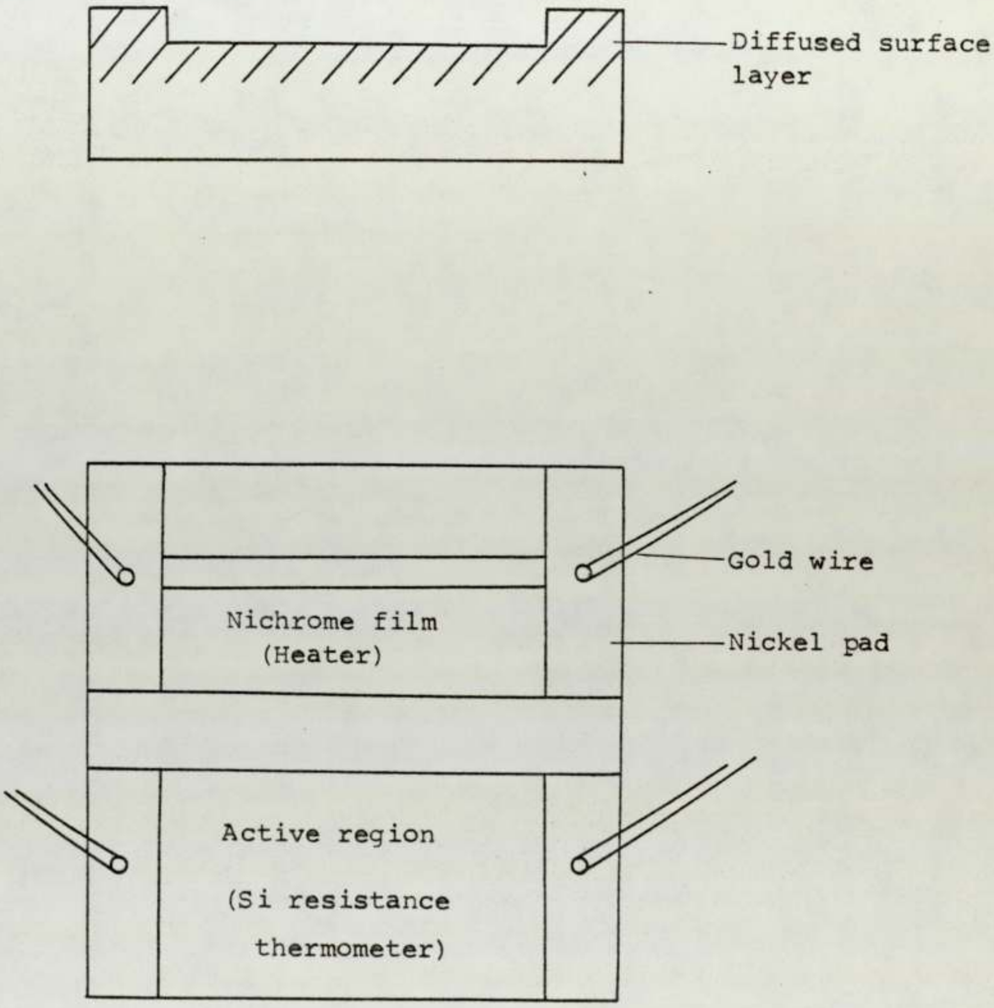

FIGURE 3.6 Diagram of a silicon calorimeter configuration.

solution so as to prevent the possibility of shorting out in the active region. Finally, the active region itself was etched in short steps using the slow silver-glycol etch until the desired resistance/temperature characteristics were obtained. Figure 3.7 shows the resistance versus temperature characteristics of a typical silicon resistance thermometer after each of five successive etching steps.

3.3.1 (a) (v) The Electrical Contacts to Silicon

The making of permanent electrical contacts to the silicon device was more difficult than might have been imagined and various methods were tried. For example, thin metal films were evaporated on to the degenerate contact pads and then gold wires, each pre-melted in a hydrogen flame to form a ball at the end, pressure bonded to these films using a glass capillary to position the wires and to apply pressure. However, it was found that the contacts made by this method had insufficient adherence to support the weight of the sample.

An alternative method which was found to be satisfactory was electrodless nickel plating which provides uniform plating over all surfaces contacted by the plating solution. A typical bath used for nickel plating on silicon was made up as follows:

	gm/litre
nickel chloride	25
sodium hypophosphite	12.5
tri-ammonium citrate	50
ammonium chloride	37.5

This solution is filtered and ammonium hydroxide added until the colour of the solution turns from green to blue. When in use, the plating bath was maintained at a temperature of 85 - 95°C, with more ammonium

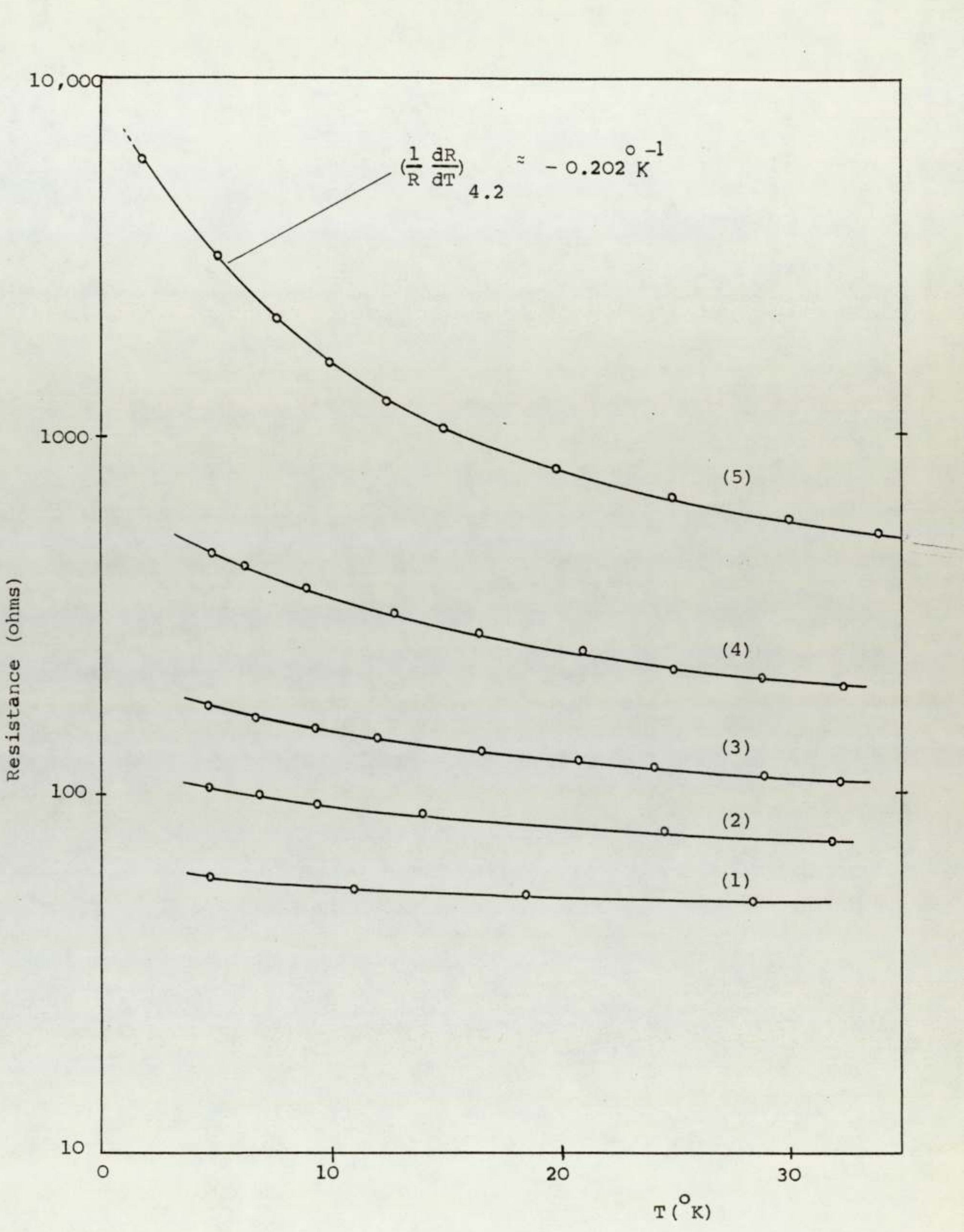

FIGURE 3.7 The resistance versus temperature for a diffused silicon resistor after a series of etching processes (1) to (5).

hydroxide being added as necessary to preserve the blue colour.

This nickel plating technique was found to be very useful since the gold wires to be connected to the thermometer could be attached to the plated surface using ordinary soft solder at temperatures below 200°C. The adherence of these contacts was found to be extremely good with very low contact resistances being observed in most cases.

3.3.1 (a) (vi) Calibration of Silicon Resistance Thermometers

The silicon resistance thermometers which were to be used in the heat capacity measurements were calibrated against standard germanium and rhodium-iron thermometers (both purchased from Cryogenic Calibrations Limited) over the temperature range 1.5 to 40°K.

Calibration between 1.5 and 4.2°K was carried out by introducing helium exchange gas into the enclosure surrounding the sample holder cryostat and then pumping over the helium bath by means of a rotary pump. The pumping speed was controlled manually and a steady temperature maintained for about 20 minutes at intervals of approximately 0.5°K. The vapour pressure of liquid helium was measured by means of the absolute pressure gauge connected to the helium bath. For temperatures above 4.2°K, however, the enclosure surrounding the sample holder cryostat was evacuated, initially, by the rotary pump and, finally, by the diffusion pump which was then used continuously throughout the duration of the heat capacity measurements.

In order to provide working temperature scales, the calibrated points were fitted to a smooth curve of the form:

$$\ln R = \sum_{n=0}^{N} An\, (\ln T)^n \qquad \text{...... (3.3)}$$

It was found that a good fit was obtained by dividing the data into four temperature ranges, namely 1.5 - 4.5°K, 4.2 - 10°K, 9 - 20°K and 18 - 40°K. A typical calibration is shown graphically in Figure 3.7. It was found that an active region sheet resistance of 3×10^3 ohms or more at liquid helium temperatures gave a sensitivity, $\frac{1}{R}\frac{dR}{dT}$, of $-0.2^\circ K^{-1}$ at 4.2°K.

3.3.1 (b) Heater

In initial attempts to make a heater, a thin layer of chromium + 5% titanium metal film was evaporated on to the non-degenerate region of the silicon slice (Figure 3.6) between the nickel-plated pads. Typical widths of 100 μm and thicknesses in the region of 500 Å, as determined by interferometry, with resistances of 1000 - 2000 ohms were used. However, it was observed that after temperature cycling a few times between liquid helium and room temperatures, films prepared in this way tend to peel off.

Because of these difficulties and the very high melting point of chromium and its tendency to react with the tungsten source during the evaporation process, it was eventually decided that a nichrome film instead of chromium would be used. It was found that the resistance of this nichrome film was of the order of 1000 ohms for a layer of the same dimensions. Furthermore, the nichrome heater also showed only a very slight variation in resistance with temperature, less than 10 ohms over the temperature range 4.2 - 30°K.

3.3.1 (c) Cryostat Construction

A general view of the cryostat and its associated equipment is shown in Plates 3.8 and 3.9 whilst Figure 3.8 shows a schematic diagram of the cryostat assembly ready for use at liquid helium temperatures. The liquid helium cryostat used in the low temperature

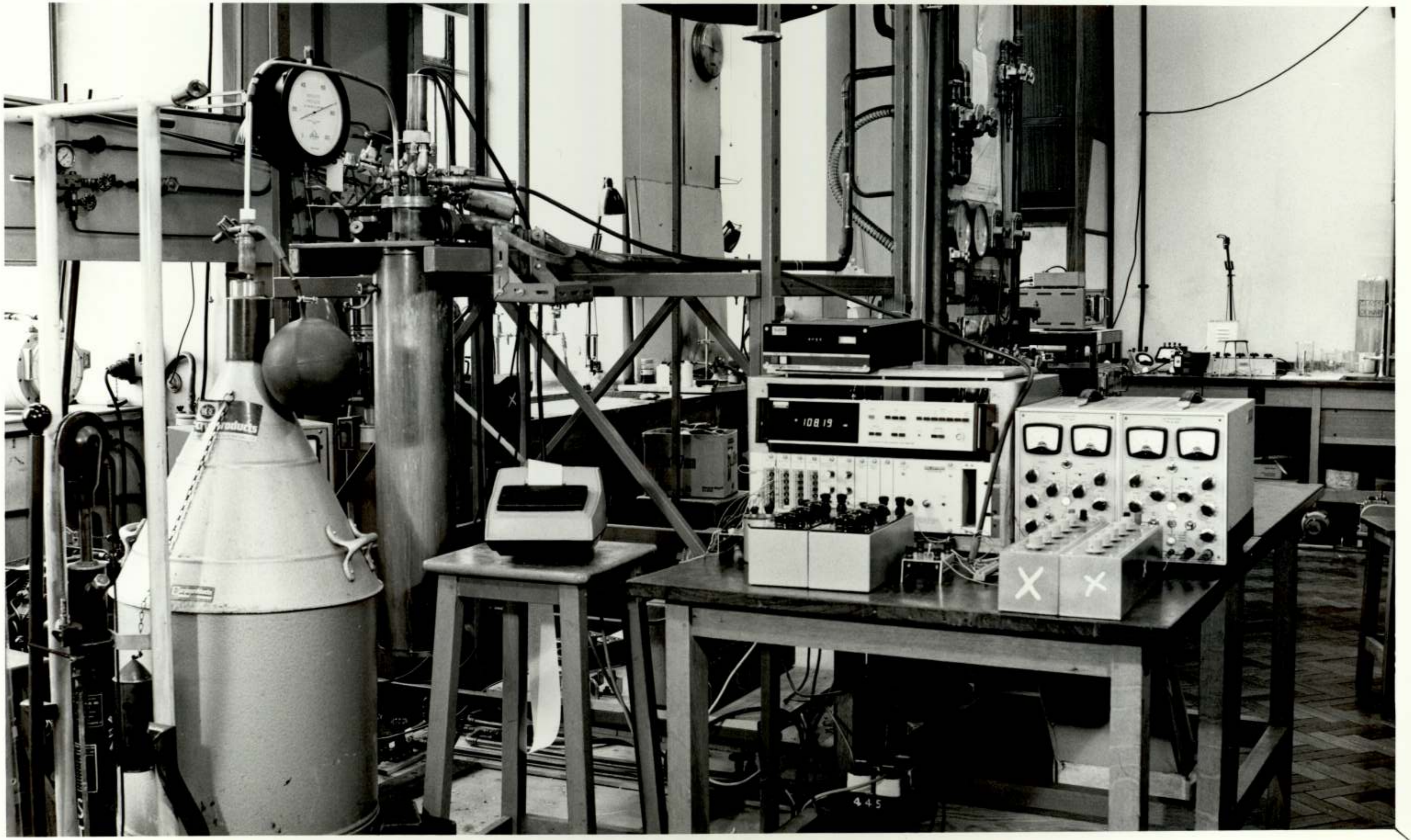

Plate 3.8 General View of Low Temperature Equipment

Plate 3·9 Low Temperature Cryostat

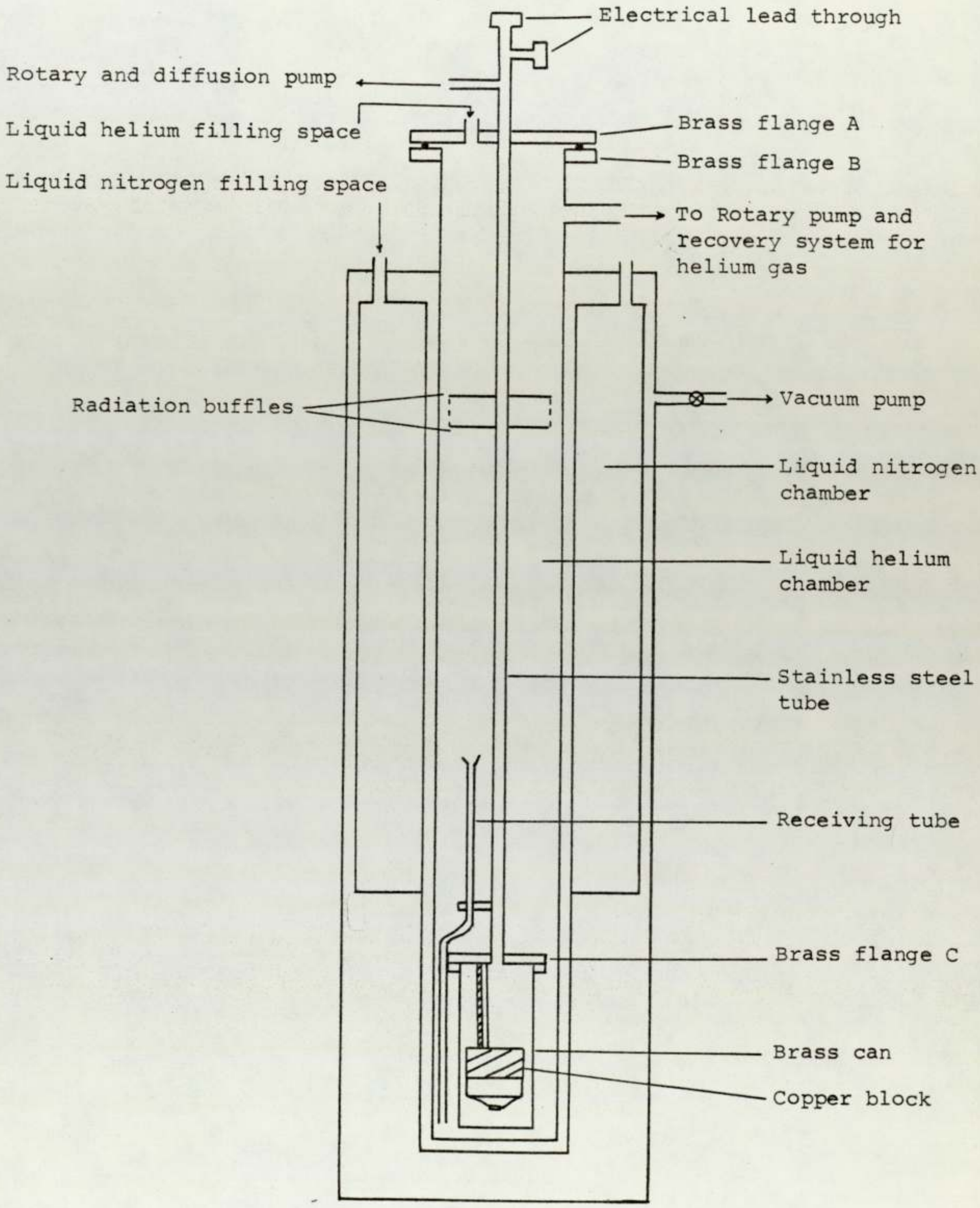

FIGURE 3.8 Schematic diagram of low temperature cryostat

experiments was a standard metal helium cryostat, manufactured by the Oxford Instrument Co., comprising two refrigerant compartments - an outer one for liquid nitrogen, having a volume of 5.5 litres, and an inner one for liquid helium, of about 3.5 litres capacity. The helium cryostat was suspended in a framework and, as the heat leak into the helium reservoir was less than 0.1 watt, the experimental enclosure could be maintained at near liquid helium temperatures for 10 to 15 hours. In addition, a copper pipe was linked to the helium chamber which could be used, firstly, for collecting helium gas in a recovery bag, and, secondly, for lowering the temperature inside the chamber by reducing the pressure over the liquid helium by means of a 250 litre/sec rotary pump. In this way, it was possible to cool the liquid helium to a temperature of about 1.5°K as and when required.

The innermost part of the cryostat assembly consisted of a brass can, 12 cm long, 5 cm in inside diameter and of 0.5 cm wall thickness. A stainless steel tube, approximately 2 cm in diameter, 77 cm long, extending down the centre of the cryostat from the brass flange A, was silver-soldered on to the male section of the brass flange C and the top end of the tube was branched for evacuation and the introduction of electrical leads. In order to reduce the rate of evaporation of liquid helium from its metal dewar, radiation shields in the form of two horizontal copper baffles were soldered on to the tube with polystyrene foam, about 4 cm in thickness, placed between the baffles.

Figure 3.9 shows details of the assembly inside the brass vacuum can of the cryostat. The copper block, made from OFHC grade copper, was supported by a 5 cm long stainless steel rod, 2 mm in diameter, suspended from the brass flange C, whilst the thermal link between the copper block and the flange C was provided by 26 swg copper wire. The copper block was also equipped with a standard germanium

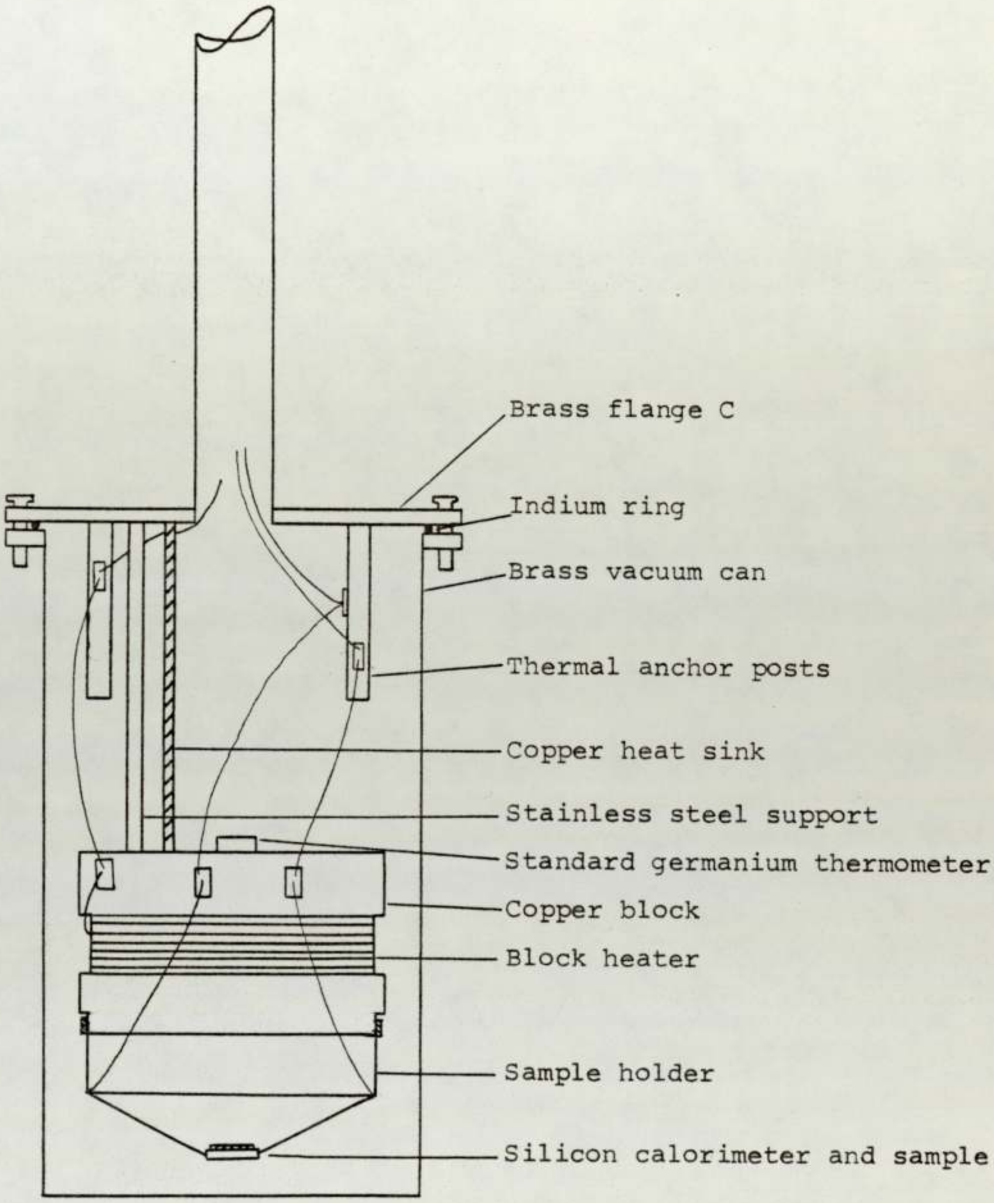

FIGURE 3.9 Assembly inside the brass vacuum can

thermometer (Cryogenic Calibrations Limited) so that the silicon thermometer could be re-calibrated for each run.

In order to obtain good thermal linking between the copper block and copper sample holder, the sample holder was gold-plated and the indium-covered press contacts on this gold-plated copper sample holder screwed on to the copper block by means of two 8 BA bolts. The block temperature was varied using the heater windings, wound around the copper core with 40 swg copper constantan wire of 480 ohms resistance. To ensure good thermal contact between each winding, a thin layer of GE 7031 low temperature varnish was painted on to each successive layer of wire during the process of winding the heater coil. Four pure gold wires of 0.076 mm diameter were used to suspend the silicon calorimeter from the gold-plated sample holder (see Plate 3.7(a)).

In order to prevent heat transfer along the wires at room temperature, thus raising the block temperature above that of the bath, electrical wires introduced into the cryostat were thermally anchored to the copper posts screwed on to the inside of the brass flange C. Pieces of gold-plated copper foil, approximately 3mm x 4mm in size, were glued to the copper thermal anchor posts by means of a thin layer of araldite (which also served as the electrical insulation) and the electrical wires soldered on to these foils. To ensure that the temperature gradient effect along the wires was at a minimum, additional thermal anchoring was made on the copper block. The potential and current wires were 40 and 38 swg enamelled copper wires respectively, connected to the external electric circuits by means of ten gold-plated brass pins forming the plug which was set in a ceramic seal mounted in a brass bush.

The entire cryogenic assembly was enclosed in a brass can fitted with a bolted brass flange C with an intermediate indium ring acting as a vacuum seal. The apparatus was evacuated using a diffusion pump backed by a rotary pump. A pressure of about 10^{-6} torr could be obtained within about 4 - 5 hours of pumping.

The small stainless steel tube attached to the flange C was used to carry the liquid helium from the transfer syphon through to the bottom of the cryostat. To prevent wastage of liquid helium, syphoning needed to be carried out slowly, especially prior to its collection in the receiving tube. As a further measure to minimize loss, a small amount of liquid helium was allowed to collect in the bottom of the cryostat and the cold gas allowed to cool the brass can and its contents before the can became completely immersed in liquid helium.

3.3.2 Heat Capacity Apparatus for 30 - 300°K

The cryostat described previously in Section 3.3.1 (c) could not be used for measuring heat capacity at temperatures above 30°K because of the characteristics of the silicon thermometers. For higher temperature measurements, therefore, another cryostat was constructed based on the conventional method of heat capacity measurement, i.e., an adiabatic calorimeter with a radiation shield to isolate the sample from its surroundings. A differential thermocouple in conjunction with a temperature controller was used to minimize any temperature difference between the radiation shield and the calorimeter, as described by Kirkham and Yates (1968). The other components of the apparatus used for heat capacity measurement over this 30 - 300°K temperature range were similar to those described in the previous Section 3.3.1 (c), except for the cryogenic components inside the brass vacuum can, as shown in Plate 3.10 and illustrated schematically in Figure 3.10. The contents of this compartment and their construction will now be described in detail.

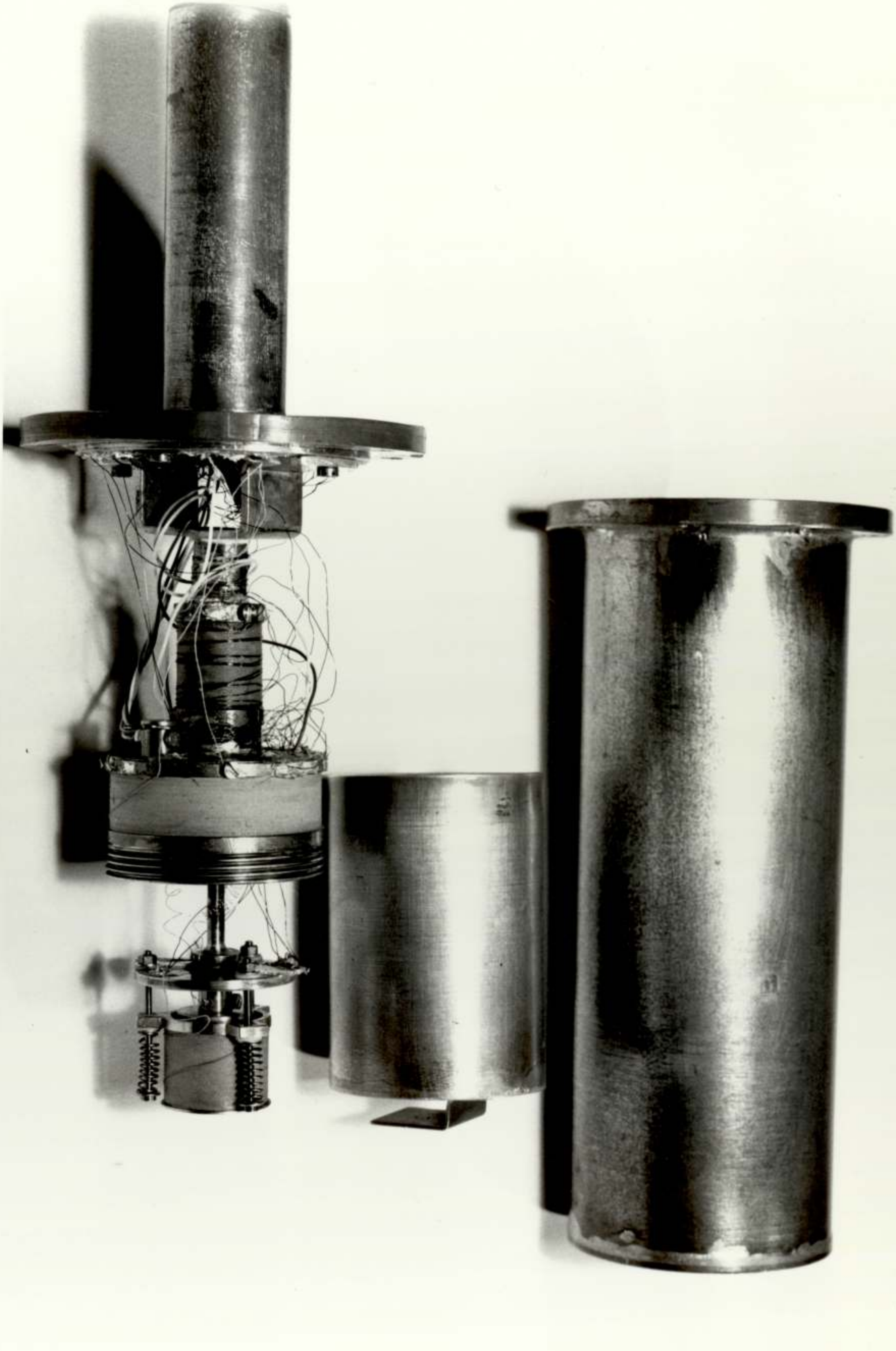

Plate 3·10 The Cryogenic Components Inside the Brass Can

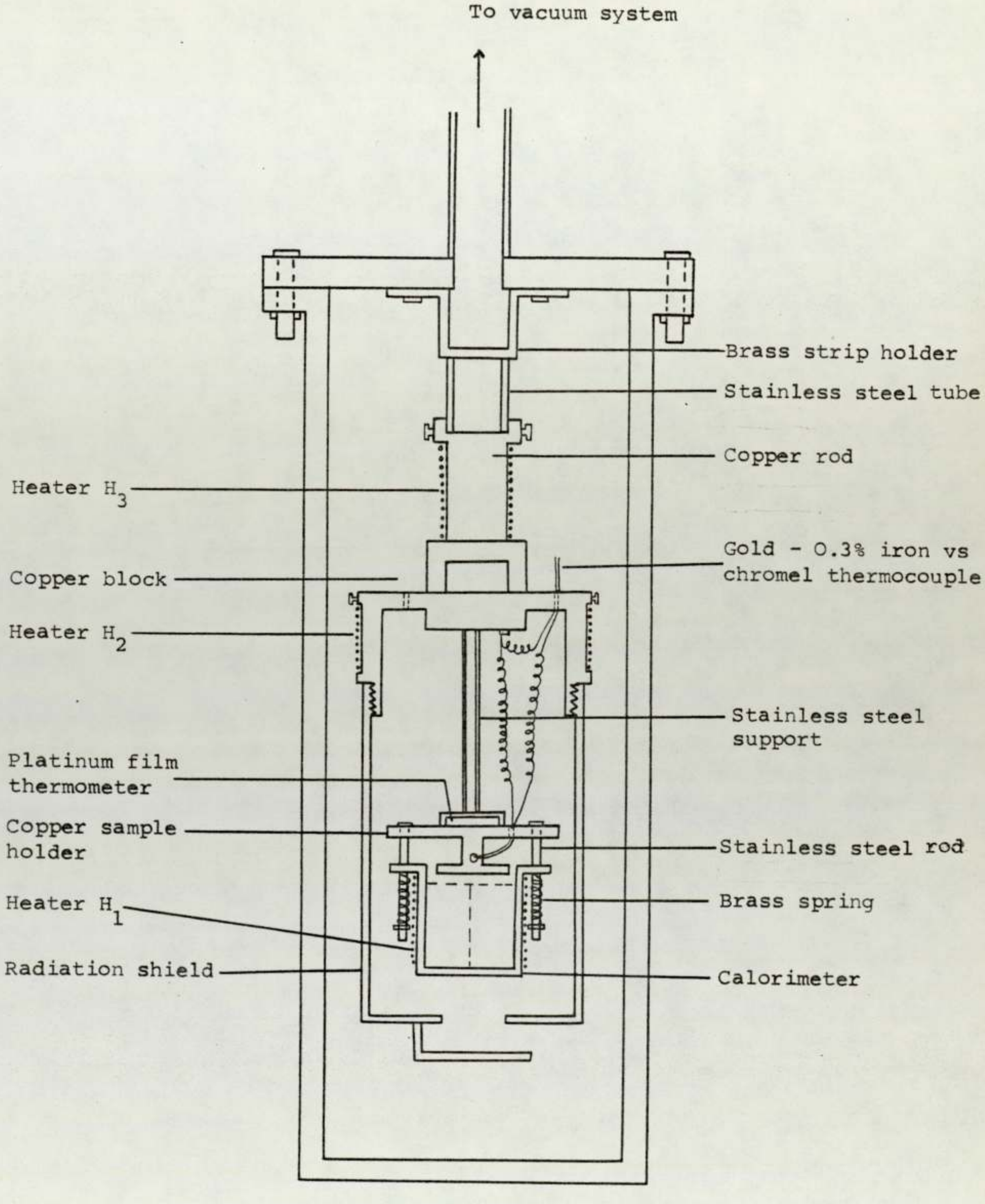

FIGURE 3.10 Schematic diagram of cryostat for heat capacity measurement over the temperature range 30 - 300°K.

3.3.2 (a) Calorimeter

Figure 3.10 shows the calorimeter assembly, the calorimeter having been machined from an OFHC (Oxygen Free High Conductivity) grade copper rod into a " ⊔ " shaped vessel of 5 cm^3 capacity. In order to obtain rapid thermal equilibration of the powdered sample, four thick vanes were silver-soldered on to the inside surface of the calorimeter, in similar fashion to that described by Kirkham and Yates (1968), and the powdered sample compacted into the calorimeter until full using a 15 mm diameter polished die under a pressure of 1 - 2 tons/sq. in. The temperature of the sample and calorimeter combined could be raised above that of the surroundings by passing a DC current through a (40 swg) copper constantan heater, H_1, having a resistance at room temperature of approximately 300 ohms. Good thermal contact between the heater wire and the calorimeter surface, as well as between each successive layer of heater coil, was promoted by the application of a thin layer of GE 7031 low temperature varnish.

The calorimeter was pressed against a copper lid by means of three brass springs and nuts bolted through stainless steel rods of 1.5 mm diameter suspended from the copper sample holder. So as to ensure good thermal contact between the surfaces of the sample and the copper lid, a thin layer of thermally conductive compound was applied to both surfaces, the same amount of compound being used for each run. The temperature of the calorimeter as a whole was measured by means of a thick platinum film thermometer attached to the copper sample holder which, in turn, was supported by a low thermal conductivity stainless steel tube of 2 mm diameter extending inside the copper can radiation shield from the copper block.

3.3.2 (b) Adiabatic Radiation Shield

The radiation shield had the form of a cylindrical copper can, 5.5 cm in height, 3.5 cm in diameter and 2 mm in thickness, with a hole at the bottom. The calorimeter was surrounded by this shield screwed to the copper block on which the heater, H_2, was wound non-inductively with 40 swg copper constantan wire of approximately 300 ohms resistance. All electrical wires connected to the calorimeter were passed through the small holes provided in the copper block and thermally anchored to it by soldering on to the gold-plated strips, these strips each being fixed to the copper block by a thin layer of araldite. In order to minimize heat leakage at room temperature along the wires to the calorimeter, the electrical wires were wrapped around the copper block several times and glued with GE 7031 low temperature varnish before being thermalised to the brass flange, C.

The adiabatic control of the radiation shield and the calorimeter was monitored by means of a gold-0.03% iron/chromel differential thermocouple in conjunction with a Thor Cryogenic temperature controller which could provide joule heating through the heater H_2 (see Figure 3.10). To minimize the heat leak from the calorimeter along the thermocouple wires, which were of 0.08 mm diameter, the latter were given a helical twist throughout the whole of their length. One junction of the thermocouple was attached to the copper lid of the calorimeter whilst the other junction was attached to the inner surface of the copper block radiation shield. In order to obtain good thermal contact between both surfaces, the junctions of the thermocouple were wrapped with gold-plated copper strips before being inserted and then screwed into the small holes. The copper rod, 10 mm in diameter and 25 mm in length, was silver-soldered on to the copper block, its surface being wound non-inductively with 40 swg copper constantan wire of approximately 150 ohms resistance (see H_3 in Figure 3.10). Spurious readings at high temperature ($T > 200^{\circ}K$), due to large fluctuations in the heat leakage between the radiation shield and the outer can (at $77^{\circ}K$), could be minimized through H_3. This heater was driven by a DC regulated voltage supply with a power slightly less than the amount required by the radiation shield to maintain the temperature difference between them. This ensured that the amplitude of the heat pulse delivered by the temperature controller was small and, hence, the fluctuation was small.

Finally, the radiation shield assembly was supported by a low thermal conductivity stainless steel tube of 10 mm diameter, extending from the brass strip attached to the brass flange, C, by means of two 8 BA bolts. Thus, large temperature differences between them could be obtained without boiling off too much liquid nitrogen coolant during experimental operation.

3.3.2 (c) Thermometry

Heat capacity measurements at low temperatures require the use of a reliable thermometer of small heat capacity. Two important factors must be considered before choosing a thermometer for this purpose: (i) its sensitivity and (ii) its reproducibility.

A thick platinum film resistor, grade I, supplied by Matthey Thermafilm Temperature Detectors, was used as a thermometer for measuring the temperature of the calorimeter over the temperature range $30 - 300^{\circ}K$. It possessed all of the characteristics of the standard platinum resistance thermometer, i.e. reproducibility and the property of resistance/temperature dependence. In the present work, the chief advantages were its smallness of size and ease of attachment to the calorimeter.

Figure 3.11(a) shows the actual size of the platinum film

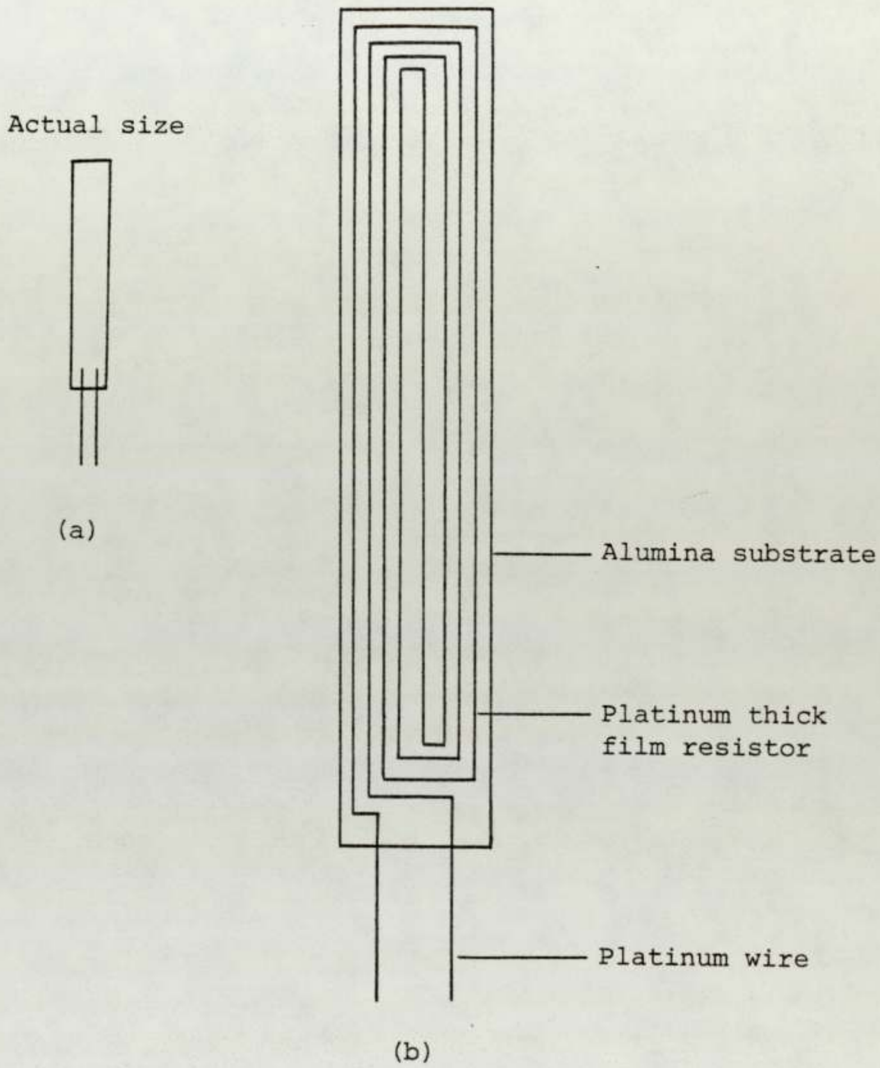

FIGURE 3.11 Diagram of the platinum film thermometer

thermometer while Figure 3.11(b), by enlargement, indicates its maximum dimensions more clearly. The thermometer was calibrated against standard germanium and rhodium-iron thermometers. In addition, Figure 3.12 shows the resistance-temperature characteristics of the platinum film thermometer, its usable temperature range being seen to be from 30°K up to about 300°K with a sensitivity of approximately 0.4 ohms/°K. A sensitivity of 2.5mK/μV could be obtained by passing a constant current of 1 milliampere, as detected by means of the Solartron A203 Digital Voltmeter which has a resolution of 1 μV.

3.4 The Electrical Circuits for Heat Capacity Measurements

Figure 3.13 shows the electrical circuits used for heat capacity measurements over the temperature range 1.5 - 30°K. The input pairs of current and voltage leads were connected to the head units of the Solartron Data Transfer Unit. The scanning of all input pairs was carried out by a relay driver and controlled by the controller. The operation could be repeated manually or automatically by a clock. The time between the various steps of the scan could be varied from one second to 30 minutes. The interface provided the input to the Solartron A203 Digital Voltmeter, in either the DC or AC mode, and returned the data via the output driver to the data recording device which, for the present work, was an Addmaster-35 typeprinter.

A stabilized DC power supply, type 305 (0 - 30V, 0 - 5A), and separate circuit DC power supply, type AS 1164.2 (0 - 30V, 0 - 1A), were used together to supply the current in conjunction with a decade resistance box which enabled the current and the voltage output to be varied from 1 - 1000 μA and 0.005 - 30 volts respectively.

The current through the heater and thermometer was determined by measuring the potential drop across a 1000 ohms standard resistance

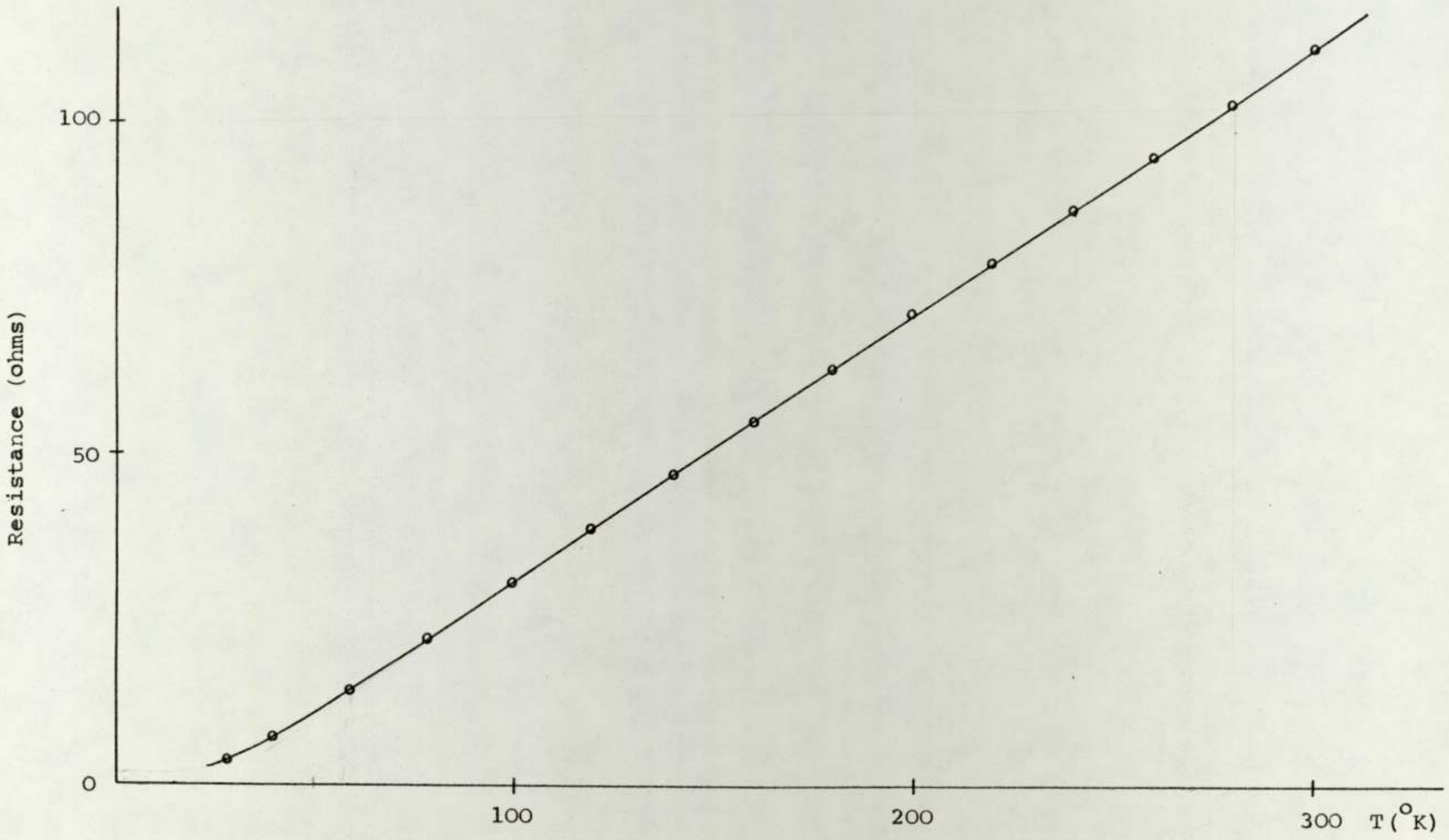

FIGURE 3.12 Resistance of the platinum thermometer against temperature.

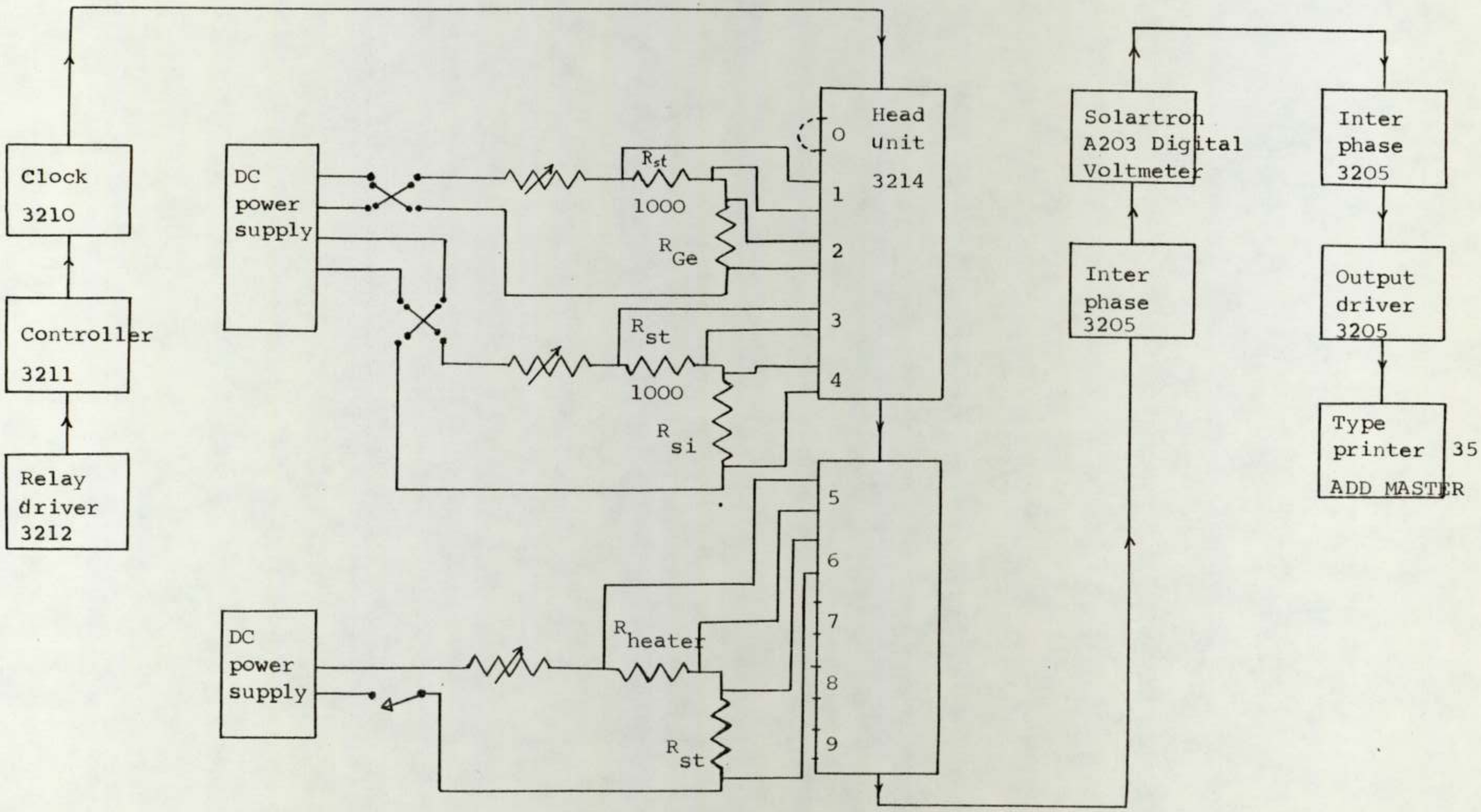

FIGURE 3.13 Electrical circuits for heat capacity measurement over the temperature range 1.5 - 30°K.

(Vitrohm type MM-2 with an accuracy ±0.01%).

Figure 3.14 shows the electrical circuit diagram for heat capacity measurement over the temperature range 30 - 300°K.

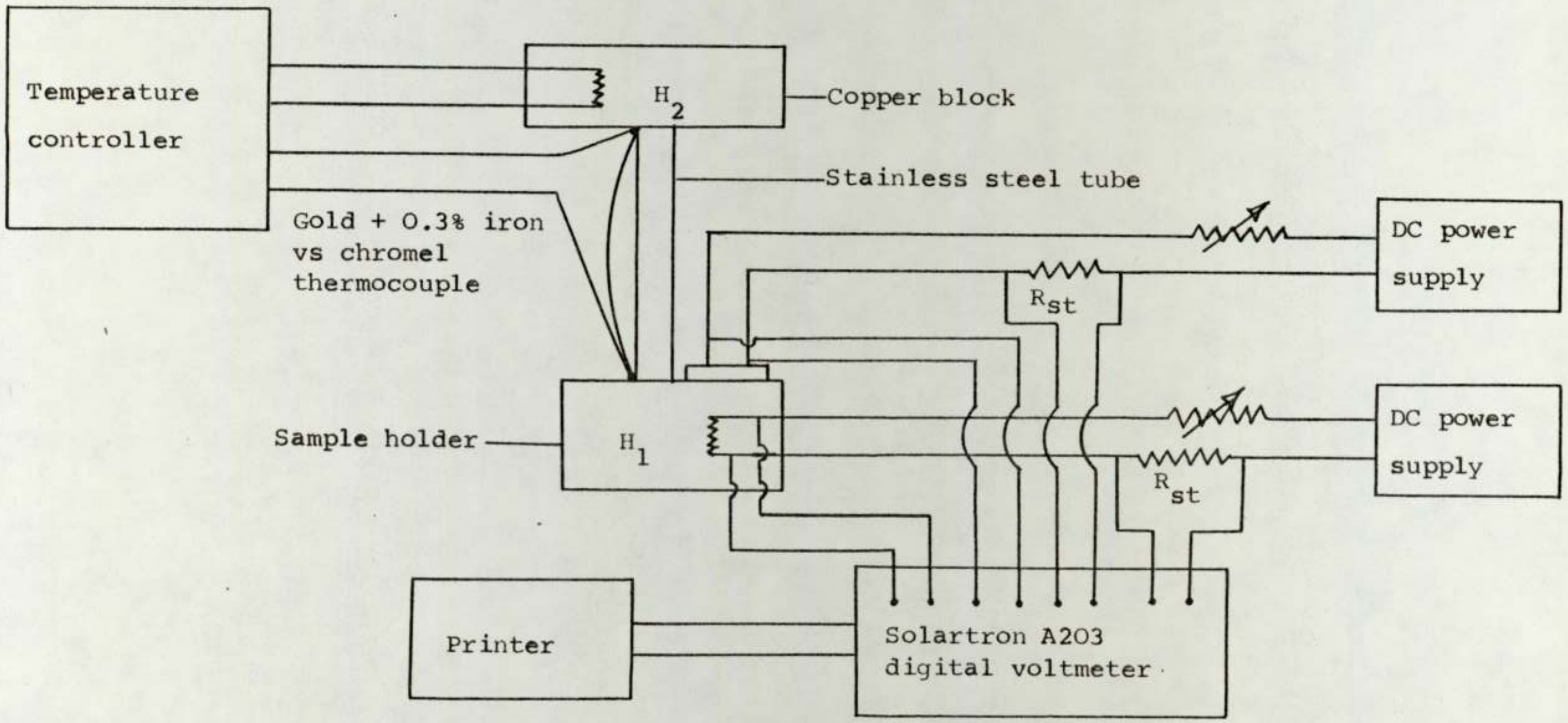

FIGURE 3.14 Electronic circuits of the heat capacity experiment for the temperature range 30 - 300°K.

CHAPTER 4

EXPERIMENTAL PROCEDURE AND RESULTS

CHAPTER 4

EXPERIMENTAL PROCEDURE AND RESULTS

4.1 Electrical Resistivity Measurements

4.1.1 Introduction

Electrical resistivity measurements were carried out for all spinel samples (i) to further characterize the specimens investigated, and (ii) as an auxiliary measure of the superconducting transition temperature, T_c.

4.1.2 Measurement Technique

The electrical resistivity measurements were carried out over the temperature range 2.0 - 300°K using a standard four-probe DC technique. The apparatus used for this purpose was originally developed for measuring the electrical resistivity of thin films - for details of the design and construction of the cryostat, see Mangkorntong (1977). The samples, in the form of hard sintered pellets, were filed into rectangular shaped slices of approximately 2 x 0.5 x 14 mm in size. Six electrical leads were then bonded to each sample with silver paint (see Plate3.7(c)) and tested for mechanical adhesion. The variation in sample temperature was measured by means of a standard germanium thermometer and calibrated gold-0.3% iron/chromel thermocouple. By passing a constant current (of the order of 100 μA) through the sample (from A to B), its resistance could be determined by measuring the voltage developed between either contacts C and D or contacts E and F (see Figure 4.1). The absolute value of the electrical resistivity, $\rho = R\frac{a}{l}$, could then be calculated from the resistance, R, of the sample and the measured sample dimensions, l and a, where l is the distance between C and D or E and F and a the cross-sectional area of the sample.

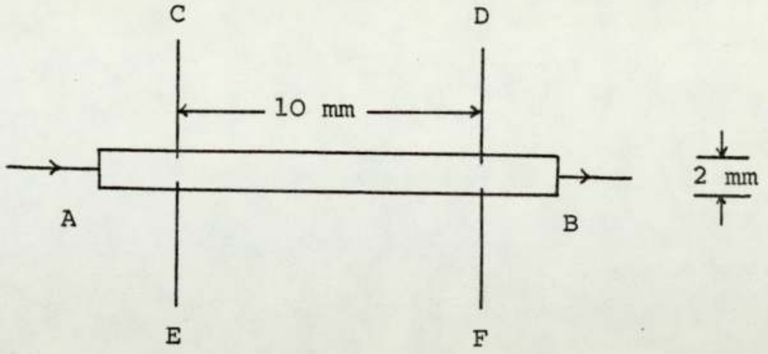

FIGURE 4.1

The sample configuration for electrical resistivity measurements

4.1.3 Results for $LiTi_2O_4$

In the case of $LiTi_2O_4$, X-ray diffraction investigation showed that the sample of nominally stoichiometric composition was substantially spinel phase, with negligible scattering from other sources (see Plate 3.4). Resistivities of a few further samples with either an excess or a deficiency in TiO_2 were also investigated. These samples were found to contain slight traces (<5%) of an impurity phase in their diffraction patterns.

The results of the resistivity measurements of all samples studied are shown in Figures 4.2 to 4.5, from which it can be seen that the resistivities exhibit a sharp decrease as the temperature is lowered through their respective transition temperatures. However, in the absence of perfect stoichiometry, the resistivity of $LiTi_2O_4$ can subsequently increase at still lower temperatures as shown in the figures. This curious state of affairs was first discovered as far back

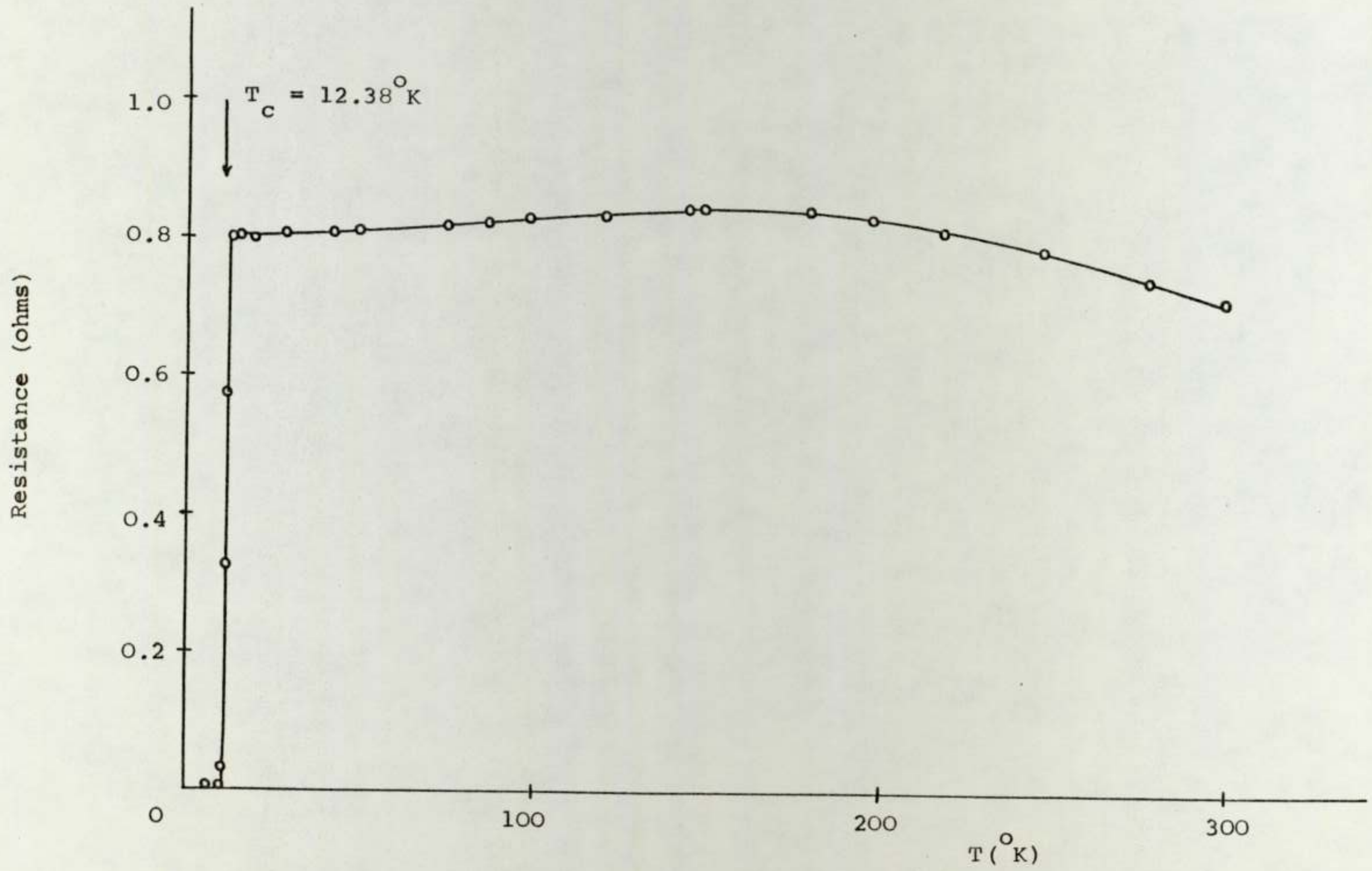

FIGURE 4.2 Resistance versus temperature for $LiTi_2O_4$.

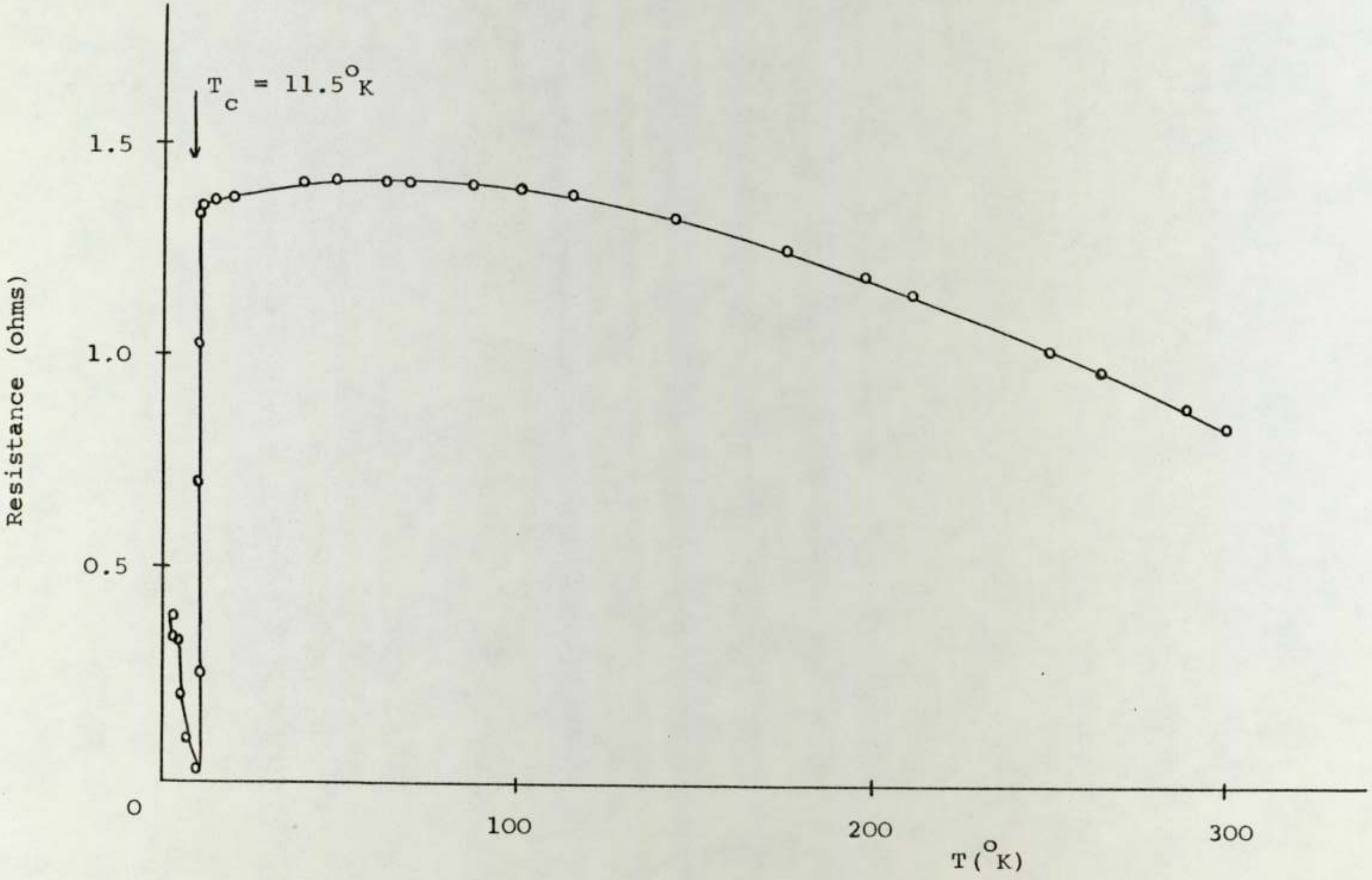

FIGURE 4.3 Resistance versus temperature for $LiTi_2O_4$ + 0.4% TiO_2.

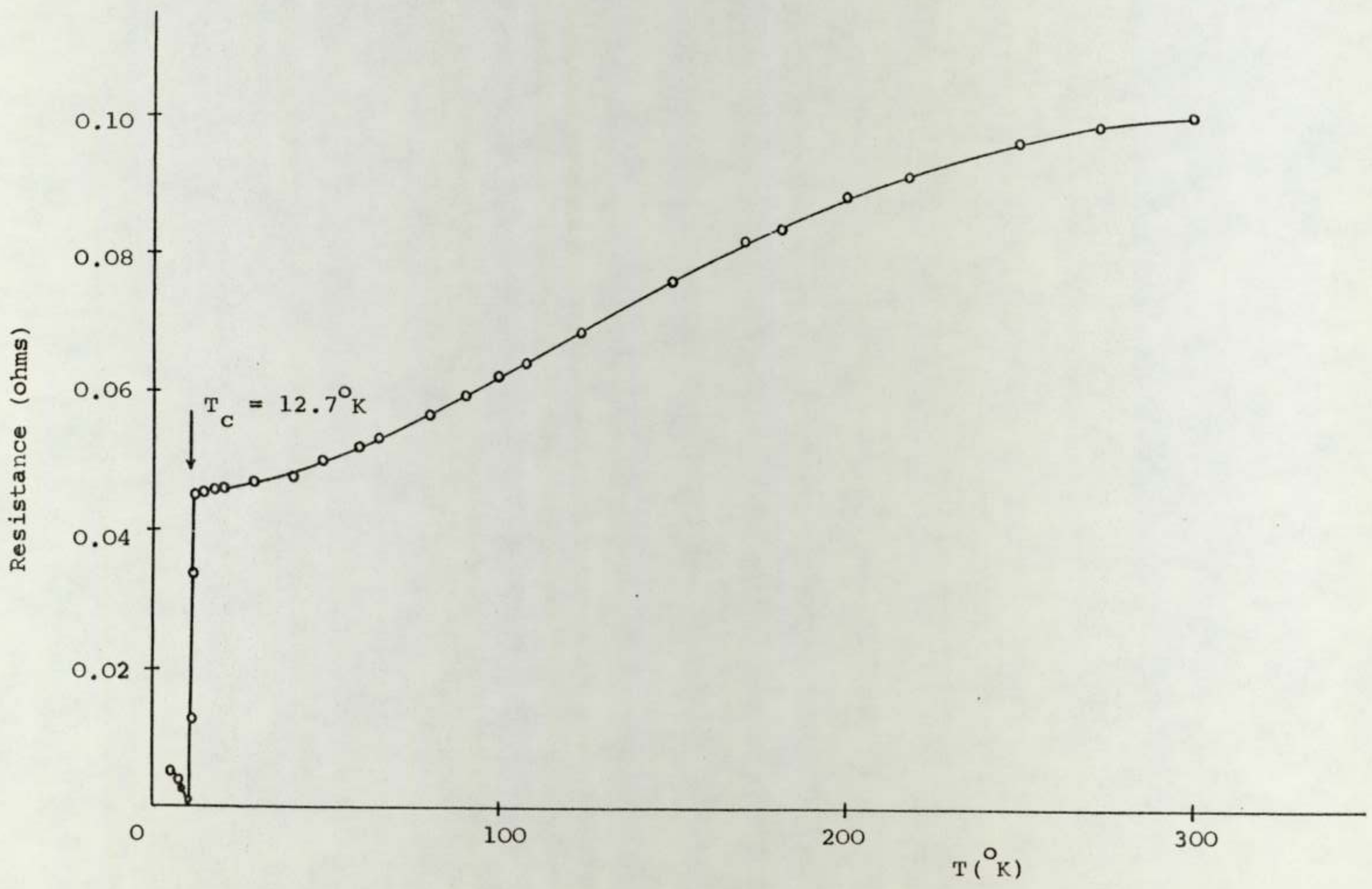

FIGURE 4.4 Resistance versus temperature for $LiTi_2O_4$ - 5.0% TiO_2.

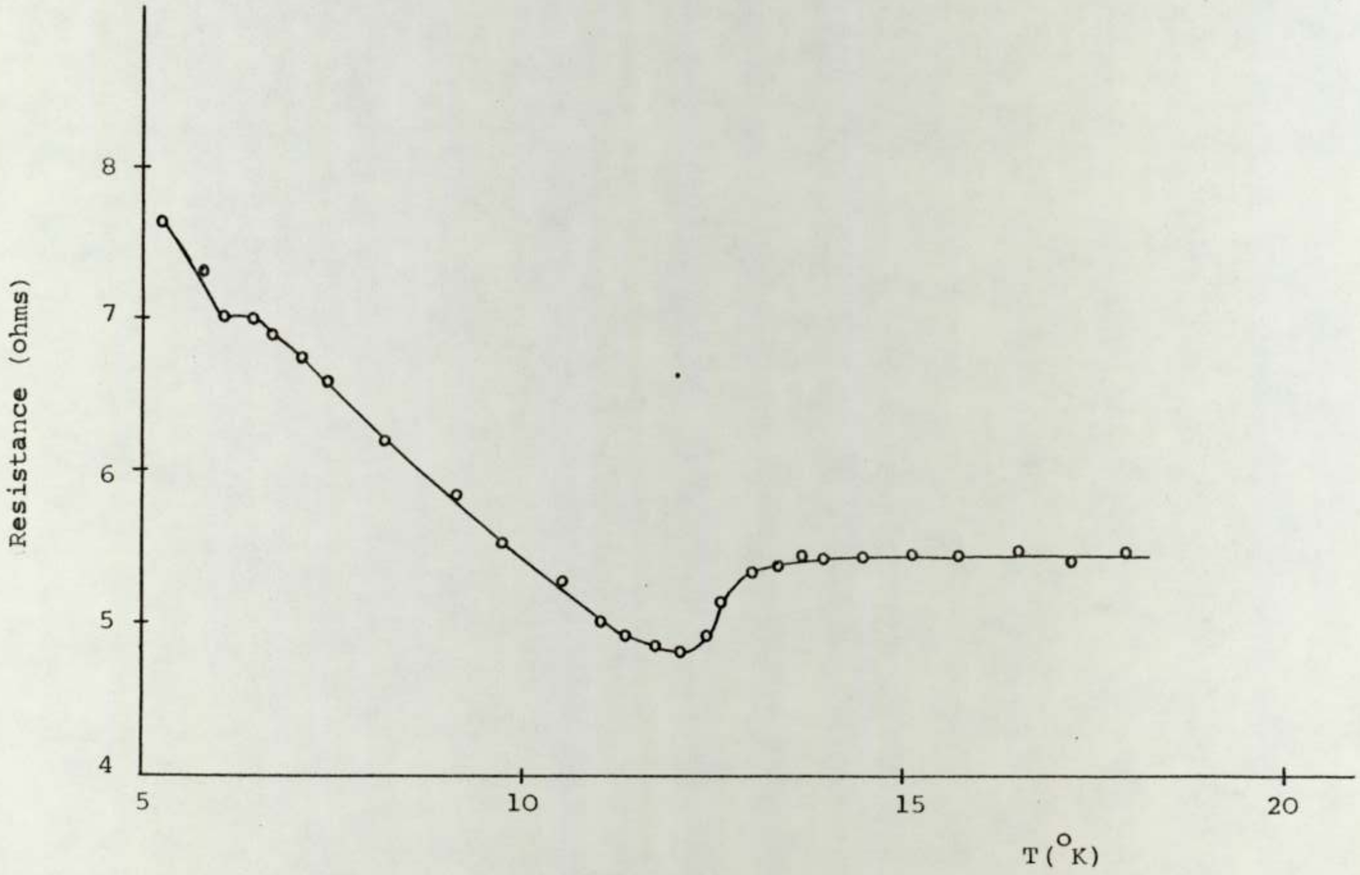

FIGURE 4.5 The resistance versus temperature for $LiTi_2O_4$ + 1.5% TiO_2.

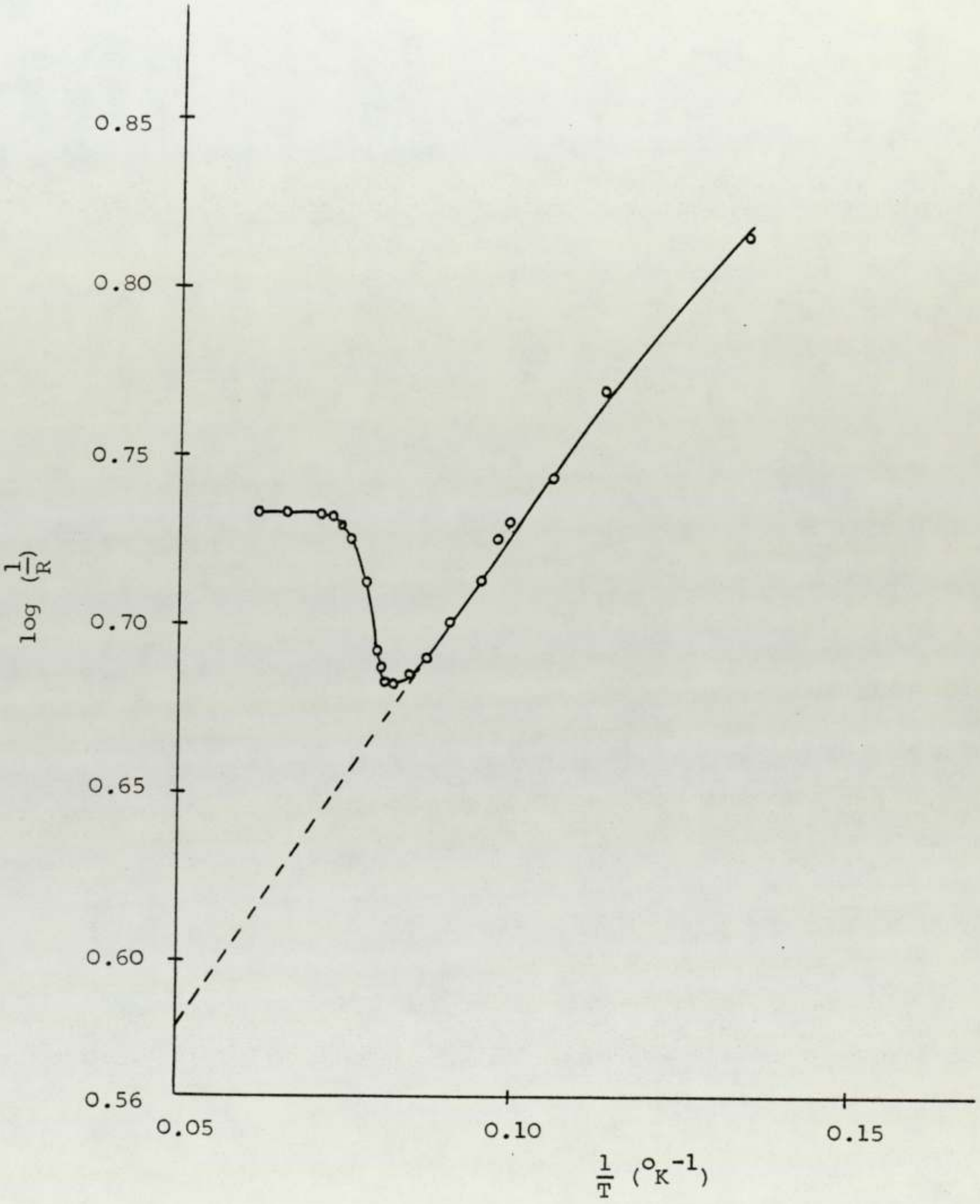

FIGURE 4.5(a) The plot of log $(\frac{1}{R})$ versus T^{-1} for $LiTi_2O_4$ + 1.5% TiO_2.

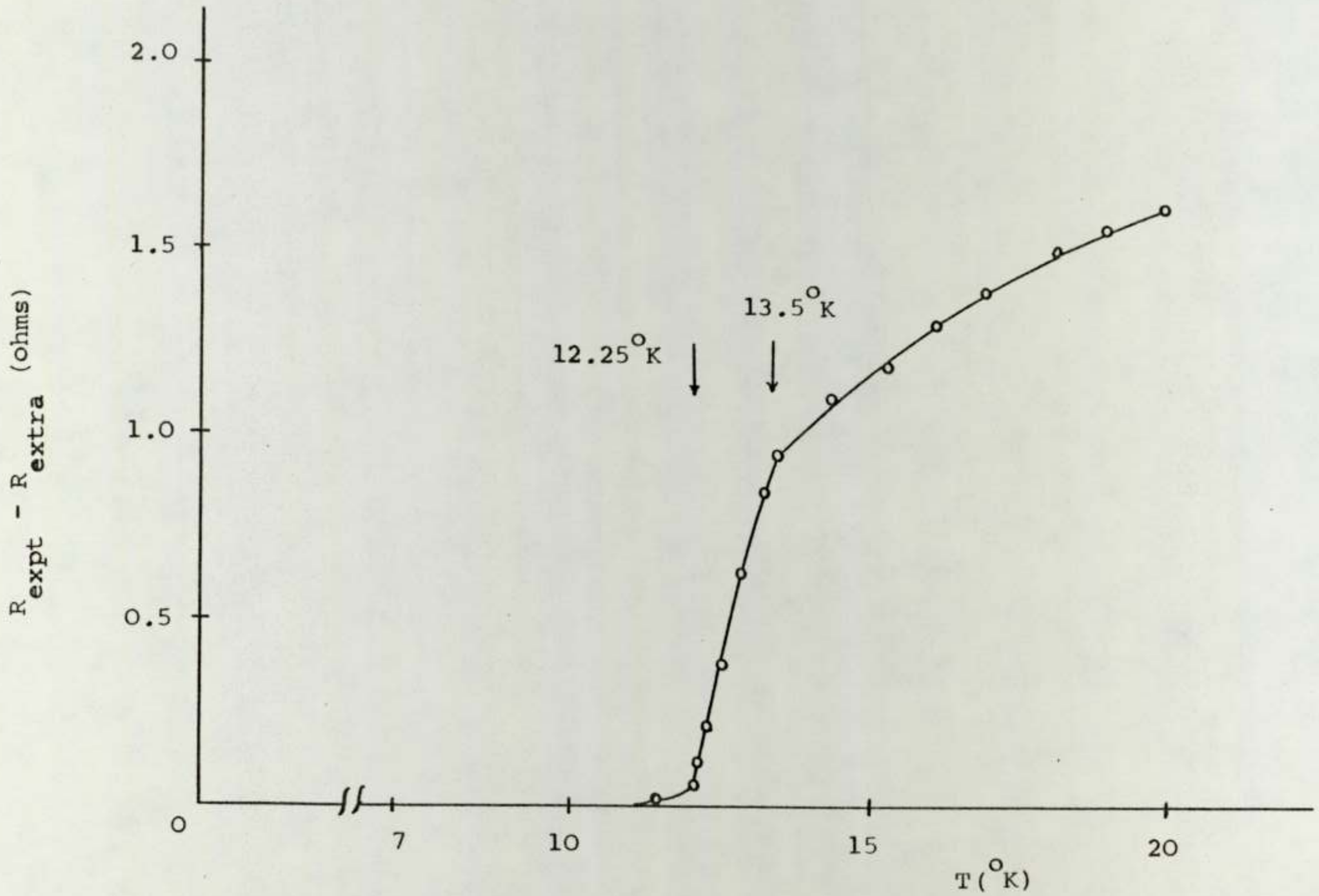

FIGURE 4.5(b) The plot of $R_{expt} - R_{extra}$ (from Figure 4.5(a)) versus temperature for $LiTi_2O_4$ + 1.5% TiO_2.

as the 1930s, yet only recently has a proper explanation been given by Kondo (1964) - this phenomenon now being known as the Kondo effect. In "simple" metals (such as copper, zinc and the noble metals), the Kondo effect is observed when trace amounts of transition elements are present, these giving rise to spin order which competes with the superconducting mechanism. The corresponding effects observed with $LiTi_2O_4$ are thus indicative of excess Ti^{3+} ions.

4.1.4 Results for $CuRh_2Se_4$

This sample was investigated briefly and the results of the resistivity measurements are shown in Figure 4.6. For this $CuRh_2Se_4$ sample, the resistivity was temperature dependent (above the superconducting transition). The onset of the transition temperature for this spinel was found to be at $3.48^\circ K$, whilst the breadth of the transition was $0.2^\circ K$. The resistivity ratio, $\rho_{300} / \rho_{4.2}$, was determined as being 2.04.

4.2 Heat Capacity Measurements over the Temperature Range 1.5 - $30^\circ K$

4.2.1 The Thermal Relaxation Method

The basic idea behind this method is illustrated in Figure 4.7 via an electrical analogy (Bachmann et al., 1972). Under steady state conditions, power P (current i) flows through the system. If the power is cut off, the temperature, T, (voltage = iR), decays to T_o (V = 0) with a time constant C/k(RC), where C is the heat capacity and k the thermal conductance.

In practice, in order to simplify the mathematical problems which are associated with the analysis, it is usually necessary to make some further assumptions. For example, Bachmann et al. (1972) have made the assumption that the lateral heat flow (e.g., from the centre of the

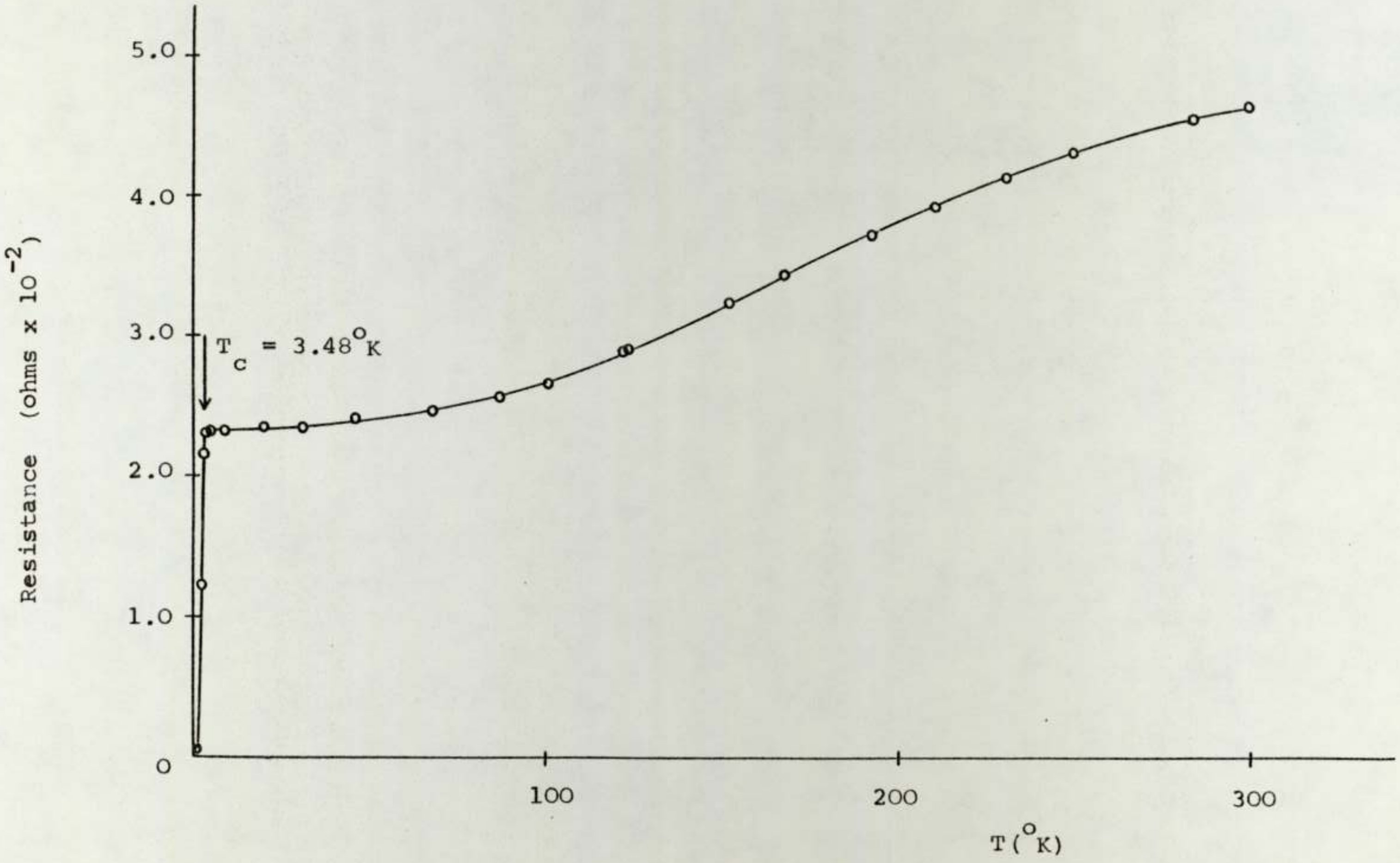

FIGURE 4.6 Resistance versus temperature for $CuRh_2Se_4$.

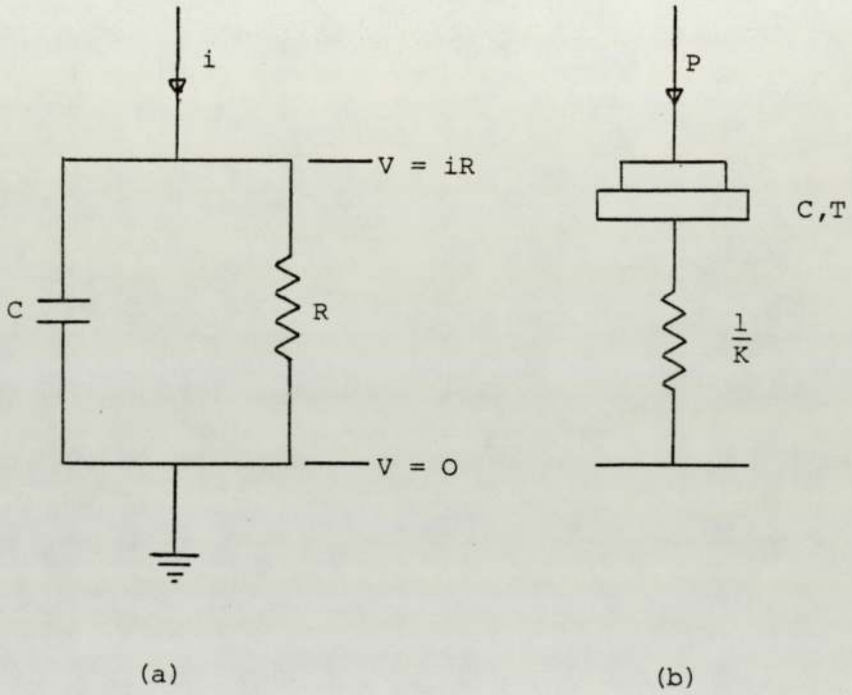

FIGURE 4.7 Thermal relaxation method:
(a) electrical analogy, and
(b) schematic heat flow circuit
(Bachmann et al., 1972).

sample or calorimeter towards the wires) is much faster than the longitudinal heat flow down the wires. This enabled them to adopt a one dimensional model for heat flow within the system comprising the sample and calorimeter at temperature, T, the linking wire and the copper block heat reservoir at temperature, T_o. In these circumstances, the heat balance equation can be written as follows:

power into sample = power out (along the wires)

$$+ \left(\frac{\partial}{\partial t}\right) \text{ (heat in sample)}$$

or

$$P = Ak_o \frac{\partial T}{\partial z} + C(T) \frac{\partial T}{\partial t} \qquad \ldots\ldots (4.1)$$

where P is the power put into the sample, A is the cross-sectional area of the wire, k_o is its thermal conductivity and the heat flow is along the z axis.

Integrating equation (4.1) over the length of the wire yields:

$$C(T) = \left(\frac{dT}{dt}\right)^{-1} \{ P - \int_{T_o}^{T} k(T)' \, dT' \} \qquad \ldots\ldots (4.2)$$

where k is the thermal conductance of the wire and $k(T) = k_o(T) \times \frac{A}{l}$ (l being the length of the wire).

If the sample temperature, T_1, is raised above the block temperature, T_o, so that $T_1 - T_o$ is still small, the integral in equation (4.2) is simply:

$$\int_{T_o}^{T} k dT' = k(T_{av}) \Delta T \qquad \ldots\ldots (4.3)$$

where $T_{av} = \frac{1}{2}(T + T_o)$ and $\Delta T = T - T_o$.

If the relaxation time constant, τ_1, changes by less than 1%, $T_1 - T_o$ is "small enough" for heat capacity measurements to an accuracy of 1%, thus implying that:

$$\frac{dT}{dt} = d(\Delta T)/dt \qquad \ldots\ldots (4.4)$$

as long as the block temperature is stabilized such that $dT_o/dt \ll dT/dt$.

When the power P is switched off suddenly at time t = 0, we have:

$$C(T) = - \frac{k(T_{av}) \Delta T}{dT/dt} \quad \ldots\ldots$$

$$= - \frac{k(T_{av}) \Delta T}{d(\Delta T)/dt}$$

$$= - \frac{k(T_{av})}{d(\ln \Delta T)/dt} \quad \ldots\ldots (4.5)$$

If C is constant over the temperature interval $T_1 - T_o$, then:

$$\frac{d(\ln \Delta T)}{dt} = - \frac{k}{C} = - \frac{1}{\tau_1} \quad \ldots\ldots (4.6)$$

where $\tau_1 = \frac{C}{k}$.

Since at t = 0, $\Delta T = T_1 - T_o$, it follows that:

$$\ln \left\{ \frac{(\Delta T)}{T_1 - T_o} \right\} = - \frac{t}{\tau_1} \quad \ldots\ldots (4.7)$$

i.e.,

$$\Delta T(t) = (T_1 - T_o) \exp \left(- \frac{t}{\tau_1}\right) \quad \ldots\ldots (4.8)$$

Thus, the heat capacity, C, can be determined by measuring k and τ_1. Figure 4.7(a) shows the sample thermal relaxation curve.

4.2.2 Experimental Procedure

In the experiments to be described, a sample prepared in the form of a sintered pellet was filed into a square-shaped slice, approximately 10 x 10 x 0.5 mm in size and 150 - 500 mg in weight. This sample was bonded to the rear (insulating) side of the silicon calorimeter with a thermally conductive compound (Thermal Heat Sink Compound, RS Components Limited), the amount of compound used each time being of the order of 6 mg. A thin layer of compound was applied to the sample surface and to the reverse side of the calorimeter and the two "tinned" faces were then pressed together. At the same time, it was found

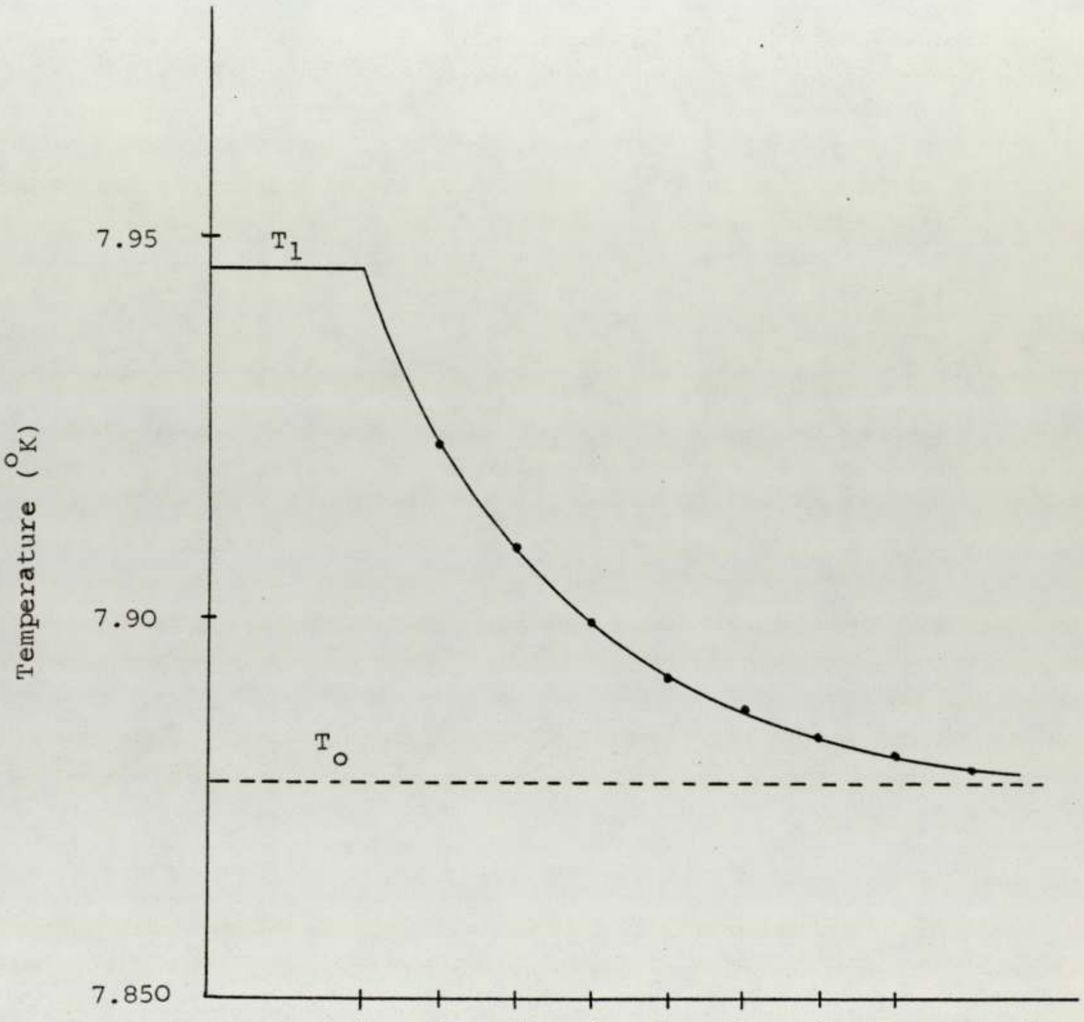

FIGURE 4.7(a) Sample thermal relaxation time.

necessary to rub the sample and calorimeter against each other in order to remove any entrapped air bubbles. Subsequently, since the calorimeter and lead wires were fragile, particular care had to be taken when changing samples. By using a demountable holder, as shown in Plate 3.7(a), the calorimeter holder could be removed from the cryostat and supported on it securely whilst the bonding compound was cleaned off and a fresh sample mounted.

After bonding the sample, the calorimeter holder was removed from the demountable holder and carefully mounted on to the copper block using the technique described in Section 3.3.1(c). Having connected all electrical leads, the whole assembly was enclosed in the brass can which was, in turn, bolted to the brass flange with an intermediate indium ring as vacuum seal. The apparatus was evacuated by, firstly, a rotary pump and, subsequently, by a diffusion pump. When a pressure of about 10^{-5} torr had been established, the outer dewar of the liquid helium cryostat was filled with liquid nitrogen. Having pre-cooled overnight with liquid nitrogen, liquid helium could be slowly transferred from the storage dewar into the helium cryostat using the technique described previously in Section 3.3.1(c). Since an exchange gas was not used, this stage had to be continued for 4 - 5 hours in order to attain thermal equilibrium at liquid helium temperature.

Prior to taking any heat capacity measurements, the calorimeter (with or without sample) was allowed to reach equilibrium at temperature T_o (the same temperature as that of the copper block) by means of the block heater winding which was supplied by a regulated DC power supply; this temperature, T_o, actually being given by the corresponding silicon resistance, R_o. Once thermal equilibrium had been attained (usually after about 10 minutes), the film heater of the calorimeter was switched on so that the power input, P, was dissipated into the calorimeter and sample. This established the rise in temperature of the system (calorimeter plus sample) and could be monitored through the change in resistance of the silicon thermometer. At first, the resistance increased rapidly before gradually slowing down towards the next equilibrium temperature, T_1, corresponding to the silicon resistance, R_1, as indicated by a constant temperature. At this stage, the power P was switched off and the temperature of the system allowed to decrease back to the original temperature T_o. The resistance, R_o, the power input, P, and the change in resistance per second of the silicon thermometer were recorded. This procedure was repeated until the whole of the temperature range to be studied had been characterized. The helium exchange gas was allowed into the system in order to re-calibrate the silicon thermometer and to avoid shifts in temperature after its thermal cycling to room temperature.

4.2.3 Determination of Heat Capacity

As described previously in Section 4.2.1, the heat capacity, C, can be determined if the thermal conductance, k, and the thermal relaxation time constant, τ_1, are known. The values of k and τ_1 are determined from experiment as follows.

4.2.3 (a) Thermal Conductance

The thermal conductance, k, is defined by the equation:

$$k = P/(T_1 - T_o) \qquad \text{......} \ (4.9)$$

where $(T_1 - T_o)$ is the temperature change produced by the heating power P. Hence, the value of k can be determined from the power P and the resistances R_o and R_1, corresponding to temperatures T_o and T_1. The power P was supplied by a DC power supply with a large load resistance (in the form of a decade resistance box) in series with the film heater. The current flowing through the film and voltage drop across it were measured using a Solartron A203 Digital Voltmeter in conjunction with a typeprinter unit as described previously in Section 3.4. In this way, the power P could be measured to an accuracy of 0.05%. The resistances R_o and R_1 were converted by a computer programme to find T_o and T_1 using the calibration described previously in Section 3.3.1(a)(vi). The temperature differences, $(T_1 - T_o)$, observed were normally within the range 50 - 100 mK. By using pure gold wires, the values of k were found to be between 10^{-6} - 10^{-4} watt/°K, corresponding to a power dissipation of 10^{-7} - 10^{-5} watt.

4.2.3 (b) The Relaxation Time Constant

In order to determine the thermal relaxation time constant, τ_1, the change in resistance of the silicon thermometer, recorded after switching the power P off, was interpolated by a computer programme to find the corresponding temperatures using the calibration equation (3.3). Since the temperature change, $\Delta T(t)$, varies exponentially with time, as explained in Section 4.2.1, τ_1 was determined by fitting T(t) to an exponential function using the method of least squares. The values of τ_1 recorded exponentially ranged from 1 to 120 seconds, with typical values of a few seconds. It was found that the τ_1 values were reproducible to 1%.

4.2.4 Test of the Method of Measurement

For a test of the method of measurement, the heat capacity of 451.6 mg of niobium was measured between 2°K and 10°K. This sample, obtained as 99.99% pure from Metals Research Limited, was cut into a thin wafer of approximately 7.0 mm diameter and 0.5 mm thickness. Niobium was chosen as a test sample because of its superconductivity allied with a high transition temperature, thus resembling, in this respect, the spinel compounds in which we were interested. The test results displayed in Figure 4.8, and compared with those of Chou, White and Johnston (1958), showed that this sample of niobium became superconducting with a $T_c = 9.25 \pm 0.05^{\circ}K$. The values of $\gamma = 86\ \mu J/g - {}^{\circ}K^2$ and $\beta = 1.4 J/g - {}^{\circ}K^4$ derived from this graph are in good agreement with those of Chou et al.

For calibration purposes, the heat capacity of gold was also measured over the temperature range 4.2 - 30°K. The results of this investigation on a sample of 146.4 mg weight are shown in Figure 4.9. Comparison with earlier measurements by Martin (1966) shows that the maximum deviation of the present data points from his smooth curve is less than 1%.

4.2.5 Results from Heat Capacity Measurements at Low Temperatures (1.5 - 30°K)

Heat capacity measurements within the temperature range 1.5 - 30°K were carried out using the thermal relaxation technique, as described in Sections 4.2.1 - 4.2.3. The heat capacity data obtained in this way will now be described in more detail.

4.2.5. (a) Heat Capacity for the Empty Calorimeter

Before carrying out any of the investigations on the heat capacity of the spinel samples, measurements were carried out on the empty calorimeter, together with 6 mg of a thermally conductive compound, over the temperature range 1.5 - 30°K. These results were to be used to correct the later measurements for the effect of the calorimeter and are therefore summarized in Table 4.1.

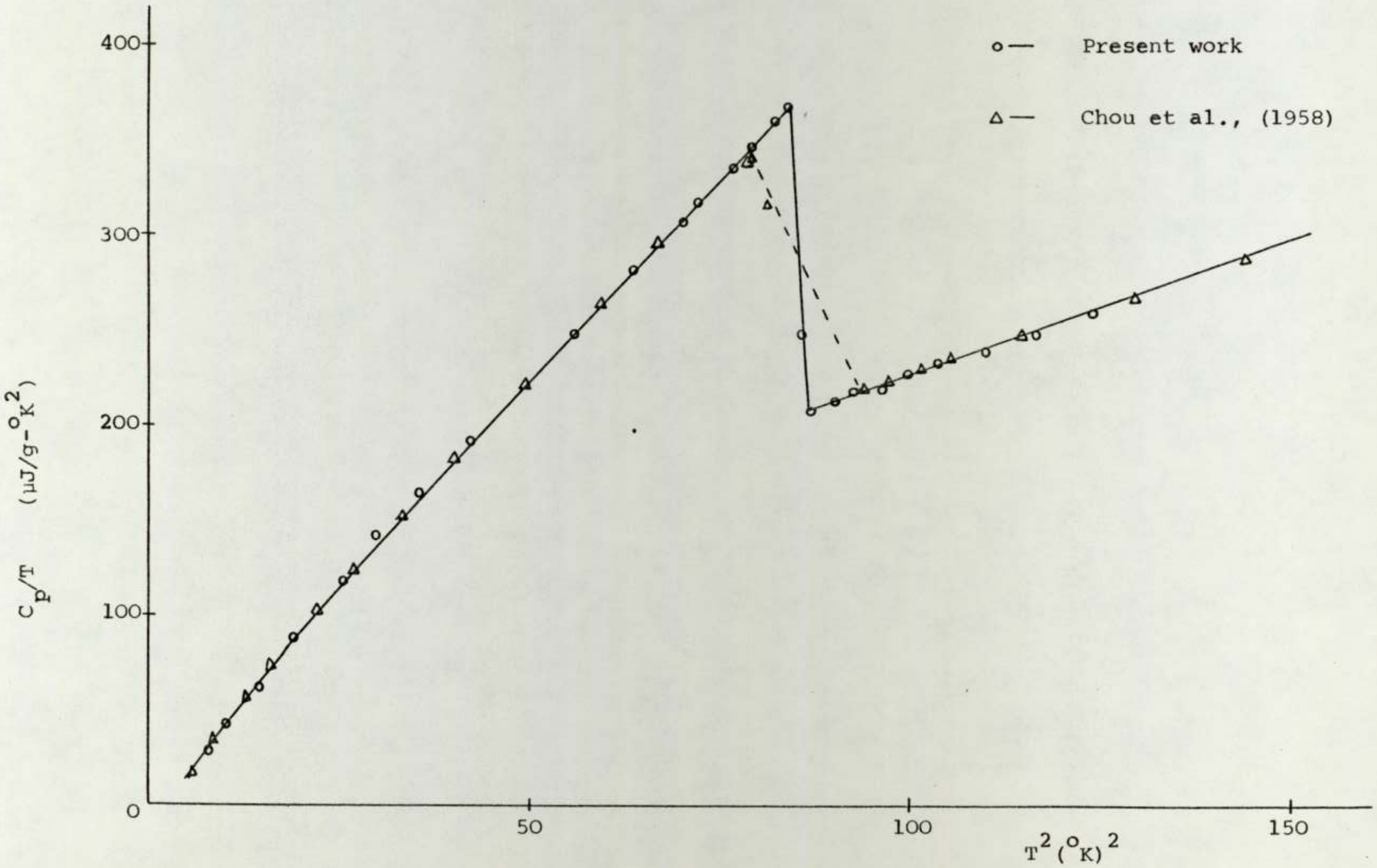

FIGURE 4.8 Heat capacity of niobium.

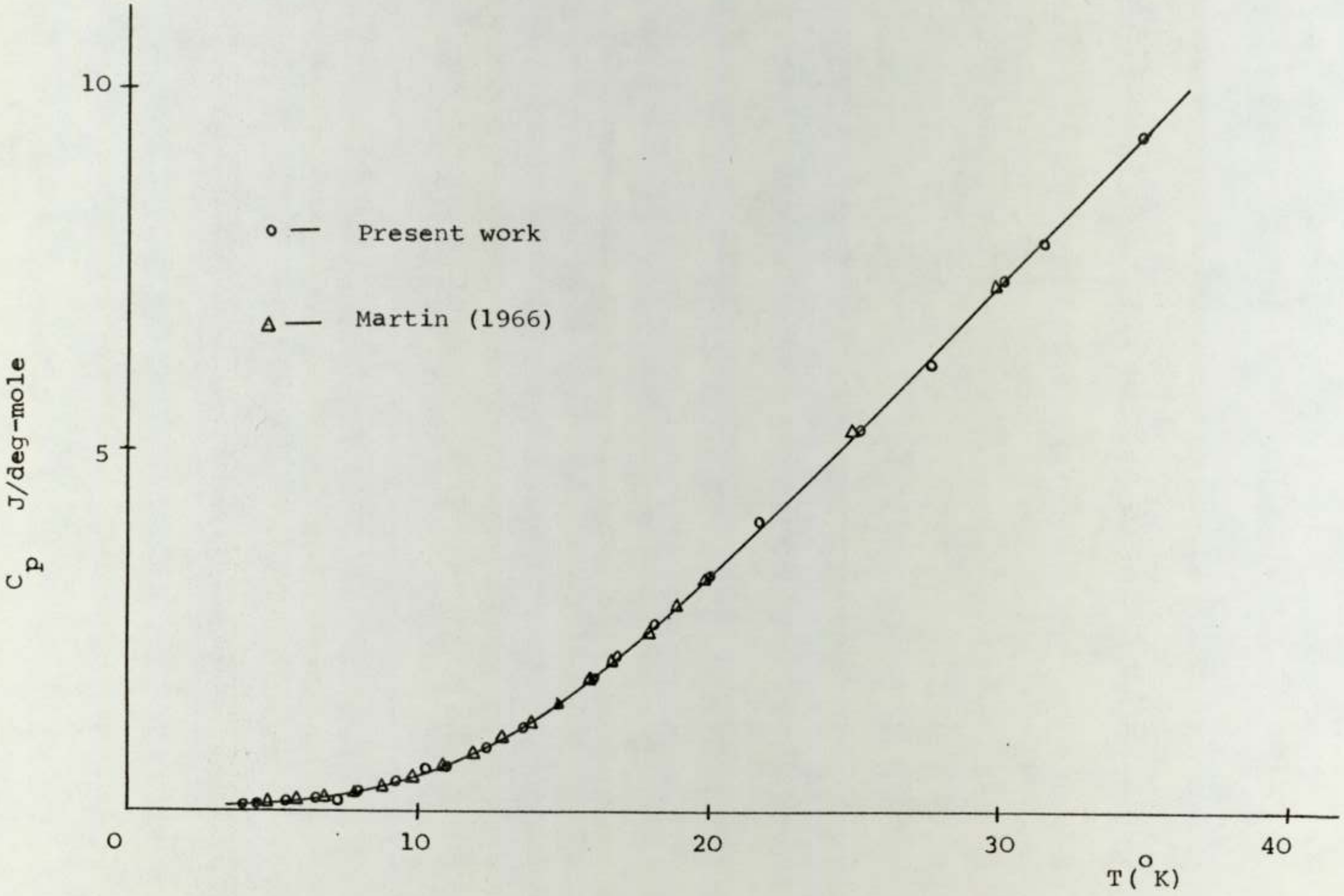

FIGURE 4.9 Heat capacity of gold.

TABLE 4.1

Heat capacity of empty calorimeter with 6 mg of a thermally conductive compound.

T (^{o}K)	C_p (mJ/^{o}K)	T (^{o}K)	C_p (mJ/^{o}K)
1.84	0.0112	10.07	0.423
2.05	0.0120	11.13	0.542
2.45	0.0151	12.31	0.685
3.15	0.0223	13.59	0.842
3.75	0.0283	15.03	1.05
4.26	0.0408	16.61	1.28
4.53	0.0446	17.45	1.41
5.01	0.0589	18.36	1.57
5.53	0.0811	19.78	1.83
6.11	0.107	20.29	1.94
6.75	0.145	22.42	2.39
7.46	0.194	24.78	2.90
8.25	0.233	27.39	3.52
9.16	0.335	30.26	4.27

4.2.5 (b) Results for $LiTi_2O_4$ over the Range 4 - 30°K

For heat capacity measurements over the temperature range 4.2 - 30°K, the silicon calorimeter was bonded with 185 mg of $LiTi_2O_4$ sample. The results of the observed molar heat capacity of $LiTi_2O_4$ within this temperature range (4.2 - 30°K) are given in Table 4.2 in which the data are presented as heat capacity (C_p), temperature (T), in columns 1 and 2 respectively. This data were obtained by subtracting the heat capacity of the empty calorimeter from the overall heat capacity of the calorimeter plus the $LiTi_2O_4$ sample. Values of the heat capacity of the empty calorimeter were read from the optimised smooth curve through the observed data points described in Section 4.2.5 (a) which were plotted on a large-scale graph. Figure 4.10 shows the plot of C_p/T as a function of the square of the temperature (T^2) displaying the characteristic superconducting feature of a sharp discontinuity in heat capacity, in this case at a temperature of 12.40 ± 0.05°K, in agreement with the resistivity measurements on the same sample. However, at temperatures well below this temperature (T_c), the heat capacity of $LiTi_2O_4$ decreases to a very small value. By extrapolation of the straight line passing through the data points above T_c to T = 0, the intercept gives a value for the low temperature electronic heat capacity, γ_o, of 22.5 ± 1.0 mJ/mole$^\circ K^2$. The corresponding slope yields a value for the Debye temperature at low temperature, θ_o, of 599 ± 6°K.

TABLE 4.2

The experimental values of the observed heat capacity of $LiTi_2O_4$ between 4.2 and 30^oK.

T (^oK)	C_p (J/mole-^oK)	T (^oK)	C_p (J/mole-^oK)
4.46	0.0369	9.29	0.381
4.61	0.0440	9.55	0.403
4.81	0.0559	9.81	0.441
5.06	0.0603	9.97	0.456
5.31	0.0685	10.06	0.467
5.57	0.0839	10.29	0.501
5.82	0.0984	10.54	0.529
6.06	0.114	10.81	0.595
6.31	0.125	11.25	0.639
6.54	0.141	11.40	0.638
6.79	0.156	11.59	0.673
7.09	0.173	11.85	0.694
7.34	0.199	12.01	0.730
7.54	0.213	12.15	0.729
7.77	0.234	12.25	0.637
8.03	0.258	12.41	0.590
8.51	0.309	12.61	0.505
8.80	0.333	12.70	0.423
9.05	0.356	12.75	0.415

TABLE 4.2 (continued)

T (°K)	C_p (J/mole-°K)
12.82	0.423
13.01	0.436
13.20	0.439
13.45	0.464
13.60	0.464
13.80	0.473
14.30	0.492
14.25	0.507
14.51	0.530
14.76	0.535
15.03	0.564
15.45	0.572
16.04	0.634
16.52	0.662
17.05	0.690
17.95	0.778
19.05	0.900
20.05	1.21
22.51	1.59
24.99	2.55
27.92	3.65
30.45	4.86

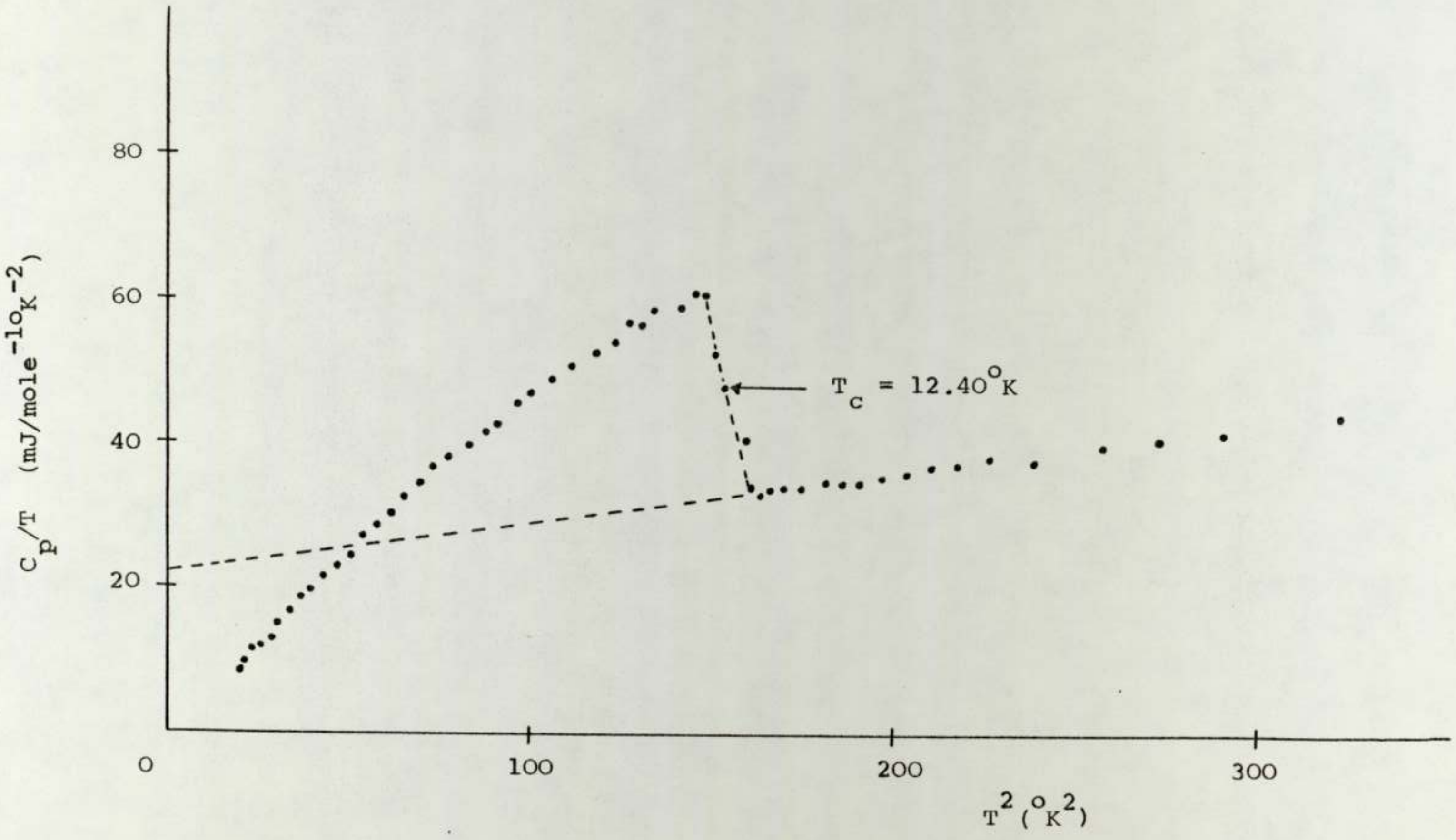

FIGURE 4.10 The plot of C_p/T against T^2 for $LiTi_2O_4$.

4.2.5 (c) Results for $CuRh_2Se_4$ over the Range 1.5 - 30°K

For heat capacity measurements involving $CuRh_2Se_4$ spinel samples, the silicon calorimeter was bonded with 192.6 mg of $CuRh_2Se_4$. The results of the observed molar heat capacity of $CuRh_2Se_4$ between 1.5 and 30°K are presented in Table 4.3, whilst Figure 4.11 shows the variation in C_p/T as a function of T^2. This latter curve exhibits a sharp discontinuity in heat capacity at a temperature of 3.50 ± 0.05°K, again in excellent agreement with the resistivity measurements. As with the previous sample, extrapolation of the straight line passing through the data points above T_c to $T = 0$ gives a value of γ_o of, in this case, 28.0 ± 1.0 mJ/mole-$^\circ K^2$ and (from the slope) a value of θ_o of 228 ± 5°K.

TABLE 4.3

The experimental values of the observed heat capacity of $CuRh_2Se_4$ between 1.5 and 30°K.

T (°K)	C_p (J/mole-°K)	T (°K)	C_p (J/mole-°K)
1.66	0.0364	3.52	0.163
1.77	0.0434	3.55	0.153
1.85	0.0493	3.63	0.162
1.96	0.0584	3.69	0.167
2.08	0.0713	3.76	0.171
2.28	0.0919	3.83	0.176
2.42	0.110	3.89	0.179
2.57	0.126	4.03	0.191
2.65	0.140	4.15	0.203
2.82	0.162	4.28	0.214
2.97	0.184	4.45	0.230
3.06	0.199	4.64	0.246
3.15	0.212	4.86	0.272
3.21	0.223	5.07	0.292
3.29	0.235	5.23	0.311
3.35	0.246	6.06	0.392
3.40	0.260	6.45	0.461
3.43	0.260	7.02	0.576
3.49	0.206	7.58	0.725

TABLE 4.3 (continued)

T ($^{\circ}$K)	C_p (J/mole-$^{\circ}$K)
8.07	0.809
8.52	0.916
8.92	1.02
9.47	1.19
9.87	1.30
10.97	1.66
12.18	2.10
12.98	2.45
14.02	2.89
15.16	3.40
17.04	4.45
18.18	5.08
19.44	5.95
20.02	6.40
21.11	7.12
22.35	7.99
24.02	9.53
25.88	11.20
27.28	12.44
28.89	13.96
29.64	14.77
30.16	15.32

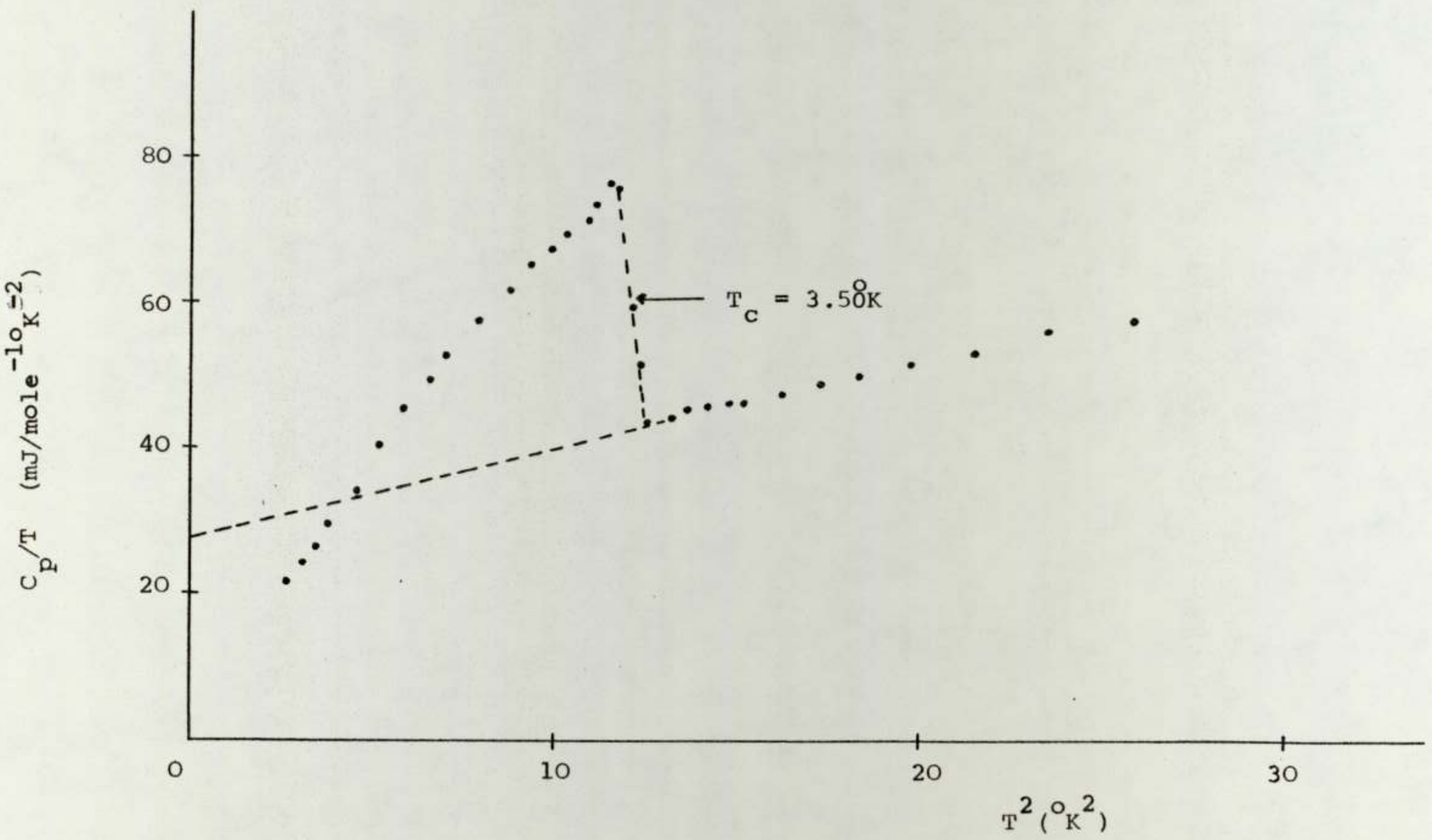

FIGURE 4.11 The plot of C_p/T against T^2 for $CuRh_2Se_4$.

4.3 Measurements of Heat Capacity over the Temperature Range 30 - 300°K

4.3.1 Experimental Procedure

The calorimeter was weighed empty prior to filling with the powdered sample which was compacted with a polished steel die under an applied pressure of 1 - 2 tons/sq in. The mass of the sample was determined by re-weighing the filled calorimeter, all weighings being carried out to an accuracy of 10^{-4} gm. A certain amount of thermally conductive compound was applied to the interface between the sample and copper lid surfaces in order to ensure good thermal contact between them. Having connected the electrical wires of heater H_1, the copper radiation shielding can was screwed on to the copper block. The entire assembly was then enclosed with the outer brass can fastened to the flange C by eight 4 BA nuts and bolts. The interface between them was sealed with an indium ring acting as a vacuum seal. The main cryostat was mounted on to the liquid helium dewar and pumped down to a pressure of $\sim 10^{-5}$ torr before filling the outer dewar with liquid nitrogen.

For measurements above 77°K, the inner dewar was filled with liquid nitrogen whilst liquid helium was used for measurements between 30°K and 90°K. Liquid helium was transferred from the storage dewar into the helium dewar using the technique described previously in Section 2.3.1(c). So as to prevent gas adsorption on to the surfaces of the copper and the powdered sample, no exchange gas was admitted to the system; consequently, the cooling stage was generally carried out overnight so as to ensure that the cryostat had reached thermal equilibrium.

When the calorimeter and its contents were at equilibrium, as indicated by the zero reading of the differential thermocouple, the Temperature Controller was set 0.000 mV and the control heater (which was connected to heater H_2) button switched on. The radiation shield was now maintained at a constant temperature with no power supply to the sample heater H_1. Having switched on H_1, the potential drop across it, the current passing through the standard resistance, the heating time and the rise in sample temperature were all recorded automatically by the printer unit at time intervals of, typically, two minutes. At high temperature, above 200°K, the heater H_3 was switched on to minimize the radiation losses between the can and the sample.

4.3.2 Method of Calculation

In order to determine the heat capacity of the sample alone, two sets of heat capacity results were needed - firstly, heat capacity measurements of the calorimeter alone (i.e., without any sample), and, secondly, containing an appropriate amount of sample. The difference between these two sets of data could then be attributed to the heat capacity of the sample which was determined as follows:

Let the power input to heater H_1 $(I^2R) = \frac{dQ_i}{dt} = P_i$

where i = 1 and i = 2 represent the experiments without sample and with sample respectively, and Q is the heat input in Joules.

The rate of increase in the calorimeter temperature = $(\frac{dT}{dt})_i = T_i'$

Thus, the heat capacity of the calorimeter alone, in the absence of sample, at a given temperature T is $C_1(T) = \frac{dQ_1(T)}{dT_1}$

$$= \frac{dQ_1(T)/dt}{dT_1/dt}$$

$$= \frac{P_i}{T_i'} \qquad \text{...... (4.10)}$$

Similarly, the heat capacity of the calorimeter with sample is

$$C_2(T) = \frac{P_2}{T_2'} \qquad \ldots\ldots (4.11)$$

Therefore, the heat capacity of the sample alone, of mass, m, at temperature T = $C_2(T) - C_1(T)$ ...... (4.12)

Therefore, specific heat of the sample

$$\equiv S(T) = \frac{C_2(T) - C_1(T)}{m} \qquad \ldots\ldots (4.13)$$

and the gram molecular heat capacity, C_p,

$\equiv S(T)$ x Molecular weight of sample ...... (4.14)

4.3.3 Estimated Accuracy of the Results

The accuracy with which the heat capacities could be obtained depended on all of the terms in the following equation:

$$C = \frac{VI}{(\frac{dT}{dt})} = \frac{P}{(\frac{dT}{dt})} = \frac{Q}{\Delta T} \qquad \ldots\ldots (4.15)$$

Under ideal conditions, the power P could be measured to an accuracy of greater than 0.05%, whilst a temperature change of $\frac{1}{400}$ °K was detectable with the Solartron A203 Digital Voltmeter. Thus, for $\Delta T = 1^{\circ}K$, the uncertainty of C for each experimental point was estimated as being 0.05% + 0.25% = 0.3% and, since the error due to weighing was very small (10 gm $\pm$ 10^{-4} gm), the specific heat, $S = \frac{C}{m}$, was estimated as being accurate to $\pm$0.4%. However, experimental error in practice could be two or three times greater than for the ideal condition and was therefore estimated to be within $\pm$1%.

For a calibration sample, the heat capacity of the calorimeter containing 10.5108 gm of copper powder was determined after measuring the heat capacity of an empty calorimeter over the temperature range 30 - 300°K. The copper powder sample, 99.9% pure from Koch-Light Co. Limited, was chosen as the test sample because, in addition to being easily and cheaply available, Furukawa, Saba and Reilly (1965) had previously conducted an extensive programme of work to standardize its specific heat below 300°K. A comparison of the present results with theirs is shown graphically in Figure 4.12, and the deviation of all the data points from a smoothed curve was found to be less than 1%.

4.3.4 Results from Heat Capacity Measurements at High Temperatures (30 - 300°K)

Heat capacity measurements for the spinel samples over the temperature range 30 - 300°K were performed in an adiabatic calorimeter, as described previously in Section 4.3.1. Details of the experimental data obtained in this way will now be described.

4.3.4 (a) Heat Capacity for the Empty Calorimeter

As at low temperatures, prior to measuring the heat capacity of the spinel samples, the heat capacity of the empty calorimeter, together with 26.2 mg of thermally conductive compound, was measured over the temperature range 30 - 300°K. The resultant heat capacity data relating to this empty calorimeter are given in Table 4.4.

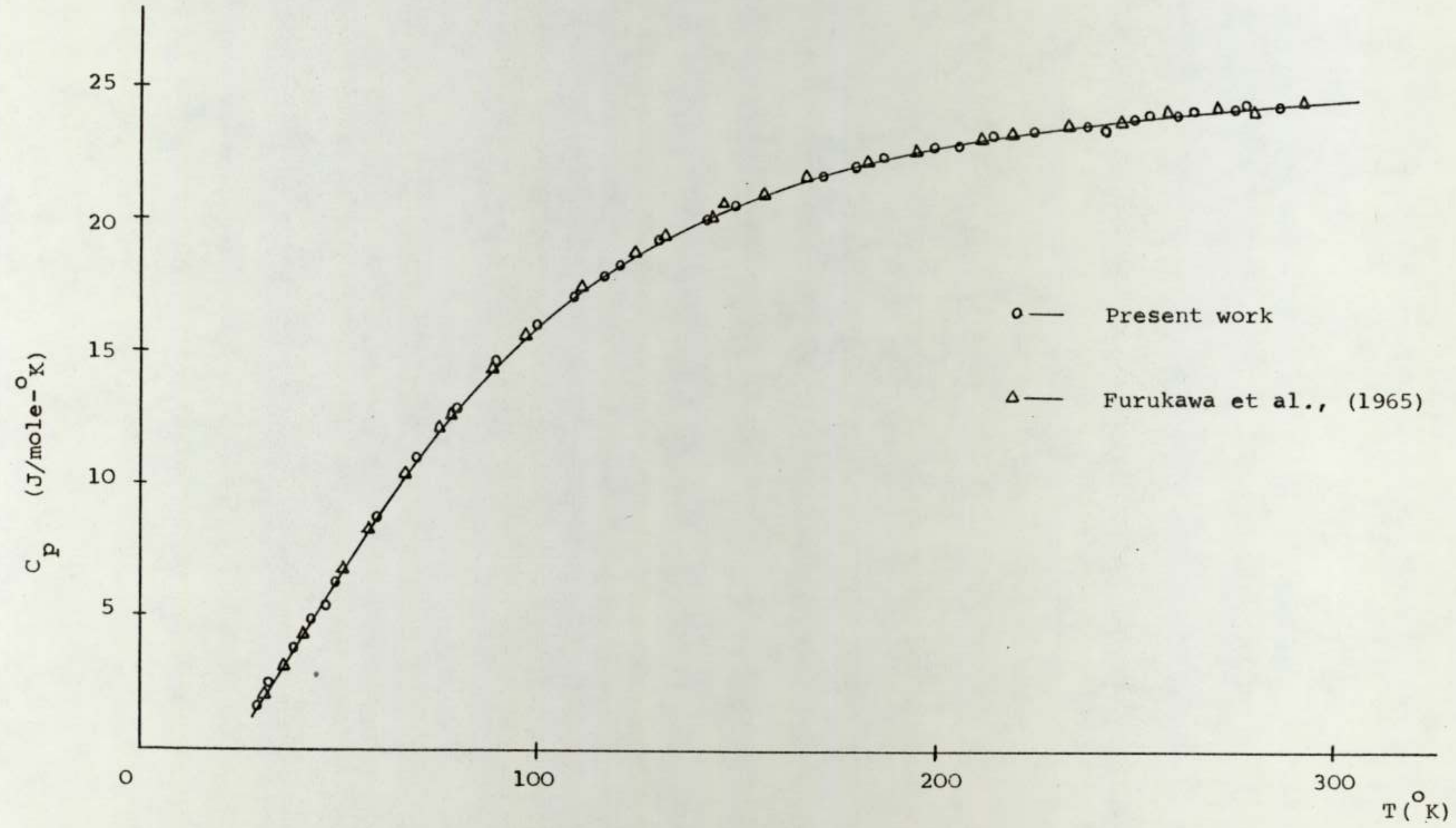

FIGURE 4.12 Heat capacity of copper.

TABLE 4.4

Heat Capacity of empty calorimeter together with 26.2 mg of thermally conductive compound

T ($^{\circ}$K)	C_p (J/$^{\circ}$K)	T ($^{\circ}$K)	C_p (J/$^{\circ}$K)	T ($^{\circ}$K)	C_p (J/$^{\circ}$K)
30.07	1.21	112.46	9.08	168.52	11.41
33.23	1.81	114.82	9.19	170.41	11.47
35.45	2.06	117.17	9.43	174.07	11.48
36.88	2.21	119.43	9.50	177.82	11.66
38.23	2.38	121.96	9.68	179.67	11.75
40.10	2.45	124.47	9.79	181.52	11.84
43.01	3.04	126.67	9.87	187.02	11.92
46.13	3.35	128.85	9.96	188.83	12.02
50.07	3.85	131.01	10.04	192.44	12.11
54.64	4.41	133.16	10.18	199.59	12.29
56.75	4.53	135.27	10.17	212.14	12.42
61.24	5.03	137.38	10.36	215.64	12.53
63.40	5.22	139.47	10.35	219.99	12.63
66.99	5.62	144.79	10.43	232.64	12.75
70.74	5.95	146.85	10.59	241.71	12.85
72.95	6.18	148.88	10.75	245.49	12.91
75.12	6.41	150.90	10.73	250.97	12.98
79.52	6.80	152.91	10.78	260.61	13.12
85.61	7.29	154.90	10.88	268.03	13.15
91.70	7.99	156.88	11.05	271.79	13.17
94.62	8.00	158.85	11.08	275.39	13.24
98.16	8.24	160.81	11.10	280.73	13.26
102.51	8.55	162.75	11.26	284.23	13.28
107.59	8.68	164.68	11.31	290.12	13.29
110.05	8.89	166.60	11.36	294.35	13.30
				296.15	13.31

4.3.4 (b) Results for $LiTi_2O_4$ over the Range 30 - 300°K

For heat capacity measurements involving $LiTi_2O_4$ spinel samples, the calorimeter was filled with 5.9435 gm of $LiTi_2O_4$, together with the same amount of thermally conductive compound used in the case of the empty calorimeter. The experimental values of the observed molar heat capacity of $LiTi_2O_4$ between 30 - 300°K are presented in Table 4.5. These data were obtained by subtracting the heat capacity of the empty calorimeter from the overall heat capacity of the calorimeter plus the $LiTi_2O_4$ sample. Values of the heat capacity of the empty calorimeter were taken from a large-scale graph of the observed experimental points in Table 4.4 fitted to their optimum smooth curve.

TABLE 4.5

The experimental values of the observed heat capacity of $LiTi_2O_4$ between 30 and 300°K

T (^{o}K)	C_p (J/mole-^{o}K)	T (^{o}K)	C_p (J/mole-^{o}K)
31.21	5.43	81.12	31.37
33.41	6.52	83.45	32.49
35.91	7.79	85.24	33.85
37.45	8.45	87.43	35.01
40.66	10.15	89.12	36.72
42.95	11.22	91.75	37.88
44.28	12.05	94.49	38.96
46.04	12.84	97.15	41.01
48.85	14.12	99.75	42.71
50.19	14.83	102.28	43.98
52.04	15.85	104.75	45.97
53.91	16.74	107.17	47.29
55.37	17.30	111.87	51.05
59.50	19.57	114.16	52.57
62.16	21.22	116.41	53.73
64.72	22.36	118.62	56.18
67.57	24.22	120.80	57.85
69.12	24.81	122.96	58.97
72.25	26.61	125.08	60.14
75.49	27.92	127.19	61.96
78.43	29.95	129.26	63.69

TABLE 4.5 (continued)

T (^oK)	C_p (J/mole-^oK)	T (^oK)	C_p (J/mole-^oK)
131.32	64.63	200.85	116.2
133.35	66.37	208.37	122.3
135.35	67.57	212.21	122.8
137.34	70.25	214.11	124.9
139.31	71.97	215.99	126.9
141.52	72.51	225.33	131.4
143.18	74.02	234.71	136.4
148.87	77.78	240.33	138.6
150.75	80.05	243.57	137.9
152.61	81.11	247.06	142.2
154.45	83.33	250.54	142.4
158.09	86.06	252.26	142.7
161.70	87.21	253.98	143.9
163.48	90.25	260.75	145.6
167.02	91.29	264.11	145.9
170.53	94.70	267.43	147.3
173.94	96.80	269.07	148.2
175.65	97.26	270.71	149.2
179.03	101.2	275.57	150.4
182.59	102.7	280.41	152.9
184.67	104.9	286.00	154.3
186.74	106.6	290.12	154.7
190.82	108.5	295.60	158.6
196.88	113.8	297.45	159.1

4.3.4 (c) Results for $CuRh_2Se_4$ over the Range 30 - 300°K

The weight of $CuRh_2Se_4$ sample used for heat capacity measurements was 11.4576 gm. The values of its observed molar heat capacity over the temperature range 30 - 300°K are given in Table 4.6.

TABLE 4.6

The experimental values of the observed heat capacity of $CuRh_2Se_4$ between 30 and 300°K

T (°K)	C_p (J/mole-°K)	T (°K)	C_p (J/mole-°K)
32.22	18.85	88.59	112.8
34.39	21.20	90.23	115.9
36.31	23.13	93.45	119.5
38.04	25.33	95.03	120.5
40.19	28.14	96.56	122.1
42.19	31.16	98.14	123.6
45.58	37.49	101.19	125.6
47.39	40.66	102.68	128.2
50.79	47.65	104.16	129.2
53.52	52.61	105.62	130.8
56.40	58.22	108.51	133.3
58.90	64.35	109.94	134.3
63.41	74.06	112.70	136.4
66.47	79.68	115.44	139.4
68.23	82.23	119.60	142.0
73.07	91.94	122.62	145.6
76.18	96.02	125.25	146.6
81.54	103.7	127.84	149.6
85.29	107.8	130.41	150.2

TABLE 4.6 (Continued)

T (^oK)	C_p (J/mole-^oK)	T (^oK)	C_p (J/mole-^oK)
132.63	152.2	199.57	189.0
135.19	155.8	208.54	191.0
138.15	155.8	212.97	192.0
140.67	157.8	217.39	195.1
144.37	160.9	220.32	196.1
149.25	162.4	227.57	198.2
150.15	163.0	230.45	200.7
154.95	164.5	234.69	201.2
160.62	168.0	243.11	202.3
163.84	172.6	250.32	203.3
167.04	174.2	255.25	204.8
170.59	174.7	259.31	206.9
172.14	176.7	264.72	210.4
175.19	177.2	270.69	210.9
177.69	178.8	274.60	212.0
180.72	179.3	279.71	212.5
185.37	180.8	282.25	213.0
190.42	184.9	286.45	213.5
193.48	186.4	292.75	215.0
196.04	188.5	297.86	216.6

4.4 Summary of Smoothed Heat Capacity Results

The heat capacity results arising from this investigation are now summarized in this section, over the temperature range studied, in the form of smoothed data. This data was derived from the corresponding large-scale graphs of the experimental values of the observed molar heat capacity relating to each sample studied (see Sections 4.2.5 and 4.3.4) after fitting to their optimum smooth curves.

4.4.1 Smoothed Molar Heat Capacity Data for $LiTi_2O_4$

The smoothed molar heat capacity data for $LiTi_2O_4$ over the temperature range 4.2 - 300°K are presented in Table 4.7, whilst Figures 4.13 - 4.14 show the actual plot of heat capacity at constant pressure, C_p, as a function of T. The analysis of these results, corrected to constant volume, C_v, is given in the following chapter. The values for C_v were derived from the corresponding figures for C_p through the Nernst-Lindemann equation (Section 2.1) where, in the case of $LiTi_2O_4$, $3\alpha = 2.6 \times 10^{-5}$ degree^{-1} (Cheary, private communication) and $V = 44.75$ cm^3/mole, since the lattice constant at room temperature is 8.408Å. For oxide spinels, the bulk modulus tends to take values ~ 20×10^{10} N/m^2 and this was assumed to be appropriate for $LiTi_2O_4$.

TABLE 4.7

Smoothed Heat Capacity Data for $LiTi_2O_4$

T (^oK)	C_p (J/mole-^oK)	C_v (J/mole-^oK)	T (^oK)	C_p (J/mole-^oK)	C_v (J/mole-^oK)
4.5	0.0392	0.0392	80	30.65	30.63
5.0	0.0591	0.0591	90	36.79	36.76
6.0	0.109	0.109	100	42.91	42.87
7.0	0.182	0.182	110	49.55	49.49
8.0	0.255	0.255	120	56.75	56.66
9.0	0.350	0.350	130	64.24	64.11
10.0	0.452	0.452	140	71.65	71.48
12.0	0.730	0.730	150	79.21	78.98
12.15	0.729	0.729	160	86.81	86.52
12.50	0.550	0.550	170	94.42	94.06
12.75	0.415	0.415	180	101.5	101.1
13	0.431	0.431	190	108.9	108.4
14	0.496	0.496	200	116.1	115.5
16	0.624	0.624	210	122.4	121.7
18	0.780	0.780	220	127.4	126.5
20	1.08	1.08	230	133.0	132.0
25	2.55	2.55	240	137.7	136.6
30	4.80	4.80	250	141.8	140.5
35	7.30	7.30	260	145.4	144.1
40	9.75	9.75	270	149.1	147.6
45	12.24	12.24	280	153.1	151.2
50	14.72	14.72	290	155.5	153.8
60	19.85	19.84	300	158.6	156.8
70	25.24	25.23			

4.4.2 Smoothed Molar Heat Capacity Data for $CuRh_2Se_4$

Corresponding smoothed molar heat capacity data for $CuRh_2Se_4$ are presented in Table 4.8 and Figures 4.13 - 4.14 over the temperature range 1.5 - 300°K. As before, the constant volume heat capacity, C_v, is also given, following correction of the C_p values using the Nernst-Lindemann equation.

For $CuRh_2Se_4$, α was unknown, but assumed to be similar to $CdCr_2Se_4$, i.e., 7.5×10^{-6} $degree^{-1}$ after Bindloss (1971), $V = 81.34$ cm^3/mole corresponding to a lattice constant at room temperature of 10.260Å (Dawes and Grimes, 1975), and, again, the bulk modulus was assumed to be ~ $20 \times 10^{10} N/m^2$.

TABLE 4.8

Smoothed Heat Capacity Data for $CuRh_2Se_4$

T (°K)	C_p (J/mole-°K)	C_v (J/mole-°K)	T (°K)	C_p (J/mole-°K)	C_v (J/mole-°K)
1.6	0.0325	0.0325	80	101.6	101.5
2.0	0.0633	0.0633	90	114.3	114.1
2.5	0.118	0.118	100	125.3	124.9
3.0	0.190	0.190	110	135.0	134.7
3.4	0.260	0.260	120	142.8	142.3
3.43	0.259	0.259	130	150.3	149.7
3.50	0.190	0.190	140	156.8	156.2
3.55	0.153	0.153	150	163.1	162.4
3.80	0.174	0.174	160	169.0	168.2
4	0.190	0.190	170	174.5	173.6
5	0.284	0.284	180	179.8	178.7
6	0.392	0.392	190	184.7	183.5
8	0.820	0.820	200	189.3	188.0
10	1.30	1.30	210	192.9	191.5
15	3.36	3.36	220	196.3	194.8
20	6.35	6.35	230	199.3	197.7
25	10.25	10.25	240	202.0	200.3
30	15.26	15.26	250	204.5	202.7
35	21.45	21.45	260	207.8	205.8
40	28.54	28.53	270	210.5	208.4
45	37.25	37.24	280	212.9	210.7
50	46.15	46.13	290	215.0	212.7
60	66.39	66.34	300	216.8	214.4
70	85.90	85.81			

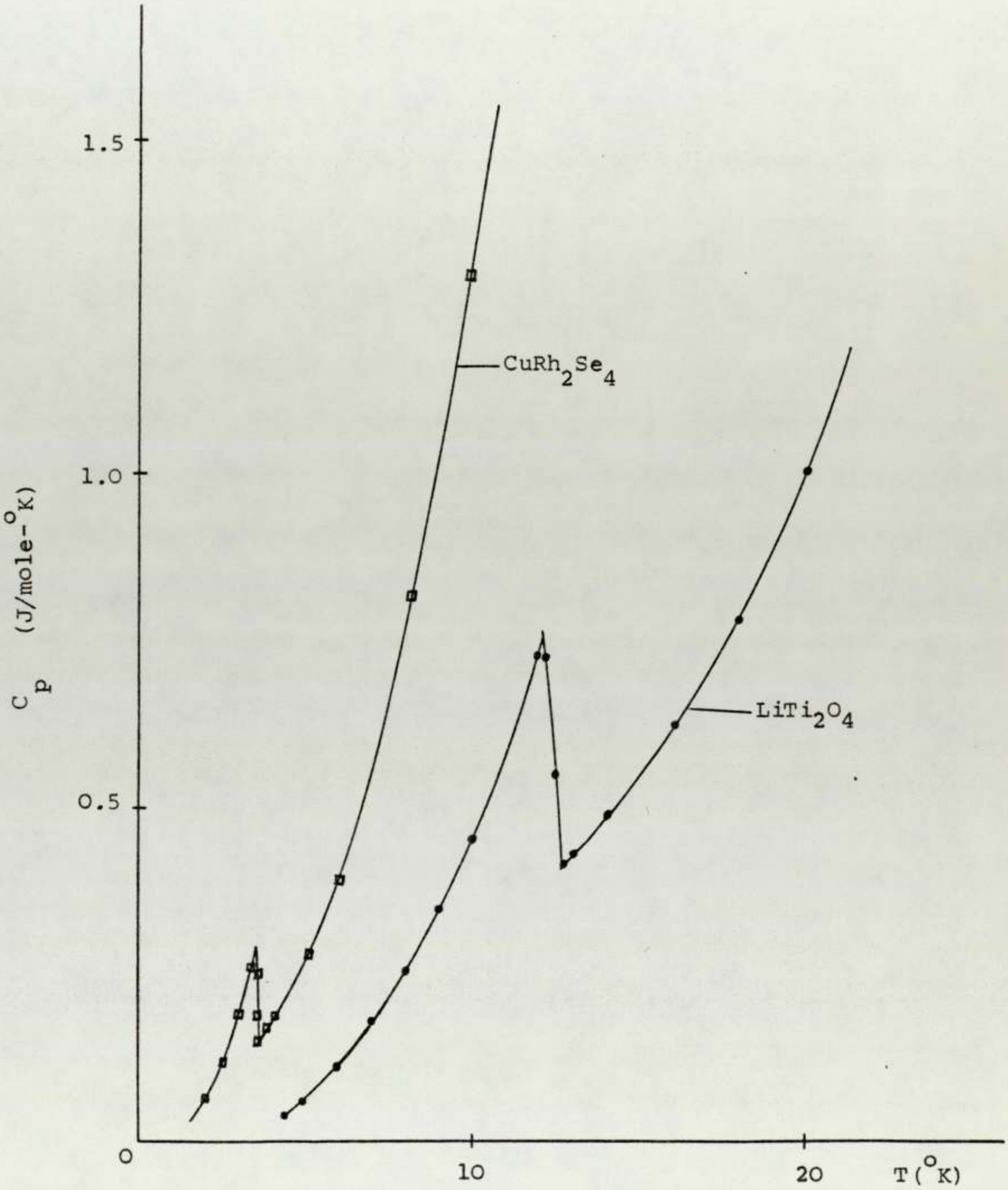

FIGURE 4.13 Smoothed heat capacity of $LiTi_2O_4$ and $CuRh_2Se_4$ at low temperatures.

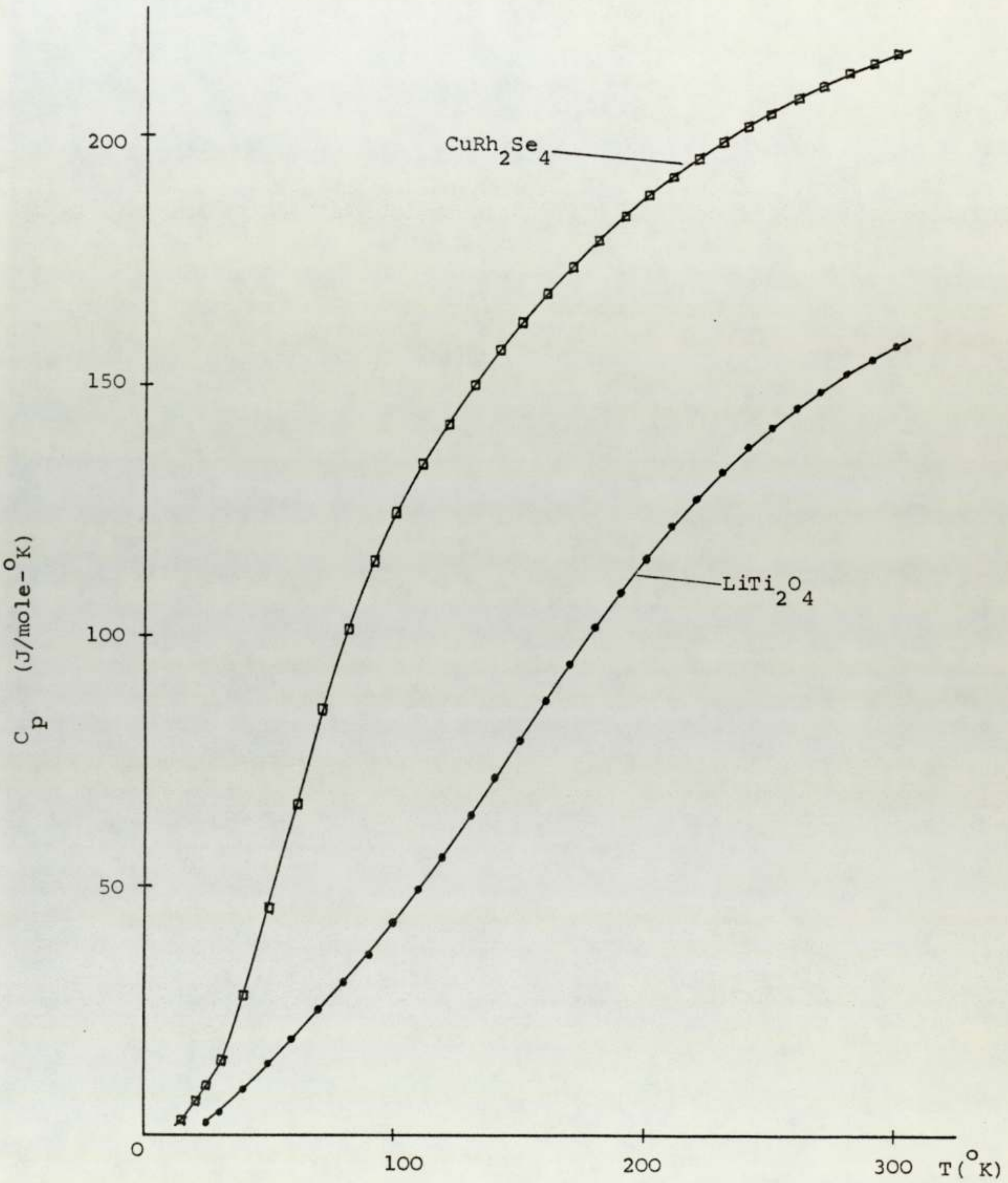

FIGURE 4.14 Smoothed heat capacity of $LiTi_2O_4$ and $CuRh_2Se_4$ between 30 and 300°K.

CHAPTER 5

ANALYSIS AND DISCUSSION

CHAPTER 5

ANALYSIS AND DISCUSSION

5.1 Superconducting Transition Temperatures

As has been emphasized by many workers, the highest and sharpest transition temperatures, T_c, among different samples of a given superconducting compound, tend to be exhibited by those which are single phased and of good stoichiometry. In the case of the spinel samples used in this investigation T_c was determined both by resistivity (see Section 4.1) and heat capacity measurements (see Section 4.2.5). These results are summarized for $LiTi_2O_4$ and $CuRh_2Se_4$ in Table 5.1 and it should be noticed that the T_c values obtained from the two methods are in good agreement.

A comparison of these values with those reported by previous workers for the same spinel compounds is shown in Table 5.2 where it will be observed that there is very good agreement among the results for $CuRh_2Se_4$. In the case of $LiTi_2O_4$, however, much wider variations have been reported and this is presumably associated with the difficulties experienced in preparing this compound. Nevertheless, by the criterion of T_c measurement, it is evident that the samples used in the present investigations are at least comparable with, if not better than, the best material that has been prepared to date.

TABLE 5.1

Comparison of transition temperatures, T_c, obtained from resistivity measurements and specific heat measurements.

Compounds	Resistivity results		Specific heat results	
	T_c (°K) $\pm$ 0.05	ΔT_c (°K) $\pm$ 0.05	T_c (°K) $\pm$ 0.05	ΔT_c (°K) $\pm$ 0.05
$LiTi_2O_4$	12.35	0.50	12.40	0.46
$CuRh_2Se_4$	3.48	0.20	3.50	0.11

TABLE 5.2

Reported transition temperatures, T_c, for spinel compounds.

Compounds	% Impurity phases	T_c (^oK)	ΔT_c (^oK)	References
$LiTi_2O_4$	0	12.40	0.46	Present work
	~ 20	10.95 (onset T_c = 13.7^{o}K)	4.2	Johnston et al. (1973)
	~ 10	11.2	> 0.1	Shelton et al. (1976)
	~ 15	11.26	0.04	
	-	11.7	1.2	McCallum et al. (1976)
	-	10-12	-	Johnston (1976)
$CuRh_2Se_4$	0	3.50	0.11	Present work
	0	3.47	0.04	Van Maaren et al. (1967)
	0	3.46	0.09	Robbins et al. (1967)
	0	3.50	0.50	Dawes and Grimes (1975)
	-	3.48	-	Schaeffer et al. (1968)
	~ 15	3.49	0.02	Shelton et al. (1976)
	0	3.38	0.01	

5.2 Analysis of Low Temperature Heat Capacity Data

5.2.1 Heat Capacity Coefficients

As emphasized in Chapter 2, to extract the anharmonic component from heat capacity data, the low temperature electronic coefficient, γ_o, must be carefully determined. Therefore, the method of analysis described by Knapp et al. was followed closely, that is, the values of γ_o, β, D and θ_o were obtained by fitting the experimental data to the 3-term expansion of equation (2.11), utilizing the additional constraint that normal state and superconducting state entropies are equal at T_c. Thus, we have that:

$$C_n(T_c)/T_c = \gamma_o + \beta T_c^2 + DT_c^4 \quad \text{......} \; (5.1)$$

and

$$S_n(T_c) = S_s(T_c) \quad \text{......} \; (5.2)$$

Here,

$$S_n(T_c) = \int_o^{T_c} (\gamma_o + \beta T^2 + DT^4)\,dT$$

$$= \gamma_o T_c + \frac{1}{3}\beta T_c^3 + \frac{1}{5} DT_c^5 \quad \text{......} \; (5.3)$$

The entropy $S_s(T_c)$ was determined by numerically integrating the area under the plot of C_p/T versus T up to the onset - T_c temperature for superconductivity.

The results obtained from this analysis of the low temperature heat capacity data from $LiTi_2O_4$ and $CuRh_2Se_4$ are summarized in Table 5.3 which also shows the corresponding values obtained by previous workers. Note, however, that in previous work the lattice contribution has always been assumed to be adequately characterized by a single term proportional to T^3.

TABLE 5.3

Various normal state parameters obtained from the low-temperature analysis of the heat capacity results. Comparison between the values obtained from this and earlier work.

Compounds	γ_o (mJ/mole-$^oK^2$)	β (mJ/mole-$^oK^4$)	D (mJ/mole-$^oK^6$)	θ_o (^oK)	References
$LiTi_2O_4$	21.5 ± 0.3	0.075 ± 0.002	$- 2.00 \times 10^{-5}$	567 ± 6	Present work
$LiTi_2O_{3.95}$	21.4	0.043	-	685	McCallum et al. (1976)
$Li_{1.05}Ti_{1.94}O_4$	19.7	0.054	-	630	
$CuRh_2Se_4$	24.9 ± 0.5	1.55 ± 0.05	$- 5.18 \times 10^{-3}$	206 ± 3	Present work
	27.0	1.32	-	218	Schaeffer et al. (1968)

Some idea of the significance of the values obtained for the electronic coefficient γ_o is given by Table 5.4 where the ratios $C_E\ (T_c)/\gamma_o T_c$ are compared with the prediction from the Bardeen-Cooper-Schrieffer (BCS) theory of superconductivity (see, for instance, Lynton, 1967).

5.2.2 Thermodynamic Critical Fields

The critical field for a superconductor is one of the more important practical parameters and can be calculated from heat capacity data from the entropy difference of the normal and superconducting states (London, 1950). The essential equations are:

$$S_n(T) - S_s(T) = -\frac{VH_c}{4\pi}\frac{dH_c}{dT} = -\frac{V}{8\pi}\frac{d(H_c^2)}{dT} \qquad \ldots\ldots (5.4)$$

i.e.,

$$H_c(T)^2 = -\frac{8\pi}{V}\int_{T_c}^{T} (S_n - S_s)\,dT' \qquad \ldots\ldots (5.5)$$

and

$$(S_n - S_s)T'' = \int_{o}^{T''} \{ (C_n - C_s)/T'' \}\, dT'' \qquad \ldots\ldots (5.6)$$

where in the present work the entropy difference between the normal and superconducting states was obtained by graphically integrating $C_n/T - C_s/(T)$ (shown in Figures 5.1(a) and 5.2(a) for $LiTi_2O_4$ and $CuRh_2Se_4$ respectively) according to equation (5.6). Integrating this entropy difference then yields the temperature-dependent thermodynamic critical field, $H_c(T)$.

Figures 5.1(b) and 5.2(b) show the plot of $H_c(T)$ versus $(T/T_c)^2$ for $LiTi_2O_4$ and $CuRh_2Se_4$ respectively. Below about 10^oK ($LiTi_2O_4$) and $2\ ^oK$ ($CuRh_2Se_4$) the data are well described by the relation:

$$H_c(T) = H_c(0)\ \{ 1 - b\ (T/T_c)^2 \} \qquad \ldots\ldots (5.7)$$

TABLE 5.4

Comparison with BCS theory

Compounds	$C_E\ (T_c)/\gamma_o T_c$
$LiTi_2O_4$	2.49
$CuRh_2Se_4$	2.42 (2.44)*
BCS prediction	2.43

* = Schaeffer et al. (1968)

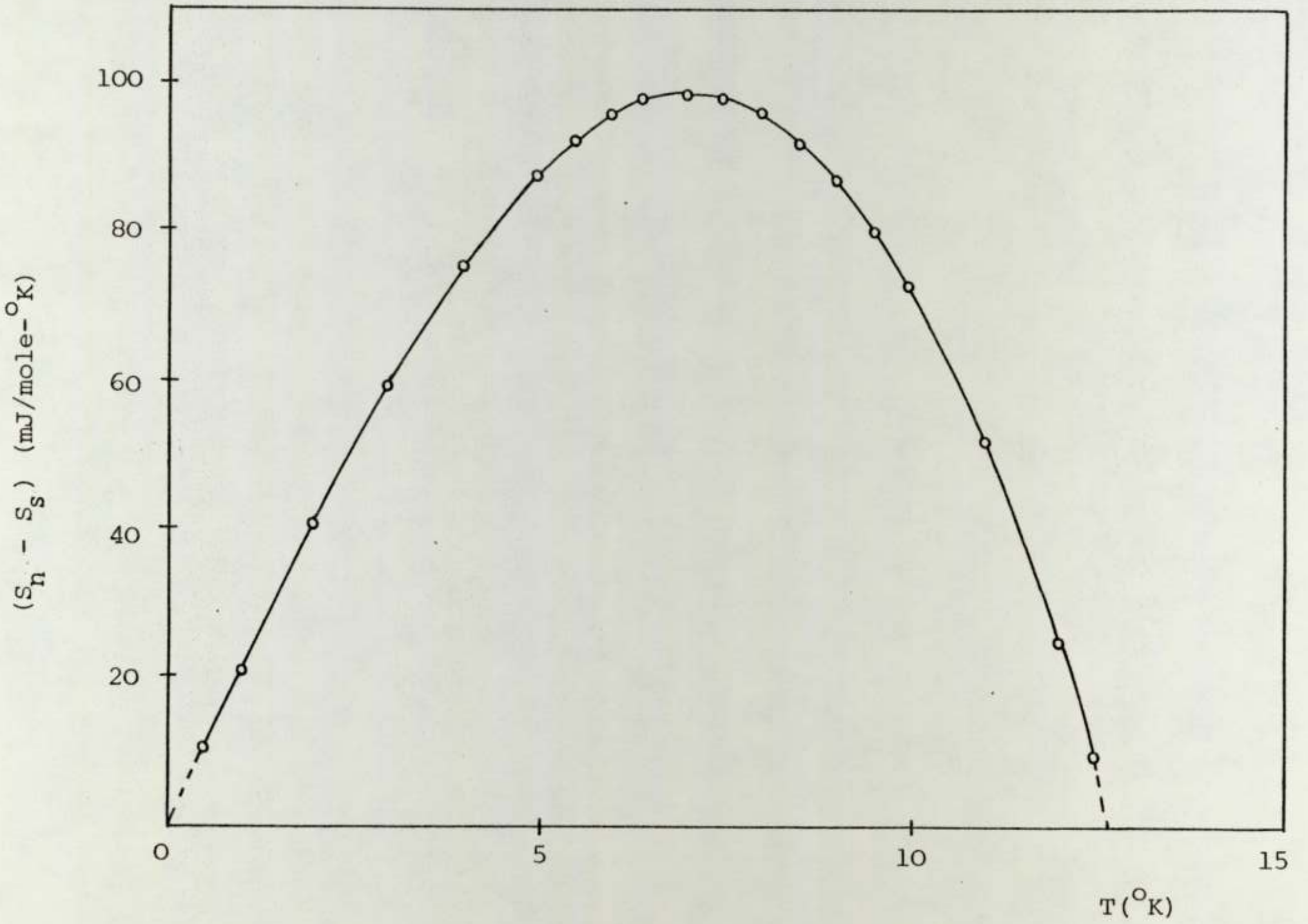

FIGURE 5.1(a) Entropy difference between normal and superconducting states for $LiTi_2O_4$ up to T_c.

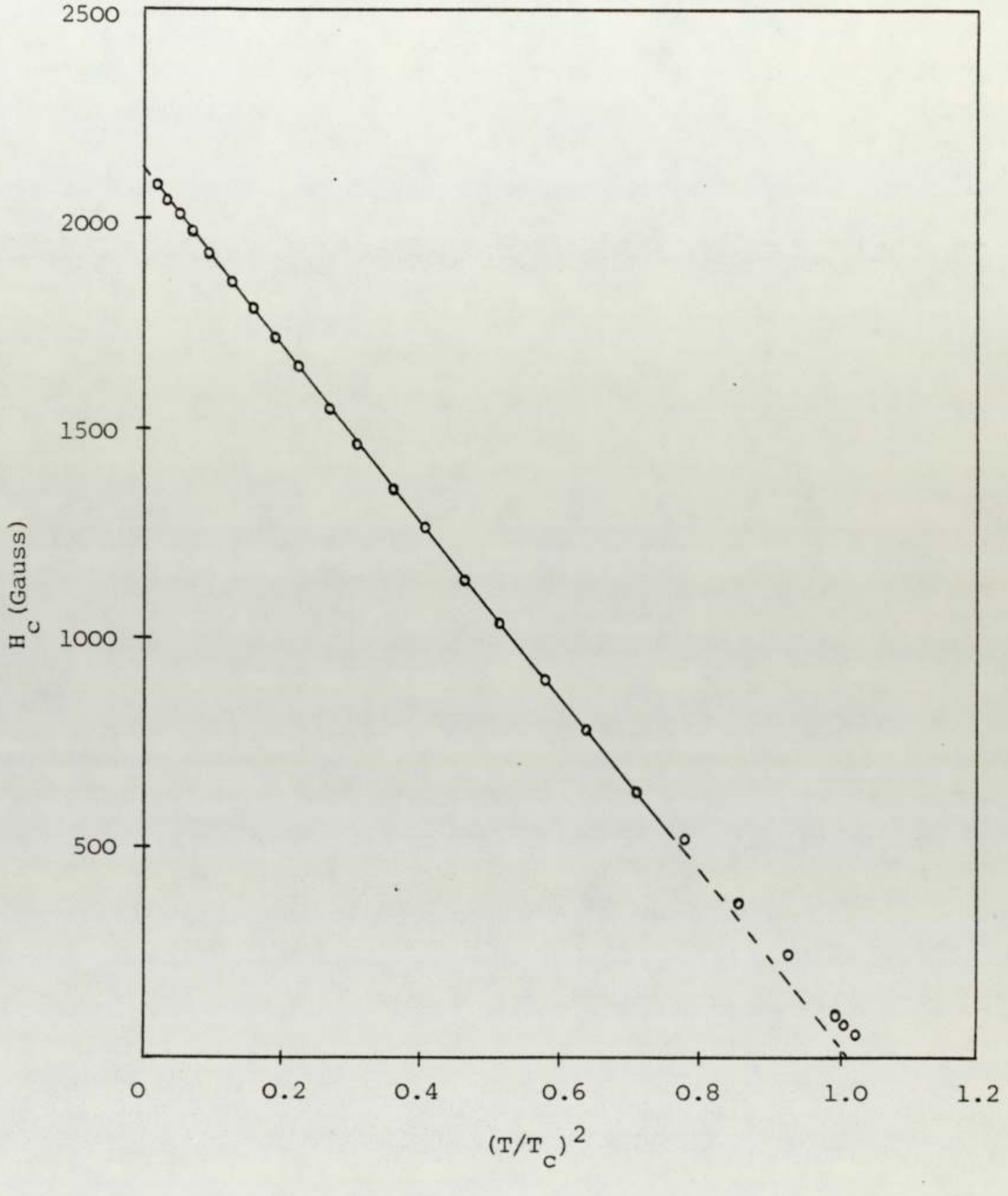

FIGURE 5.1(b) Thermodynamic critical field, $H_c(T)$, obtained by integrating the heat capacity data of Figure 5.1(a), plotted versus the square of the reduced temperature for $LiTi_2O_4$.

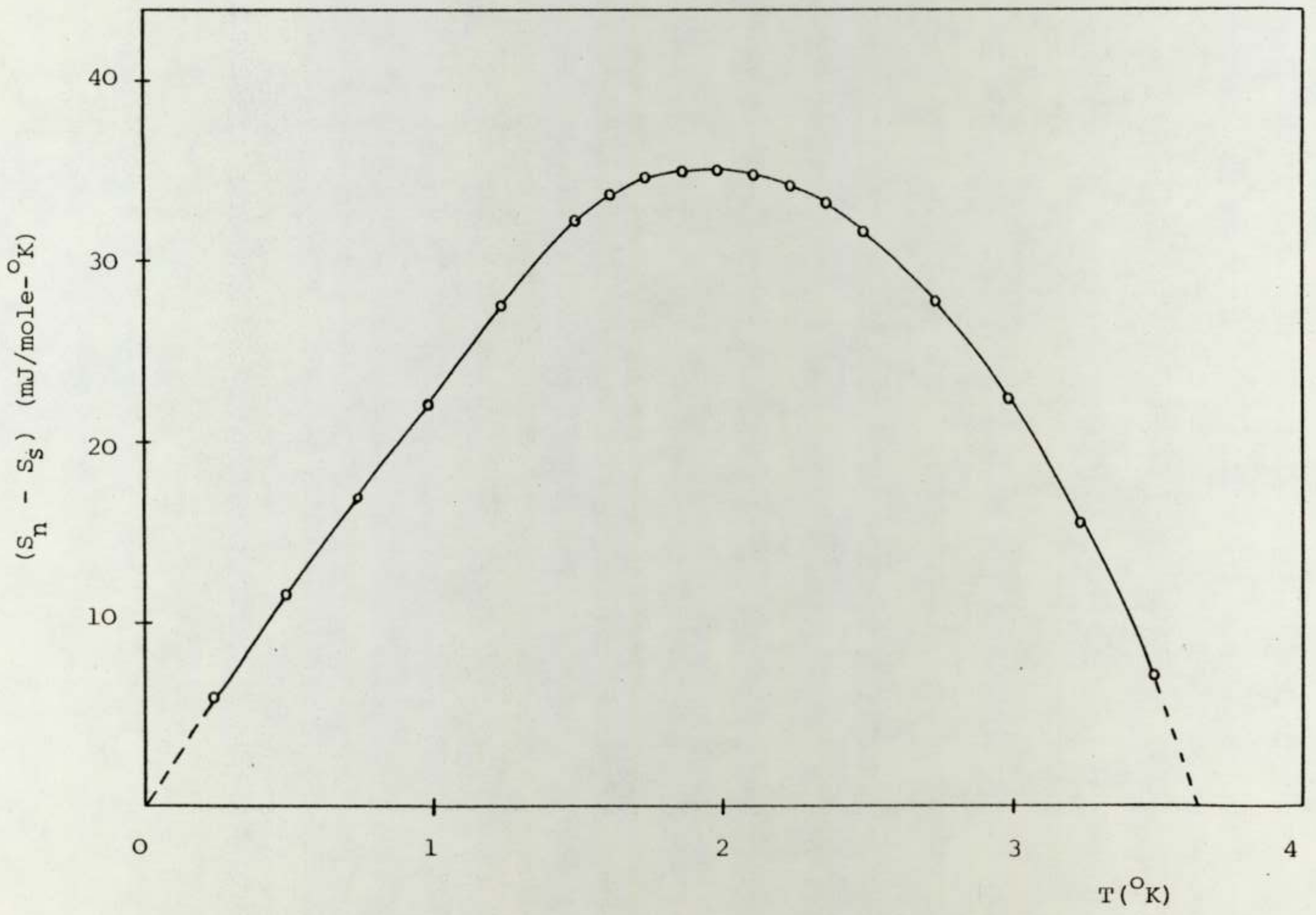

FIGURE 5.2(a) Entropy difference between normal and superconducting states for $CuRh_2Se_4$.

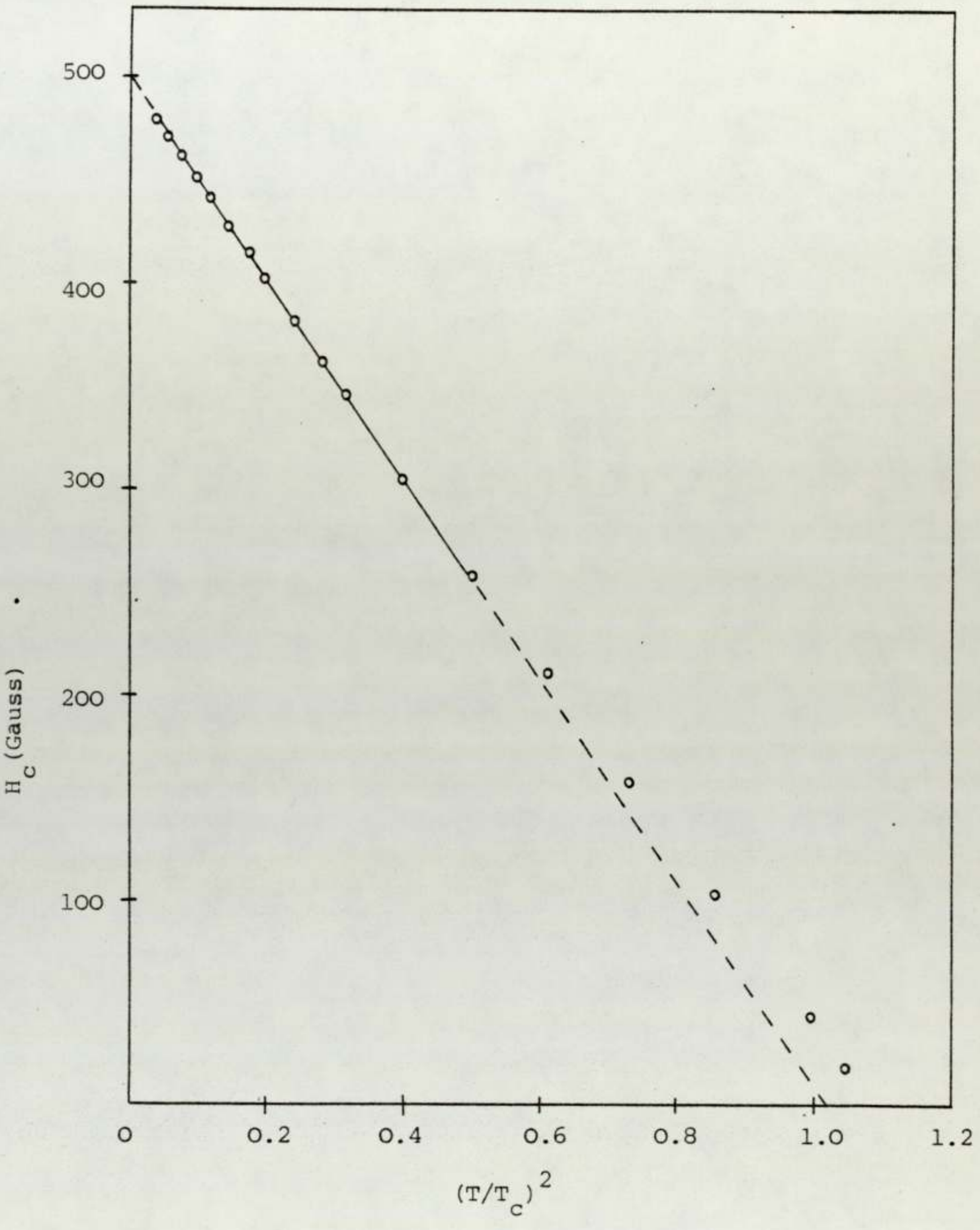

FIGURE 5.2(b) Thermodynamic critical field, $H_c(T)$, obtained by integrating the heat capacity data of Figure 5.2(a), plotted versus the square of the reduced temperature for $CuRh_2Se_4$.

with $H_c(0) = 2130$ Gauss and $b = 0.95$ for $LiTi_2O_4$ and $H_c(0) = 500$ Gauss and $b = 0.87$ in the case of $CuRh_2Se_4$. For $T << T_c$, the BCS theory predicts:

$$H_c(T) = H_c(0)\ \{\ 1 - 1.07(T/T_c)^2\ \} \qquad \text{...... (5.8)}$$

with $$H_c(0) = (10^4 \gamma_o T_c^2 / 0.170V)^{\frac{1}{2}} \qquad \text{...... (5.9)}$$

where V is the molar volume (see Sections 4.4.1 and 4.4.2). Using the γ_o values given in Table 5.3, for both samples under consideration equation (5.9), the values obtained are shown below:

Compounds	$H_c(0)$ expt. (Gauss)	$H_c(0)$ BCS (Gauss)
$LiTi_2O_4$	2130	2086
$CuRh_2Se_4$	500	470

5.3 Analysis of High Temperature Heat Capacity Data

5.3.1 The High Temperature Parameters

In the method of analysis followed here, the detection of anharmonic contributions to the heat capacity is attempted in the high temperature region as described in Chapter 2. But first, equation (2.18) is re-written to allow for the 7 atoms per molecule characteristic of the spinel compounds. That is, we write:

$$\frac{C_v - 21R}{T} = 7(\gamma + A) - \frac{21}{20} R \frac{\theta_\infty^2}{T^3} \qquad \text{...... (5.10)}$$

where the anharmonic contribution

$$A = -k_B \sum_{s=1}^{3N} \frac{\omega'_s}{\omega_s} , \qquad \text{...... (5.11)}$$

and $$\theta_\infty = \left(\frac{5}{3} \frac{\hbar^2 < \omega_s^2 >}{k_B^2}\right)^{\frac{1}{2}} \qquad \text{...... (5.12)}$$

is a characteristic temperature for the high temperature region, and we look for a linear behaviour in a graph of $(C_v - 21R)/T$ versus T^{-3}.

Figure 5.3 shows the result obtained from plotting this graph using the high temperature heat capacity data from $LiTi_2O_4$ and $CuRh_2Se_4$. In both cases the linearity is good but there is a striking difference in the slope and intercept for the two materials; $LiTi_2O_4$ the higher T_c material, having an appreciably less positive intercept, i.e., less positive value for $(A + \gamma)$.

The values derived for the high temperature parameters θ_∞, $< \omega_s^2 >$ and $(A + \gamma)$, from the slopes and intercepts of Figure 5.3 are collected in Table 5.5 together with their estimated experimental uncertainties.

5.3.2 The Electronic Heat Capacity Coefficient at High Temperatures

As explained in Section 2.3, the major problem in interpreting high temperature heat capacity data is the separation of the electronic and anharmonic contributions. In order to separate $(A + \gamma)$ we have to have γ for the high temperature region whereas low temperature analysis only gives γ_o, i.e., the electronic heat capacity coefficient including the effects of electron-phonon coupling enhancement. It has been shown by Grimvall (1968), that the latter has effectively vanished above a temperature of $2\theta_D$, and therefore that at a high temperature the appropriate value of γ is given by γ_b, the band structure electronic heat capacity coefficient for that temperature. Thus, it is the

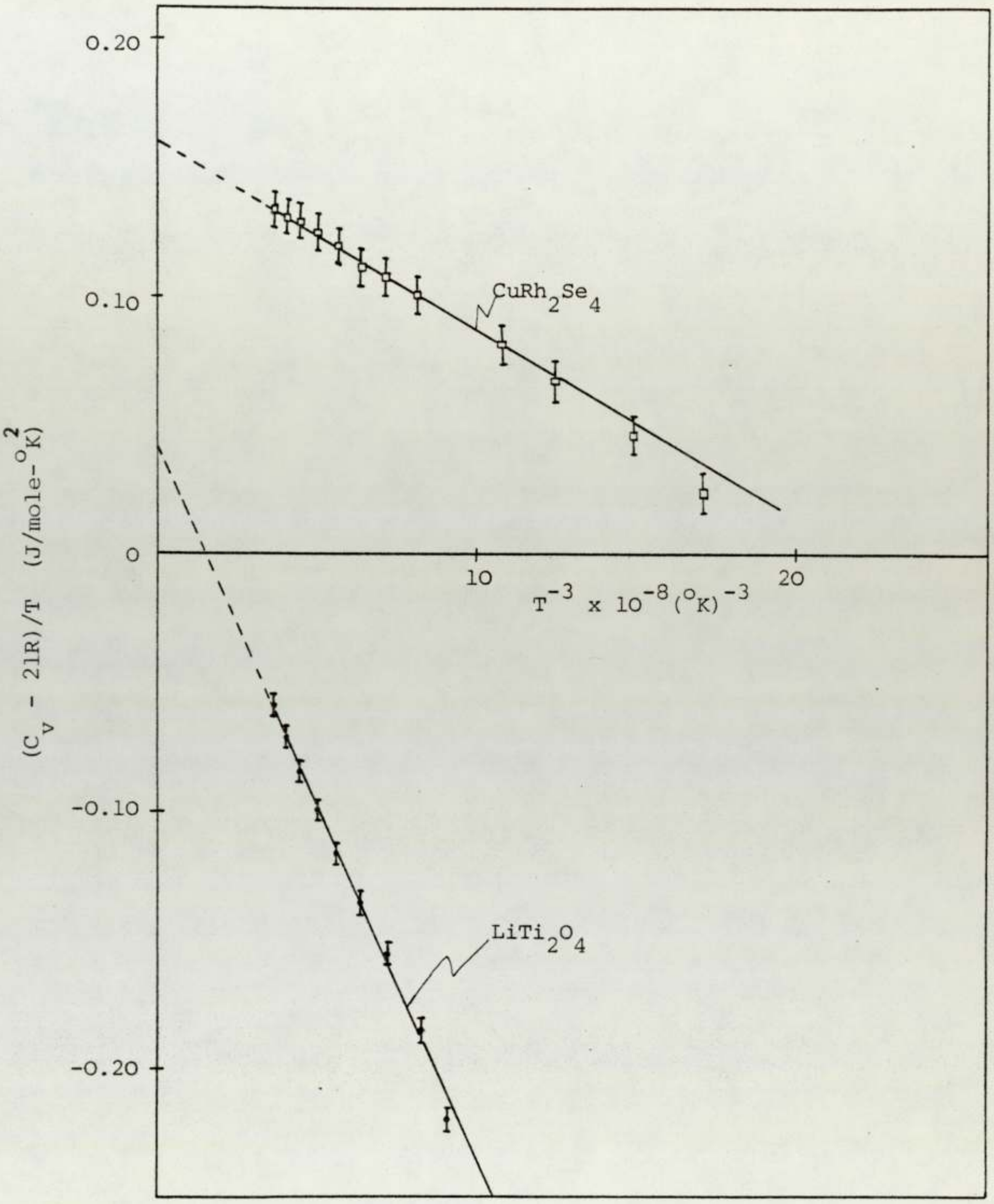

FIGURE 5.3 Heat capacity of spinel compounds, $LiTi_2O_4$ and $CuRh_2Se_4$, plotted as $(C_v - 21R)/T$ vs T^{-3}.

TABLE 5.5

Some parameters found in the high-temperature analysis of the heat capacity data.

Compounds	θ_∞ (^oK)	$<\omega_s^2>$ (sec^{-2})	A + γ ($mJ/mole\text{-}^oK^2$)
$LiTi_2O_4$	566 ± 6	3.29 ± 0.07 x 10^{27}	6.0 ± 0.5
$CuRh_2Se_4$	284 ± 10	8.3 ± 0.6 x 10^{26}	22.8 ± 0.7

temperature dependence of γ_b which then has to be determined.

At low temperatures $\gamma_b^{(0)}$ is given by:

$$\gamma_b^{(0)} = \gamma_o/(1 + \lambda) \qquad \text{......} \quad (5.13)$$

and can be derived immediately if the value of the electron-phonon coupling constant λ is known. Following Knapp, λ is calculated from McMillan's equation:

$$\lambda = \frac{1.04 + \mu^* \ln(\theta/1.45T_c)}{(1 - 0.62\mu^*)\ln(\theta/1.45T_c) - 1.04} \qquad \text{......} \quad (5.14)$$

where θ is taken to be θ_∞ and, for spinels, $\mu^* = 0.13$ (van Maaren et al., 1970).

In the case of the A15 compounds investigated by Knapp the temperature dependence of γ was assumed to have the form:

$$\gamma = \frac{\gamma_b}{1 + T/\phi} \qquad \text{......} \quad (5.15)$$

since such a variation was consistent with the known temperature dependence of the corresponding magnetic susceptibilities and spin-lattice relaxation times which, like γ, also depend on the electronic density of states, $N(\varepsilon)$. This kind of experimental data has not yet been reported for $LiTi_2O_4$ and $CuRh_2Se_4$, however, and therefore, in the present work, it seemed best to assume the nearly free electron approximation, according to which (see, for instance, A. H. Wilson, 1953 and the appendix to this thesis),

$$\gamma = \gamma_b \left\{ 1 - \frac{3\pi^2}{10} \left(\frac{k_B T}{\varepsilon_F}\right)^2 - \text{......} \right\} \qquad \text{......} \quad (5.16)$$

where ε_F is the Fermi energy.

In the case of $LiTi_2O_4$, ε_F was derived from the expression:

$$\varepsilon_F = \left\{ \frac{N(\varepsilon_F)h^3}{4\pi V(2m^*)^{3/2}} \right\}^{\frac{1}{2}} \qquad \text{...... (5.17)}$$

using $m^* = 9.4m$ (Johnston, 1976). However, for $CuRh_2Se_4$, the value of ε_F was taken directly from Schaeffer et al. (1968) since m^* has not been reported. In both spinels $N(\varepsilon_F)$, the density of states for both spin directions at the Fermi level, was obtained from:

$$N(\varepsilon_F) = \frac{3\gamma_o}{\pi^2 k_B^{\,2}(1 + \lambda)} \qquad \text{...... (5.18)}$$

The values of λ, γ_o, $N(\varepsilon_F)$ and ε_F found for $CuRh_2Se_4$ and $LiTi_2O_4$ from this analysis are then as shown in Table 5.6(a) while γ_b, γ (at 300^oK), A and γ + A are given in Table 5.6(b).

5.3.3 Estimation of the McMillan-Hopfield η parameter

Having arrived at an estimate for the anharmonicity present in a superconducting material, it is a natural step to wish to relate this quantity to the other microscopic parameters and to the observed transition temperature. A plausible argument to provide this connection is given by Knapp et al. who derive an expression for the electron-phonon coupling constant in the form:

$$\lambda = \frac{\eta}{M<\omega_s^2>} - \frac{A}{9Nk_B^{\,2}N(\varepsilon_F)} \qquad \text{...... (5.19)}$$

where the second term is a correction for the presence of anharmonicity. The first term was originally obtained by McMillan who also showed that for a number of metals and alloys the electronic parameter:

$$\eta = N(\varepsilon_F) < I^2 > \qquad \text{...... (5.20)}$$

only varies very slowly and therefore that for these materials the

TABLE 5.6(a)

Electronic parameters for $LiTi_2O_4$ and $CuRh_2Se_4$

Compounds	λ	γ_o (mJ/mole-$^oK^2$)	$N(\varepsilon_F)$ ($eV^{-1}molecule^{-1}$)	ε_F (eV)	m*/m
$LiTi_2O_4$	0.70	21.5 ± 0.3	5.37	0.14	9.4
$CuRh_2Se_4$	0.59	24.9 ± 0.5	6.64	0.11	7.8†

† In the case of $CuRh_2Se_4$ m* is the value obtained from equation (5.17) using ε_F from Schaeffer et al. (1968).

TABLE 5.6(b)

Various parameters found in the high-temperature analysis of the heat capacity data. The units of γ_b, γ and A are in mJ/mole-$^oK^2$.

Compounds	γ_b	γ (300^{o}K)	A	γ + A
$LiTi_2O_4$	12.7 ± 0.2	11.3 ± 0.2	- 5.3 ± 0.3	6.0 ± 0.5
$CuRh_2Se_4$	15.7 ± 0.3	13.2 ± 0.3	9.6 ± 0.4	22.8 ± 0.7

electron-phonon coupling depends primarily upon the phonon frequencies rather than electronic properties.

More recently, and in apparent contradiction to this conclusion, Allen and Dynes (1975) have argued that although η may vary only slowly within a given class of superconducting materials, this variation is, in fact, more significant for the appearance of a high transition temperature than the changes which may simultaneously occur in the phonon frequencies.

Unfortunately, η is experimentally a rather inaccessible parameter and, indeed, is only known rather inaccurately at the present time, for a comparatively few superconducting materials. It can be derived quite directly from measurements of the Mössbauer 'S' parameter under certain assumptions (Taylor and Craig, 1968; Kimball, Taneja, Weber and Fradin, 1974) and some initial investigations of this kind were carried out by Dawes (1975) for the spinel series $CuRh_{2-x}Sn_xSe_4$. His results together with new estimates from the present data derived through equation (5.19) are compared in Table 5.7 which also gives η for $LiTi_2O_4$ for which there is no corresponding Mössbauer data.

The comparison shows rather poor agreement between the values which have been derived for η in $CuRh_2Se_4$ from the two sources and it may be that A in equation (5.19) should be smaller. However, the more serious error seems likely to have occurred in the Mössbauer experiment for as Taylor and Craig point out the 'S' analysis depends on the extrapolation of harmonic theory to a highly anharmonic system and that when proper correction is made for this, S is smaller and therefore $N(o) < I^2 >$ larger.

Assuming then that the results from the heat capacity data are the more reliable, it is seen that the increase in η from 4.7 to

TABLE 5.7

Parameters significant for the strong coupling superconductivity theory.

Compounds	T_c (^oK)	λ	A (mJ/mole-$^oK^2$)	$<\omega_s^2>$ sec^{-2}	η (eV/$\mathring{A}^2$)
$LiTi_2O_4$	12.4	0.70	- 5.3	3.29×10^{27}	5.3
$CuRh_2Se_4$	3.5	0.59	9.6	0.83×10^{27}	4.7 (0.74)†

† The value obtained from measurements of the Mössbauer 'S' parameter from Dawes (1975).

5.3 eV/Å^2 in passing from $CuRh_2Se_4$ to $LiTi_2O_4$ is sufficient to account for more than two-thirds of the change in λ, in good agreement with the ideas of Allen and Dynes. However, the effect of the simultaneous change in $< \omega^2_s >$ is by no means negligible, for although this effect on λ is more than compensated for by decreased mass, θ_∞ , i.e. $< \omega^2_s >^{\frac{1}{2}}$, occurs explicitly in the McMillan equation for T_c (equation 1.13).

5.4 Discussion

A comparison of the low temperature heat capacity results with those of other workers shows good agreement, although there are still some slight differences which arise from differences in the data treatment. For example, in this present analysis, we have included the T^5 term in the lattice heat capacity expansion. However, Testardi and Mattheiss (see, for example, Testardi, "Physical Acoustics", 1973), using a model acoustic phonon density of states, found that the lattice heat capacity of V_3Si in the harmonic approximation has a term linear in T, in the region of $T > T_c$, which arises from the phonon spectrum. This suggested (Testardi, 1973) that the standard separation of heat capacity data into lattice ($\propto T^3$) and electronic ($\propto T$) terms was likely to be incorrect for A15 compounds. Since the mechanism for superconductivity in spinels is very closely allied to that existing in the A15 compounds (Dawes and Grimes, 1975), the inclusion of the T^5 term in the lattice heat capacity expansion is considered necessary for a meaningful separation of terms. It should also be noted that the comparisons afforded by Table 5.3 show a wide variation in the Debye temperature at low temperature, θ_o, found for $LiTi_2O_4$, whilst a much greater agreement exists among the values reported for $CuRh_2Se_4$. As emphasized in Chapter 3 (Section 3.1.2), $LiTi_2O_4$ is more difficult to prepare with the results that the final composition is often not known precisely. It seems probable, therefore, that the observed variation in the value of θ_o is associated with stoichiometry and, indeed, according to McCallum et al. the composition of their specimens was somewhat different from the nominal composition (Tables 5.2 and 5.3).

As regards the high temperature data, the results presented here represent new findings and so comparison with earlier work on spinels is not possible. However, comparison with the results for the vanadium-based A15 superconductors (Knapp et al., 1975) suggests that similar conclusions concerning the presence of anharmonicity may be drawn.

The major complication in interpreting high temperature heat capacity data is the decoupling of the electronic and anharmonic contributions (γ and A). Ideally, as explained in Section 5.3.2, this should be done above $2\theta_D$ where the electron phonon mass enhancement has decreased to zero. In practice, this is difficult to achieve. Knapp et al., for example, have evaluated the γ values for vanadium-based A15 compounds at ~360°K, i.e., at a temperature of the order of θ_D, and were able to effect some correction for the enhancement of γ by comparison with the temperature dependence of the magnetic susceptibility and spin lattice relaxation times (Section 5.3.2).

In general, the temperature dependence of γ is believed to vary as shown in Figure 5.4 (see, for example, Knapp and Jones, 1972; Grimvall, 1968). Thus, the temperature correction predicted by the nearly free electron approximation, as applied to γ_b and having been used for the spinel data here, probably undercorrects. For example, in the case of V_3Ga, using the values of ε_F from Mattheiss (1965) and γ_b from the results obtained by Knapp et al., values of $\gamma = 9.3$ mJ/mole-$^oK^2$ and, hence, $A = -7.9$ mJ/mole-$^oK^2$ were obtained at 360°K using this

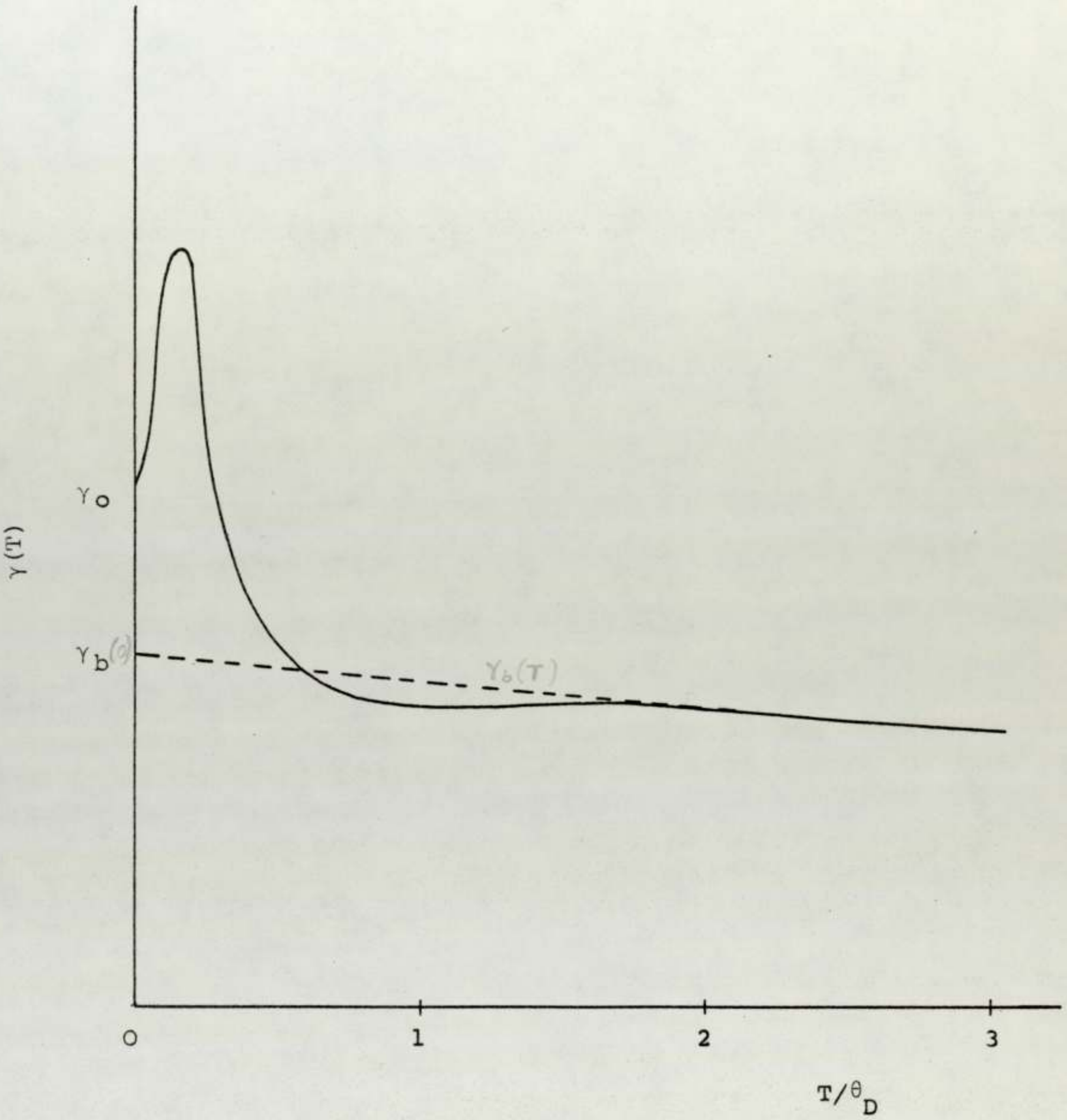

FIGURE 5.4 The temperature dependence of γ versus T/θ_D.

approximation. Yet, via Knapp's analysis they yielded $\gamma = 5.6 \pm 0.6$ mJ/mole$^{\circ}K^2$ and $A = -4.2 \pm 0.9$ mJ/mole-$^{\circ}K^2$. Thus, if anything, the degree of anharmonicity deduced in Section 5.3.2 is an overestimate.

Nevertheless, since T/θ_D is nearly 1.5 for $CuRh_2Se_4$, the error incurred by the nearly free electron approximation should be fairly small in this case. Moreover, as emphasized in Section 5.3.1, $(A + \gamma)$ is certainly much less positive in $LiTi_2O_4$ (see Figure 5.3), the higher T_c material, than in $CuRh_2Se_4$ and, indeed, in the former is comparable with values which have been observed in the vanadium-based A15 alloys. Thus, although the uncertainty in the present results for A in $LiTi_2O_4$ must inevitably be greater than for those values reported by Knapp, they still indicate the presence of a marked anharmonicity.

Finally, although only two superconducting spinels have been studied in this investigation, there is a remarkable consistency in the trend of those derived parameters believed to be important for strong coupling. Thus, it has been established that, in passing from $CuRh_2Se_4$ to $LiTi_2O_4$, not only does the anharmonicity increase whilst the transition temperature increases from 3.5 to 12.4°K, but there are also other favourable changes which contribute to this improvement in the superconducting property. In particular, it has been found that the electron-phonon coupling constant, λ, increases from 0.59 to 0.70 (Table 5.7) and that this is accounted for primarily by changes in the McMillan-Hopfield η parameter. The present results thus provide strong support for the contention by Allen and Dynes that enhanced T_c is not achieved simply by decreasing $< \omega^2 >$. On the contrary, as the behaviour of $LiTi_2O_4$ shows the deterioration in λ in this case resulting from increased $< \omega^2 >$ is almost compensated by the decreased average mass, so that the effect of increased η is reinforced by increased $<\omega^2>$ to provide a dramatic improvement in transition temperature.

CHAPTER 6

CONCLUSIONS AND SUGGESTIONS FOR FUTURE WORK

CHAPTER 6

CONCLUSIONS AND SUGGESTIONS FOR FUTURE WORK

6.1 Conclusions

The major conclusion drawn from this investigation into the heat capacity of the spinels $CuRh_2Se_4$ and $LiTi_2O_4$ is that both these compounds are very satisfactorily described in terms of the theories which have been developed for strong-coupled superconducting materials. In particular, it is noticeable that the parameters which have been deduced on this basis have a high degree of internal consistency. On the other hand, there are numerous indications that this class of superconducting materials is not BCS like in their behaviour. For example, deviations from the BCS predictions for $C_E(T_c)/\gamma_o T_c$ and $H_c(0)$ were found which were more marked in $LiTi_2O_4$, the spinel with higher transition temperature, than in $CuRh_2Se_4$.

Some insight into the reasons for the superior superconducting quantities of $LiTi_2O_4$ compared with $CuRh_2Se_4$ have also been gained from the analysis of the heat capacity results. There is good evidence to show, for example, that the major contribution to the improvement in the electron-phonon coupling comes from changes in the McMillan-Hopfield η parameter in agreement with the suggestions of Allen and Dynes. In addition, the reduction in average mass in passing from $CuRh_2Se_4$ to $LiTi_2O_4$ is accompanied by a substantial increase in the root mean square phonon frequency which also contributes to the near four-fold improvement in T_c.

Finally, evidence has been found to indicate that anharmonicity may be an important factor for superconductivity in spinel compounds for the effects on the heat capacity are particularly marked in $LiTi_2O_4$, the higher T_c material. The present results thus confirm the earlier conclusions drawn by Dawes and Grimes (1975) and Dawes, Grimes and O'Connor (1974) from their X-ray diffraction and Mössbauer studies on the spinel series $CuRh_{2-x}Sn_xSe_4$.

6.2 Suggestions for Future Work

In recent years, a number of high T_c superconducting compounds have been found mainly among substances crystallizing with the A15 or NaCl structures. In both these classes of materials, however, there is increasing evidence that a limit is being reached. For example, among the A15 compounds there is strong evidence to show that the Group IV element is crucial for further improvement in T_c. The highest reported T_c to date has been found with Nb_3Ge ($T_c = 23.2^{\circ}K$ - Testardi et al., (1974)) and it is thought that if Nb_3Si could be prepared in the A15 form then this would possess an even higher T_c. But this has proved to be too difficult a task so far.

For these reasons, there is currently much interest in the possibility of developing ternary superconducting systems and the spinel series, of which $LiTi_2O_4$ seems to be the best example, is only one of two presently known with strong-coupling qualities. The other series is that based on $PbMo_6S_8$ which was first discovered by Chevrel et al., (1971). Evidently, this area of research has only just been opened up so that there must be considerably more scope for further investigation and improvement in superconducting qualities among such materials.

In the case of the spinels, it would be useful to know a great deal more about both the phonon and electron density of states. Considerable expertise exists within the department in electrical and optical measurements using thin films, for example, and it is known that thin film tunneling experiments can yield information of considerable relevance to superconductivity (e.g., an energy gap, the electron-phonon coupling constant, etc.). Similarly, optical measurements, particularly in the infra-red spectrum can be used to deduce the phonon density of states.

In addition to these experiments it would be interesting to carry out Mössbauer investigations on the $LiTi_2O_4$ spinel compound if a suitable Mössbauer absorber can be incorporated into the structure as was done by Dawes (1975) for the series $CuRh_{2-x}Sn_xSe_4$ where ^{119}Sn was used. Certainly, it would seem that further investigations into the possible use of the 'S' parameter of Taylor and Craig ought to be carried out.

Finally, since the mechanism for superconductivity in spinels is very closely allied to that existing in the A15 and NbN compounds (Dawes and Grimes, 1975), it would seem worth while searching for new superconducting spinel compounds among which there may be materials with higher T_c than has yet been observed.

APPENDIX

The Nearly Free Electron Approximation

APPENDIX

The Nearly Free Electron Approximation

If we assume that the band electrons of the spinel compounds are treated as being only weakly affected by the periodic potential of the ion cores, then, if $N(\varepsilon)$ is the density of states of the free electrons (for one direction of spin), the internal energy per unit volume, U, is of the general form:

$$U = 2 \int_0^\infty \varepsilon N(\varepsilon) f(\varepsilon) d\varepsilon \qquad \text{......} \ (1)$$

subject to the condition that the total number of electrons, N, is as:

$$N = 2 \int_0^\infty N(\varepsilon) f(\varepsilon) d\varepsilon \qquad \text{......} \ (2)$$

The electronic heat capacity, γ, is given by the relation:

$$\gamma = \frac{1}{T} \frac{\partial U}{\partial T} \qquad \text{......} \ (3)$$

In the case of the nearly free electron model:

$$\varepsilon = \frac{\hbar^2 q^2}{2m^*} \qquad \text{......} \ (4)$$

where $\vec{q}$ is the wave vector for an electron of energy ε and effective mass m^* and the number of energy level, $N(\varepsilon)$, within the range ε to $\varepsilon + d\varepsilon$ is given by:

$$N(\varepsilon) d\varepsilon = \frac{V}{8\pi^3} \int dq \qquad \text{......} \ (5)$$

where the integration is over the volume in $\vec{q}$ space contained between two concentric spheres of radii $\vec{q}$ and $\vec{q} + d\vec{q}$, i.e.:

$$N(\varepsilon) d\varepsilon = \frac{4\pi V q^2 dq}{8\pi^3} = \frac{Vq^2}{(2\pi^2)} dq \qquad \text{......} \ (6)$$

From equations (4) and (5):

$$\therefore \quad N(\varepsilon) = 2\ \{\ 2\pi V(2m^*)^{3/2}\varepsilon^{\frac{1}{2}}/h^3\ \} \qquad \ldots\ldots (7)$$

where the factor of 2 arises from the two spin orientations. Therefore, the internal energy, U, can be derived in the form:

$$U = \frac{Nk_BT \int_0^\infty (\frac{\varepsilon}{k_BT})^{3/2} f(\varepsilon)\,d(\frac{\varepsilon}{k_BT})}{\int_0^\infty (\frac{\varepsilon}{k_BT})^{\frac{1}{2}} f(\varepsilon)\,d(\frac{\varepsilon}{k_BT})}$$

or

$$U = Nk_BT.\ \frac{F_{3/2}(\mu)}{F_{\frac{1}{2}}(\mu)} \qquad \ldots\ldots (8)$$

where

$$F_s(\mu) = \int_0^\infty \frac{(\frac{\varepsilon}{k_BT})^s d(\frac{\varepsilon}{k_BT})}{(e^{(\varepsilon-\mu)/k_BT}+1)} \qquad \ldots\ldots (9)$$

and μ is called the 'chemical potential' which has a value equal to the Fermi energy, ε_F, at $T = 0^\circ K$.

Now at $T = 0^\circ K$, $f(\varepsilon) = 1$ for $\varepsilon \leqslant \varepsilon_F$ and $= 0$ for $\varepsilon > \varepsilon_F$

$$\therefore \quad N = C\int_0^\infty \frac{\varepsilon^{\frac{1}{2}}d\varepsilon}{(e^{(\varepsilon-\mu)/k_BT}+1)}$$

$$= C\int_0^\infty \varepsilon^{\frac{1}{2}}d\varepsilon = \frac{2}{3}C\varepsilon_F^{3/2}$$

and

$$F_{\frac{1}{2}}(\mu) = \frac{2}{3}(\frac{\varepsilon_F}{k_BT})^{3/2} \qquad \ldots\ldots (10)$$

From equations (8) and (10) we have:

$$U = \frac{3}{2}Nk_BT(\frac{k_BT}{\varepsilon_F})^{3/2}F_{3/2}(\mu) \qquad \ldots\ldots (11)$$

Up to this point, the analysis is exact but now we have to make an approximation. In making this approximation, we follow Wilson (1953), and McDougall and Stoner (1938) and express $F_{3/2}(\mu)$ in the form:

$$F_{3/2}(\mu) = \frac{2}{5}\left(\frac{\mu}{k_BT}\right)^{5/2}\left\{1 + \frac{15}{2}C_2\left(\frac{k_BT}{\mu}\right)^2 - \frac{15}{8}C_4\left(\frac{k_BT}{\mu}\right)^4 + \ldots\right\} \qquad \ldots\ldots (11)$$

where $C_2 = \frac{\pi^2}{12}$; $C_4 = \frac{7\pi^4}{720}$; $C_6 = \frac{31\pi^6}{30240}$ etc.

Note that from equation (10)

$$\left(\frac{\varepsilon_F}{k_BT}\right)^{3/2} = \left(\frac{\mu}{k_BT}\right)^{3/2}\left\{1 + \frac{3C_2}{2}\left(\frac{k_BT}{\mu}\right)^2 + \frac{9C_4}{8}\left(\frac{k_BT}{\mu}\right)^4 + \ldots\right\} \qquad \ldots\ldots (12)$$

which when inverted gives:

$$\frac{\mu}{k_BT} = \left(\frac{\varepsilon_F}{k_BT}\right)\left\{1 - C_2\left(\frac{k_BT}{\varepsilon_F}\right)^2 - \frac{3}{4}(C_2{}^2 + C_4)\left(\frac{k_BT}{\varepsilon_F}\right)^4 \ldots\right\} \qquad \ldots\ldots (13)$$

These expansions are valid if $\mu/k_BT > 1$ and therefore for the spinels for the case of $CuRh_2Se_4$, $\varepsilon_F = 0.11$ eV (Schaeffer et al., 1970), i.e., at $T = 0^\circ K$, $\mu = 0.11$ eV and increases at higher temperatures while $LiTi_2O_4$ has $\varepsilon_F = 0.14$ eV.

Substituting equation (13) into equation (11) gives:

$$U = \frac{3}{5}N(\varepsilon_F)\left\{1 + \frac{5\pi^2}{12}\left(\frac{k_BT}{\varepsilon_F}\right)^2 - \frac{\pi^2}{16}\left(\frac{k_BT}{\varepsilon_F}\right)^4 \ldots\right\}$$

Hence,

$$\gamma = \frac{1}{T}\frac{\partial U}{\partial T} = \frac{2}{3}\pi^2 k_B{}^2 N(\varepsilon_F)\left\{1 - \frac{3\pi^2}{10}\left(\frac{k_BT}{\varepsilon_F}\right)^2 \ldots\right\}$$

$$\therefore \quad \gamma = \gamma_b\left\{1 - \frac{3\pi^2}{10}\left(\frac{k_BT}{\varepsilon_F}\right)^2 \ldots\right\} \qquad \ldots\ldots (14)$$

ACKNOWLEDGEMENTS

This research work was carried out during the tenure of the Colombo Plan scholarship while on leave of study from the University of Chiengmai, Thailand.

I would like to express my deepest sincere thanks to my supervisor, Dr. N.W. Grimes, for his helpful suggestions, encouragement and patient reading throughout this thesis.

I am also indebted to Dr. W.E.J. Neal for his enthusiastic support and valuable suggestions while the present work was in progress.

I wish to express my gratitude to the technical staff of Physics Department, in particular to Mr. H. Arrowsmith of the main workshop and also to Mr. G. Cochrane of the x-ray laboratory.

Finally, my thanks are due to Professor S.E. Hunt in whose Department this work was performed and also to Professor T. Mulvey for his interest.

REFERENCES

REFERENCES

P.B. Allen and R.C. Dynes, Phys. Rev. B, 12 (3), 905 (1975).

G. Aschermann, E. Friederich, E. Justi and J. Kramer, Phys. Z., 42, 349 (1941).

R. Bachmann, F.J. DiSalvo, Jr., T.H. Geballe, R.L. Greene, R.E. Howard, C.N. King, H.C. Kirsch, K.N. Lee, R.E. Schwall, H.U. Thomas and R.B. Zubeck, Rev. Sci. Instrum., 43, 205 (1972).

J. Bardeen, L.N. Cooper and J.R. Schrieffer, Phys. Rev., 108, 1175 (1957).

J. Bardeen and J.R. Schrieffer, Recent Developments in Superconductivity, Progress in Low Temperature Physics, Vol. III, C.J. Gorter, ed., New York, Interscience (1961).

T.H.K. Barron, Lattice Dynamics, R.F. Wallis, ed., Pergamon, London, p 247 (1965).

T.F.W. Barth and E. Posnjak, Z. Kristallogr., 82, 325 (1932).

H.E. Barz, A.S. Cooper, E. Corenzwit, M. Marezio, B.T. Matthias and P.H. Schmidt, Science, 175, 884 (1972).

W.T. Berg and J.A. Morrison, Proc. Roy. Soc., A242, 467 (1957).

W. Bindloss, J. Appl. Phys., 42, 1474 (1971).

M. Born, Proc. Camb. Phil. Soc., 36, 160 (1940).

M. Born and V. Kármán, Th., Phys. Zeits., 13, 297 (1912).

V.A.M. Brabers, Phys. Stat. Solidi, 33, 563 (1969).

W.H. Bragg, Nature, 95, 561; Phil. Mag., 30, 305 (1915).

L. Cervinka, Czech. J. Phys. B, 15, 747 (1965).

R.W. Cheary, Ph.D. Thesis, Univ. of Aston in Birmingham (1971).

R.W. Cheary, Private Communication.

R. Chevrel, M. Sergent and J. Prigent, J. Solid State Chem., 3, 515 (1971).

C. Chou, D. White and H.L. Johnston, Phys. Rev., 109 (2), 788 (1958).

T. Cleason and S. Lundquist, Physica Scripta, 10, 5 (1974).

L.N. Cooper, Phys. Rev., 104, 1189 (1956).

J.G. Dash, D.P. Johnson and W.M. Visscher, Phys. Rev., 168, 1087 (1968).

P.P. Dawes, Ph.D. Thesis, Univ. of Aston in Birmingham (1975).

P.P. Dawes and N.W. Grimes, Solid St. Commun., 16, 139 (1975).

P.P. Dawes, N.W. Grimes and D.A. O'Connor, J. Phys. C : Solid St. Phys., 7, L387 (1974).

P. Debye, Ann. d. Physik, 39, 789 (1912).

J.D. Dunitz and L.E. Orgel, J. Phys. Chem. Solids, 3, 20 (1957).

A. Einstein, Ann. d. Physik, 22, 180 (1907).

B.J. Evan, S.S. Hafner and H.P. Weber, J. Chem. Phys., 55, 5282 (1971).

S. Foner and E.J. McNiff, Jr., Sol. State Commun., 20, 995 (1976).

S. Foner, E.J. McNiff, Jr., and E.J. Alexander, Phys. Lett., 49A, 269 (1974).

H. Fröhlich, Phys. Rev., 79, 845 (1950).

C.J. Frosch, Transistor Technology, Vol. III, F.J. Biondi, ed., D. van Nostrand Company, Inc., New York, p 94 (1958).

C.J. Frosch and L. Derick, J. Electrochem. Soc., 104, 547 (1957).

G.T. Furukawa, W.G. Saba and M.L. Reilly, Critical Analysis of Heat Capacity Data of The Literature and Evaluation of Thermo-Dynamic Properties of Copper, Silver and Gold from 0 to 300^{o}K, Nat. Bur. Std. Publ. NSRDS-NBS-18.

G.D. Gaspari and B.L. Gyorffy, Phys. Rev. Lett., 28, 801 (1972).

J.R. Gavaler, Appl. Phys. Lett., 23, 480 (1973).

I. Giaever and K. Megerle, Phys. Rev., 122, 1101 (1961).

W.F. Giauque, The Scientific Papers of W.F. Giauque, Vol. I, Dover, New York, p 332 (1969).

A.L. Giorgi, E.G. Szklarz and M.C. Krupka, Superconductivity in d- and f- Band Metals, D.H. Douglass, ed., American Institute of Physics, New York, p 147 (1972).

B.B. Goodman (1959), see E.A. Lynton, Superconductivity, 3rd edition, B.L. Worshop and G.K.T. Conn, ed., Methuen & Co. Ltd., London (1967).

E.W. Gorter, Philips Res. Rep., 9, 295 (1954).

C.J. Gorter and H.B.G. Casimir, Physica, 1, 306 (1934a).

C.J. Gorter and H.B.G. Casimir, Phys. Z., 35, 963; Z. techn. Phys., 15, 539 (1934b).

N.W. Grimes, J. Phys. C : Solid St. Phys., 4, L342 (1971).

N.W. Grimes, Phil. Mag., 26, 1217 (1972).

N.W. Grimes, J. Phys. C : Solid St. Phys., 6, L78 (1973).

N.W. Grimes, Proc. R. Soc. Lond, A, 338, 223 (1974).

N.W. Grimes, Physics in Technology, 22 (1975).

N.W. Grimes, Contemp. Phys., 17(1), 71 (1976).

N.W. Grimes and A.J. Collectt, Phys. Stat. Solidi(b), 43, 591 (1971).

N.W. Grimes and R.J. Hilleard, J. Phys. C : Solid St. Phys., 3, 866 (1970).

G. Grimvall, J. Phys. Chem. Solids, 29, 1221 (1968).

G.F. Hardy and J.K. Hulm, Phys. Rev., 89, 884 (1953).

J.J. Hopfield, Phys. Rev., 186, 443 (1969).

A. Hudson and H.J. Whitfield, Molec. Phys., 12, 165 (1967).

L. Hwang, A.H. Heuer and T.E. Mitchell, Phil, Mag., 28, 241 (1973).

D.C. Johnston, J. Low Temp. Phys., 25, 145 (1976).

D.C. Johnston, H. Prakash, W.H. Zachariasen and R. Viswanathan, Mat. Res. Bull, 8, 777 (1973).

H. Kamerlingh Onnes, Leiden Comm., 122b, 1206; 124c, 1226 (1911).

W.H. Keesom and J.A. Kok, Commun. Phys. Lab. Univ. Leiden, No. 219c, (1932).

C.W. Kimball, S.P. Taneja, L. Weber and F.Y. Fradin, Mössbauer Effect Methodology, Vol. 9, I.J. Gruverman, C.W. Seidel and D.K. Dieterly, ed., Plenum Press, New York and London, p 93 (1974).

A.J. Kirkham and B. Yates, Cryogenics, 381 (1968).

T.A. Kitchens, P.P. Craig and R.D. Taylor, Mössbauer Effect Methodology, Vol. 5, I.J. Gruverman, ed., Plenum Press, New York, London, p 123 (1970).

G.S. Knapp, S.D. Bader, H.V. Culvert, F.Y. Fradin and T.E. Klippert, Phys. Rev. B, 11, 4331 (1975).

G.S. Knapp and R.W. Jones, Phys. Rev. B, 6, 1761 (1972).

J. Kondo, Prog. of Theor. Phys., 32(1), 37 (1964).

W. Kunz and E. Saur, Z. Phys., 189, 401 (1966).

J. Labbé and J. Friedel, J. Phys. Chem. Sol., 28, 2477 (1967a).

J. Labbé and J. Friedel, Phys. Rev., 158, 647 and 655 (1967b).

F. London, Superfluids, Vol. i, Dover, New York, p 20 (1950).

F. London and H. London, Proc. Roy. Soc., A149, 71 (1935a).

F. London and H. London, Physica, 2, 341 (1935b).

F.K. Lotgering, J. Phys. Chem. Solids, 23, 1153 (1962).

F.K. Lotgering and R.P. van Stapele, J. Appl. Phys., 39, 417 (1968).

F.H. Lou and D.W. Ballentyne, J. Phys. C : Proc. Phys. Soc., Series 2, 1, 608 (1968).

E.A. Lynton, Superconductivity, 3rd edition, Methuen & Co. Ltd., 147 (1967).

R.W. McCallum, D.C. Johnston, C.A. Luengo and M.B. Maple, J. Low Temp. Phys., 25, 177 (1976).

J. McDougall and E.C. Stoner, Roy. Soc. Philas. Trans., A237, 67 (1938).

W.L. McMillan, Phys. Rev., 167(2), 331 (1968).

N. Mangkorntong, Ph.D. Thesis, Univ. of Aston in Birmingham (1977).

D.L. Martin (1966), Critical Analysis of Heat-Capacity Data of The Literature and Evaluation of Thermodynamic Properties of Copper, Silver and Gold from 0 to 300°K, Nat. Bur. Std. Publ. NSRDS-NBS-18.

M. Marezio, P.D. Dernier, J.P. Remeika, E. Corenzwit and B. Matthias, Mat. Res. Bull., 8, 657 (1973).

L.F. Mattheiss, Phys. Rev., 138, A112 (1965).

B.T. Matthias, Phys. Rev., 92, 874 (1953).

B.T. Matthias, Chapter 5, Progress Low Temperature Physics, Vol. 2, C.J. Gorter, ed., New York, Interscience (1957).

B.T. Matthias, IEEE. Trans. on Mag., Mag-11(2), 154 (1975).

B.T. Matthias, T.H. Geballe and V.B. Compton, Rev. Mod. Phys., 35, 1 (1963).

B.T. Matthias, T.H. Geballe, S. Geller and E. Corenzwit, Phys. Rev., 95, 1435 (1954).

B.T. Matthias, T.H. Geballe, L.D. Longinotti, E. Corenzwit, G.W. Hull, R.H. Willens and J.P. Maita, 156, 645 (1967).

B.T. Matthias, M. Marezio, E. Corenzwit, A.S. Cooper and H.E. Barz, Science, 175, 1465 (1972).

E. Maxwell, Phys. Rev., 78, 477 (1950).

W. Meissner and R. Ochsenfeld, Naturwiss., 21, 787 (1933).

A.P. Miller and B.N. Brockhouse, Can. J. Phys.,49, 704 (1971).

P. Morel and P.W. Anderson, Phys. Rev., 125, 1263.

W. Nernst and F.A. Lindemann, Zeits. Electrochem., 17, 817 (1911).

S. Nishikawa, Proc. Tokyo math-phys. Soc., 8, 199 (1915).

N. Pessall, R.E. Gold and H.A. Johansen, J. Phys. Chem. Sol., 29, 19 (1968).

J.C. Phillips. J. Appl. Phys., 43, 3560 (1972).

V.L. Pokrovskii, J.E.T.P. USSR, 40, 641; Soviet Phys. J.E.T.P., 13, 447 (1961).

V.L. Pokrovskii and M.S. Ryvkin, J.E.T.P. USSR, 43, 92 (1962).

T.V. Ramakrishnan, J. Phys. C : Solid St. Phys., 6, 3041 (1973).

J.P. Remeika, T.H. Geballe, B.T. Matthias, A.S. Cooper, G.W. Hull and E.M. Kelly, Phys. Lett., 24A, 565 (1967).

C.A. Reynolds, B. Serin, W.H. Wright and L.B. Nesbitt, Phys. Rev., 78, 487 (1950).

M. Robbins, J. Phys. Chem. Sol., 28, 897 (1967).

M. Robbins, A. Menth, M.A. Miksovsky and R.C. Sherwood, J. Phys. Chem. Solids, 31, 423 (1970).

M. Robbins, R.H. Willens and R.C. Miller, Solid St. Commun., 5, 933 (1967).

J.K. Roberts and A.R. Miller, Heat and Thermodynamics, 4th edition, Blackie & Son Ltd., London, p 209 (1951).

G.M. Schaeffer and M.H. van Maaren, Proc. of the 11th Int. Conf. on Low Temp. Physics, St. Andrews, 1033 (1968).

H. Shechter, J.G. Dash, G.A. Erickson and R. Ingall, Phys. Rev. B, 2, 613 (1970).

R.N. Shelton, D.C. Johnston and H. Adrian, Solid St. Commun., 20, 1077 (1976).

J.S. Shier and R.D. Taylor, Solid St. Commun., 5, 147 (1967).

J.S. Shier and R.D. Taylor, Phys. Rev., 174, 346 (1968).

G. Shirane and J.D. Axe, Phys. Rev. Lett., 27, 1803 (1971).

G. Shirane and J.D. Axe, Solid St. Commun., 9, 397 (1971).

T.F. Smith, T.R. Finlayson and R.N. Shelton, J. Less-Common. Metals, 43, 21 (1975).

R. Stahl-Brada and W. Low, Phys. Rev., 116, 561 (1959).

J.C. Swihart, D.J. Scalapino and Y. Wada, Phys. Rev. Lett., 14, 106 (1965).

M. Tanaka, T. Tokoro and Y. Aiyama, J. Phys. Soc. Japan, 21, 262 (1966).

R.D. Taylor and P.P. Craig, Phys. Rev., 175, 782 (1968).

L.R. Testardi, Phys. Rev., B5, 4342 (1972).

L.R. Testardi, Physical Acoustics, Academic, New York, Vol. 10, 193 (1973).

L.R. Testardi, R.R. Soden, E.S. Greiner, J.H. Wernick and V.G. Chirba, Phys. Rev., 154, 399 (1967).

L.R. Testardi, J.H. Wernick and W.A. Royer, Solid St. Commun., 15, 1 (1974).

K.G. van den Berg, J.C. Lodder and T.C. Mensinga, Thin Solid Films, 34, 243 (1976).

M.H. van Maaren and H.B. Harland, Phys. Lett., 30A, 264 (1969).

M.H. van Maaren, H.B. Harland and E.E. Havinga, Solid St. Commun., 8, 1933 (1970).

M.H. van Maaren, G.M. Schaeffer and F.K. Lotgering, Phys. Lett., 25A, 238 (1967).

D.P. Williamson and N.W. Grimes, J. Phys. D : Appl. Phys. 7, 1 (1974).

A.H. Wilson, The Theory of Metals, 2nd edition, Cambridge University Press, p 146 (1953).

H.R. Zeller, Phys. Rev., B5, 1813 (1972).